**Geoscientific
Model Development
Discussions**

A contrail cirrus prediction model

U. Schumann

Deutsches Zentrum für Luft- und Raumfahrt, Institut für Physik der Atmosphäre, Oberpfaffenhofen, Germany

Correspondence to: U. Schumann (ulrich.schumann@dlr.de)

GMDD

4, 3185–3293, 2011

Contrail cirrus model

U. Schumann

Title Page

Abstract	Introduction
Conclusions	References
Tables	Figures

Back | Close

Full Screen / Esc

Printer-friendly Version

Interactive Discussion

Abstract

A new model to simulate and predict the properties of a large ensemble of contrails as a function of given air traffic and meteorology is described. The model is designed for approximate prediction of contrail cirrus cover and analysis of contrail climate impact,
5 e.g. within aviation system optimization processes. The model simulates the full contrail life-cycle. Contrail segments form between waypoints of individual aircraft tracks in sufficiently cold and humid air masses. The initial contrail properties depend on the aircraft. The advection and evolution of the contrails is followed with a Lagrangian Gaussian plume model. Mixing and bulk cloud processes are treated quasi analytically
10 or with an effective numerical scheme. Contrails disappear when the bulk ice content is sublimating or precipitating. The model has been implemented in a "Contrail Cirrus Prediction Tool" (CoCiP). This paper describes the model assumptions, the equations for individual contrails, and the analysis-method for contrail-cirrus cover derived from the optical depth of the ensemble of contrails and background cirrus. The model has
15 been applied for a case study and compared to the results of other models and in-situ contrail measurements. The simple model reproduces a considerable part of observed contrail properties. Mid-aged contrails provide the largest contributions to the product of optical depth and contrail width, important for climate impact.

1 Introduction

20 Contrails are thin line-shaped ice particle clouds which form in the atmosphere behind cruising aircraft because of mixing of the emitted water vapor with cold ambient air leading to local liquid saturation, condensation of water on aerosols, and subsequent freezing (Schmidt, 1941; Appleman, 1953; Schumann, 1996). In ice supersatured air masses contrails spread and grow by uptake of ambient water. The total ice mass
25 content may be several orders of magnitude larger than the amount of water emitted from the aircraft (Knollenberg, 1972; Heymsfield et al., 1998; Atlas et al., 2006).

Contrail cirrus model

U. Schumann

Contrails have often been observed to persist for many hours and transform into contrail cirrus, with considerable cloud cover and optical depth (Detwiler and Pratt, 1984; Schumann and Wendling, 1990; Bakan et al., 1994; Minnis et al., 1998; Duda et al., 2001; Mannstein and Schumann, 2005; Atlas et al., 2006; Vazquez-Navarro, 2009; Atlas and Wang, 2010). Persisting contrails are often associated with, or embedded in thin cirrus (Sassen, 1997; Immler et al., 2008). Contrail outbreaks forming in regions with high traffic density, high humidity and thin cirrus may cause a considerable fraction of the annual mean contrail cover (Duda et al., 2001; Haywood et al., 2009). Presently more than 80 000 commercial flights per day are performed globally and traffic is increasing (Wilkerson et al., 2010). A large fraction of the aircraft cruises at altitudes where contrails may form (Appleman, 1953; Miake-Lye et al., 1993; Sausen et al., 1998). Contrails may provide surfaces for heterogeneous chemistry (Meilinger et al., 2005; Voigt et al., 2010). Contrails are visible tracers of aircraft impact on the atmosphere. In spite of still large uncertainties, the climate impact of contrails appears to be important (Fahey et al., 1999; IPCC, 2007; Lee et al., 2010; Burkhardt and Kärcher, 2011).

In order to assess the climate impact of individual aircraft flights, e.g. as input for route optimization (Mannstein et al., 2005), for aircraft optimization (Green, 2002; Koch et al., 2009; Schwartz and Kroo, 2011), or for prediction of contrail cover in an area with intense air traffic day by day (Duda et al., 2009), one needs a model which is able to compute contrail properties for individual flights as well as for a large fleet of aircraft regionally and globally with short computation times.

Contrail and cirrus formation is a nonlinear process depending strongly on ambient meteorology and plume processes (Scorer and Davenport, 1970; Lee et al., 2010). These plume processes are inherently subgrid-scale in multidimensional global models (Schumann and Konopka, 1994; Cariolle et al., 2009; Burkhardt et al., 2010; Paoli et al., 2011). Plume ice cloud models with different degree of complexity for mixing and particle microphysics have been developed (Miake-Lye et al., 1993; Kärcher et al., 1996, 2009a; Brown et al., 1997; Jensen et al., 1998b; Kärcher, 1998; Meilinger et al.,

2005; Naiman et al., 2010), but none of them treats the whole contrail life cycle from contrail formation until dissipation.

The decision of whether a contrail forms or not along a given flight is a relatively simple task because it can be explained thermodynamically once the meteorological and aircraft parameters are sufficiently known (Schumann, 1996; Rädel and Shine, 2007). Numerical weather prediction (NWP) and flight track data have been used to identify contrail forming flight tracks and follow their advection (Duda et al., 2004; Atlas et al., 2006; Duda et al., 2009). From comparisons with satellite data at computed contrail positions, optical and sedimentation properties were successfully deduced (Duda et al., 2004). Contrail persistence analysis was compared with satellite derived contrail cover showing high sensitivity to ice supersaturation and vertical wind input (Duda et al., 2009).

However the formation of ice particles in the exhaust jet at time scales of 0.1-20 seconds (Kärcher et al., 1998; Paoli and Garnier, 2005; Paoli et al., 2008), their spreading and downwash (Scorer and Davenport, 1970) with the wake vortices forming behind aircraft at time scales of 1–20 min (Lewellen and Lewellen, 2001) and their transition into wide-spread cirrus clouds and final decay, at timescales of less than a hour to possibly days (Unterstrasser and Gierens, 2010a) are difficult to compute in one model. Three-dimensional large eddy simulations resolve the fluid dynamics of wake vortex formation and decay (Gerz and Ehret, 1996; Lewellen and Lewellen, 1996; Holzäpfel et al., 2010; Misaka et al., 2012) and the bulk microphysics of contrails (Gierens, 1996; Chlond, 1998; Lewellen and Lewellen, 2001; Unterstrasser and Sölch, 2010), but require large computing times. Even two-dimensional variants of such models, which allow for parameter studies and several hours of contrail ages, are too expensive to be applied for simulations of a large ensemble of contrails with realistic meteorological variability (Jensen et al., 1998a; Gierens and Jensen, 1998; Unterstrasser and Gierens, 2010b). Hence, simpler models, using parameterized physics are required which provide proper results for the whole contrail life cycle for the global aircraft fleet under realistic meteorological conditions with far less computing time.

Such a model, the "Contrail Cirrus Prediction Tool" (CoCiP), is described in this paper. The model principles and its application for comparison with satellite data have been presented briefly before (Schumann, 2009). Basic model features and comparisons to in-situ observations have been published in Voigt et al. (2010). The model has been applied to estimate the global climate impact of contrail cirrus and to demonstrate the potential of mitigation of contrail climate impact by route optimization (Schumann et al., 2011a). This paper describes the details of the basic model concept, presents global results for illustration and compares results for special cases with other models and observations.

2   Model

2.1   The Gaussian concentration profile

The spatial distribution of concentrations in a plume or contrail segment (without or with ice) at any time t has to be know for computing plume properties depending on its width, depth, cross-section area, and shear-induced inclination. For this purpose, the concentration field in the plume is approximated as a Gaussian function of given width (or breadth) B, depth D and inclination using the analytical relationships derived by Konopka (1995). Here we describe the concentration profile. The computation of the plume parameters and their integration in time are explained in the following sections.

The concentration c of a species per air mass in the plume with local orthogonal coordinates (x, y, z) relative to the plume axis (x = flight direction, y = cross-direction, z = vertical) is approximated in the plane perpendicular to the segment axis by a Gaussian function of the position vector

$$\mathbf{x} = (y, z)^T,$$
$$c(\mathbf{x}) = \frac{C_0}{A} \exp[-\frac{1}{2}\mathbf{x}^T \sigma^{-1} \mathbf{x}] \tag{1}$$

The effective cross section area A of the plume follows from the integral over all y and z,

$$A \equiv \iint \exp[-\frac{1}{2}\mathbf{x}^T \sigma^{-1} \mathbf{x}]d\mathbf{x}. \tag{2}$$

As a consequence, see Appendix A1,

$$A = 2\pi[\det(\sigma)]^{1/2}, \tag{3}$$

and

$$\iint c(\mathbf{x})d\mathbf{x} = C_0, \tag{4}$$

where $C_0(x,t)$ is the mass of the species per plume length and C_0/A is the volume specific concentration in the center of the plume. Here $\sigma(\mathbf{x},t)$ is the covariance matrix of the concentration field c in the plane for unit mass content ($C_0 = 1$) (Konopka, 1995),

$$\sigma = \iint (\mathbf{x} \otimes \mathbf{x})c(\mathbf{x})d\mathbf{x}, \tag{5}$$

(with dyadic product $\otimes$). The components of σ describe a real symmetric and positive definite matrix,

$$\sigma = \begin{pmatrix} \sigma_{yy} & \sigma_{yz} \\ \sigma_{yz} & \sigma_{zz} \end{pmatrix}. \tag{6}$$

The inverse matrix is

$$\sigma^{-1} = \frac{1}{\det(\sigma)} \begin{pmatrix} \sigma_{zz} & -\sigma_{yz} \\ -\sigma_{yz} & \sigma_{yy} \end{pmatrix}, \tag{7}$$

with $\det(\sigma) = \sigma_{yy}\sigma_{zz} - (\sigma_{yz})^2$.

Since the area of an ellipse in normal form with width B and depth D is $A = \pi BD/4$, we identify

$$B^2 = 8\sigma_{yy}, D^2 = 8\sigma_{zz}. \tag{8}$$

Contrail cirrus model

U. Schumann

For optical depth computation, as we will see, we need the effective vertical depth $D_{\text{eff}} = A/B$ which equals $D\pi/4$ initially but gets smaller when the cross-section deforms with ambient shear.

This plume model has been used in the past to derive turbulent diffusivities from observed trace gas measurements and large eddy simulations (Schumann et al., 1995; Dürbeck and Gerz, 1995, 1996; Schlager et al., 1997), has been applied for air chemistry, sometimes as part of regional and global models (Schumann and Konopka, 1994; Karol et al., 1997; Kraabøl et al., 2000), and has been used as benchmark for tests of other models (Naiman et al., 2010; Unterstrasser and Gierens, 2010a). Compared to earlier plume studies (Danilin et al., 1994; Kärcher, 1995), this model accounts not only for turbulent diffusion but also shear. Its main advantage compared to an elliptical model described by Naiman et al. (2010) lies in the fact that the Konopka-model gives the exact solution of the advection-diffusion equations for constant shear and constant diffusivities.

The shape of aged contrails is sometimes not too far different from a Gaussian plume shape (Freudenthaler et al., 1995; Paugam et al., 2010). However the initial exhaust jet, wake vortex and contrail (with primary and secondary parts) often deviate considerably from this shape (Sussmann and Gierens, 1999; Gerz et al., 1998; Holzäpfel et al., 2010; Lewellen and Lewellen, 2001; Misaka et al., 2012). However, the Gaussian approximation allows for efficient simulation of global contrail cover. (In the future, one might use two plumes to simulate the primary and secondary vortex separately, for given split of the emission into these two parts.)

2.2 Numerical weather prediction input

CoCiP simulates the contrails formed for given meteorology regionally or globally. NWP data are used to determine the ambient meteorological conditions by linear interpolation for given positions and times (see Appendix A2).

Sub-module INITMET, see Fig. 2, reads input of discrete three-dimensional and time-dependent NWP fields for pressure p, geopotential altitude z, horizontal velocities u

(eastward) and v (northward), pressure change rate $\omega = dp/dt$, absolute temperature T, absolute humidity q, cirrus ice water mass fraction I_C, fractional cloud cover C_C, and kinetic energy of subgrid-scale motions E_{SGS}. For analysis of radiative forcing we also require input for the flux values of outgoing longwave radiation (OLR), the reflected

5   solar radiation (RSR), and the solar direct radiation (SDR) at top of the atmosphere as a function of x, y, and t from the NWP model. Finally we specify the solar constant $S_0(t)$ for the time of the year consistent with the NWP data.

For global studies we use analysis data from the Integrated Forecast System (IFS) of the European Center for Medium Range Weather Forecasts (ECMWF; see

10   http://www.ecmwf.int/research/ifsdocs/). Since a few years, the ECMWF model allows for supersaturation in clear air which has been demonstrated useful for this purpose (Tompkins et al., 2007; Rädel and Shine, 2007; Haywood et al., 2009; Lamquin et al., 2009). The model assumes that ice forms in a fraction of a grid cell when the supersaturation reaches the limit for homogeneous ice nucleation (Koop et al., 2000) typically

15   of the order 150 %. In this study, the grid-cell mean humidity is taken as representative in both the cloudy and clear parts of the grid cell. For regional applications we used NWP input from the COSMO-DE model of the German Weather Service. Also the meteorological fields from a global circulation climate model can be used to drive CoCiP.

20   Presumably the most critical input from the NWP model is the relative humidity RHi over ice, which is the dominant parameter for controlling the ice mass content in contrails (Unterstrasser and Gierens, 2010a). Contrails like cirrus, once formed, persist when the relative humidity is above a critical value RHi_c. In principle, $RHi_c = 1$. However, supersaturated regions are shallow and narrow and hence may not be resolved

25   by the discrete humidity field on a finite grid. Moreover, random subgrid scale variability could cause local supersaturation in a grid cell that is subsaturated on average (Lamquin et al., 2009). Hence, the critical value RHi_c is usually taken different and below 100 % in NWP models. In the ECMWF model, this value is

$$RHi_c = 0.8, \tag{9}$$

in the mid-troposphere, 1.0 in the stratosphere and follows a smooth transition with pressure altitude between these two values in the upper 20 % of the troposphere. For simplicity of further analysis, we divide the input value of q by RHi_c initially. Care has to be taken when interpolating humidity (see Sect. A2).

2.3 Flight track and aircraft definition

CoCiP simulates the contrails formed by cruising aircraft, flight by flight. Flight routes are prescribed on input as a sequence of waypoints versus flight time. For example, waypoint data from commercial flights over North America and Southern Canada are available in the internet (Garber et al., 2005). We got such data for case studies for German airspace from the Deutsche Flugsicherung (DFS) for a few days in October–November 2008, and for the European and the North Atlantic air space from EURO-CONTROL for some days in August 2005. A global data set was setup by the United States (US) Federal Aviation Administration (FAA) with support from Volpe National Transportation Systems Center based on a cooperation by FAA, EUROCONTROL, and ICAO for 2006 (Wilkerson et al., 2010). For other periods we simulate waypoint tracks for global commercial aviation using aircraft type, airport-connection, and schedule information from the Official Airline Guide (OAG), a commercially available product. (For a list of abbreviations and frequently used symbols, see Tables 6 and 7 in the Appendix.)

From such data, for each flight, a sub-module READFP reads the input to define the aircraft type and a list of $N_W > 1$ waypoints $W_i = (x_i, y_i, z_i, t_i)$, $i = 1, 2, \ldots, N_W$, in space and time, specifying longitude x, latitude y, altitude z, and time t, from start to end of the given flight track. The waypoints usually list the flight level z_i which is converted to a static pressure $p_{0,i}$ according to the standard atmosphere of aviation (ICAO, 1964), see Appendix A4. CoCiP loops over the waypoints or over flight segments $S_i = (W_i, W_{i+1})$, $i = 1, 2, \ldots, N_W - 1$. For each waypoint we set a flag to identify if the waypoint is followed by a contrail segment or a flight segment without contrail. This allows considering tracks with several non-consecutive contrails.

Wake vortices, particle formation and the initial contrail dimensions depend obviously on aircraft and engine properties (Holzäpfel and Gerz, 1999; Sussmann and Gierens, 2001; Lewellen and Lewellen, 2001; Kärcher and Yu, 2009; Voigt et al., 2010). This model accounts for the aircraft wing span s_a, aircraft mass M_a, true air speed V_a, fuel consumption m_F per flight distance, soot number emission index EI_{soot}, and the overall propulsion efficiency η. This efficiency is needed for analysis of the Schmidt-Appleman criterion (SAC) and defined as $\eta = F_a/(m_F Q_{fuel})$ as a function of fuel flow, thrust of engines or drag of aircraft F_a, and fuel combustion heat Q_{fuel} (Schumann, 1996). The soot emission index belongs to the critical model parameters, listed in Table 2. Aircraft usually burn kerosene with water vapor emission index $EI_{H_2O} = 1.25$ and combustion heat $Q_{fuel} = 43.2\,MJ\,kg^{-1}$. Other fuels can be simulated as well, e.g. $EI_{H_2O} = 8.94$ and $Q_{fuel} = 120\,MJ\,kg^{-1}$ for liquid hydrogen (Schumann, 1996).

Type dependent properties are set in module AINIT. The aircraft and operations data are collected from several sources, such as the BADA data set (EUROCONTROL, 2009) and the AERO2K project (Eyers et al., 2004).

2.4 Contrail formation conditions

Each flight segment between consecutive waypoints on which contrails can form is treated as a contrail segment. We use the well-known SAC (Schmidt, 1941; Appleman, 1953; Schumann, 1996). The SAC requires liquid saturation to occur locally in the plume of aircraft exhaust gases mixing with cold ambient air. The maximum threshold temperature T_{LM} is reached when the relative humidity over liquid water in ambient air is at saturation, $U = 1$, $U = RHi\, p_{ice}(T)/p_{liq}(T)$. The saturation pressures over liquid and over ice water surfaces, p_{liq} and p_{ice}, are computed as in Sonntag (1994), see Appendix A3. An often used approximation for T_{LM} (liquid maximum) is

$$T_{LM} = -46.46 + 9.43 ln(G - 0.053) + 0.72[ln(G - 0.053)]^2, \qquad (10)$$

Contrail cirrus model

U. Schumann

with G in units of Pa K^{-1} and T_{LM} in °C (Schumann, 1996), and with errors below 0.07 K for 0.24 Pa K$^{-1} < G < 23$ Pa K^{-1}. Here G is the steepness of the mixing line between engine exit and ambient air in a $p-T$ diagram,

$$G = \frac{c_p p \, EI_{H_2O}}{(M_{H_2O}/M_{air}) Q_{fuel}(1-\eta)}, \tag{11}$$

with specific heat capacity of air $c_p = 1004$ J (kg K)$^{-1}$, ratio of molecular masses of water and air $M_{H_2O}/M_{air} = 0.622$, pressure p, emission index EI_{H_2O} and combustion heat Q_{fuel} of the fuel used, and overall propulsion efficiency η of the aircraft at cruise. All these values are available for analysis within CoCiP. For kerosene driven aircraft at p between 100 and 500 hPa, G varies typically between 0.6 and 4 Pa K^{-1}. Larger values occur for fuels with larger water mass contents.

So far, no such approximation was available for the threshold temperature T_{LC} at $0 < U < 1$. Since T_{LC} has to be computed for each waypoint, we developed a new efficient approximation as presented in Appendix A5.

An alternative contrail threshold criterion avoiding iterative solutions for given T_{LM} has been suggested by Ponater et al. (2002). Instead of $T < T_{LC}$ it requires that the ambient relative humidity U stays above a critical value

$$U_{LC} = \frac{G(T-T_{LM}) + p_{liq}(T_{LM})}{G}. \tag{12}$$

This more efficient variant is used unless T_{LC} is required for analysis.

An explicit criterion for persistency as a function of supersaturation is not necessary in CoCiP. In case of very low temperatures, short-lived contrails may form from the emitted water vapor even in totally dry air. Contrails are surprisingly often found in slightly subsaturated air masses (Rädel and Shine, 2007; Krämer et al., 2009; Voigt et al., 2010). At least at low temperatures, it may take up to an hour until the ice formed initially from emitted water is sublimated, see Appendix A6. Contrails in subsaturated air masses reach small cover and hence contribute little to radiative forcing (Ponater

et al., 1996), nevertheless such contrails may be important when comparing contrail properties to observations (Voigt et al., 2011). Also, soot properties may possibly get changed when processed in contrails (Lee et al., 2010).

2.5 Wake vortex downwash

Since the global climate impact of contrails comes mainly from contrails surviving far longer than the wake vortex phase, we do not resolve the details of the jet and wake dynamics in the first minutes. Instead we use a parametric model to estimate the initial depth D_0, width B_0, and maximum and mean downward displacements Δz_w and Δz_1 such that the follow-on advection and dispersion is approximately consistent with the results of the Gaussian model. After formation of the contrail in the jet of the aircraft engines at point "0", see Fig. 1, the sinking of the contrail with the wake vortex behind the aircraft is estimated from a wake vortex model. The subsequent computations then start from model point "1" at the time and horizontal position of the contrail forming aircraft but at lower altitude, see Fig. 1. The plume model assumes that aircraft wake induced turbulence affecting the initial plume dimensions has ceased at this stage.

A wake vortex sub-model WINIT computes the maximum downward displacement Δz_w of the contrails at the end of the wake vortex phase as a function of aircraft and atmospheric parameters using a parameterization derived from a nondimensional fit to results of the Probabilistic Two-Phase Aircraft Wake-Vortex Model (P2P) (Holzäpfel, 2003). The sinking and decaying wake vortex depends on typical length and time scales of the aircraft, ambient stratification, and ambient turbulence which are defined as

wake vortex separation $b_0 = \pi s_a/4$,
initial circulation $\Gamma_0 = 4M_a g/(\pi s_a \rho V_a)$,
effective time scale $t_0 = 2\pi b_0^2/\Gamma_0$,
initial velocity scale $w_0 = \Gamma_0/(2\pi b_0)$,
and normalized dissipation rate $e_* = (\epsilon b_0)^{1/3}/w_0$,

which are functions of wing span s_a, aircraft mass M_a, true air speed V_a, air density ρ, Brunt-Vaisaila frequency N_{BV}, and turbulent kinetic energy dissipation rate ϵ.

The parameterization distinguishes between strongly and weakly stably stratified conditions: If $N_{BV} t_0 \geq 0.8$:

$$\Delta z_w = 1.49 \frac{w_0}{N_{BV}}, \tag{13}$$

else, with $\epsilon* \leq 0.36$,

$$\frac{\Delta z_w}{b_0} = 7.68(1 - 4.07\epsilon* + 5.67\epsilon*^2)(0.79 - N_{BV} t_0) + 1.88. \tag{14}$$

The maximum sinking Δz_w is larger than the value w_0/N_{BV} for a pure Brunt-Vaisaila oscillation because of additional rotational momentum in the sinking and rotating vortices (Holzäpfel and Gerz, 1999). The influence of ambient turbulence on wake vortex decay enters this model as a function of the turbulent dissipation rate ϵ in the atmosphere. As discussed later, the value of this parameter may vary from 10^{-8} to $10^{-2}\,\mathrm{m}^2\,\mathrm{s}^{-3}$ (Schumann et al., 1995; Gultepe and Starr, 1995). For small dissipation rate, the downwash depth depends only weakly on its value. Here we use Eq. (39), see below, to estimate dissipation as a function of ambient shear. Typical values are of the order $10^{-5}\,\mathrm{m}^2\,\mathrm{s}^{-3}$. Shear is important in particular for small aircraft (Lewellen and Lewellen, 1996).

The wake vortex reaches maximum downward displacement at times which are 5 to 12 times larger then t_0, depending on stratification (Holzäpfel, 2003). Hence, Δz_w is rarely observed in the atmosphere because this occurs up to 50 km behind the aircraft and the measurable wake turbulence is weak at this stage. Nevertheless the empirical fit is consistent with the few existing field and laboratory results, see Fig. 3. Figure 3 contains previously published results and in addition the result computed with the present approximation for one of the largest commercial aircraft (A380) as observed during the CONCERT campaign (Voigt et al., 2010, 2011), with $V_a = 250\,\mathrm{m\,s}^{-1}$, $M_a = 508\,\mathrm{Mg}$, $s_a = 79.8\,\mathrm{m}$, $\rho = 0.39\,\mathrm{kg\,m}^{-3}$, $N_{BV} = 0.012\,\mathrm{s}^{-1}$, $\epsilon = 10^{-5}\,\mathrm{m}^3\,\mathrm{s}^{-2}$. Hence,

$b_0 = 62.7$ m, $t_0 = 30.3$ s, $w_0 = 2.07$ m s^{-1}, $N_* = N_{BV}t_0 = 0.363$, $\epsilon_* = (\epsilon b_0)^{1/3}/w_0 = 0.04$. With these parameters, the above model computes a maximum wake vortex sinking of $Z_* = -\Delta z/b_0 = -4.63$ (see Fig. 3) or $\Delta z_w = 290$ m. This value is close to the observed value of 270 m.

The initial sinking from state "0" to "1" (Fig. 1) is set to

$$\Delta z_1 = C_{z1}\Delta z_w, \quad C_{z1} = 0.25. \tag{15}$$

The center of the contrail starts higher than midway between the initial and maximum sinking distance, partly because of buoyancy. The initial contrail depth D_1 is set to

$$D_1 = C_{D0}\Delta z_w, \quad C_{D0} = 0.5. \tag{16}$$

The initial contrail depth is taken considerably smaller than Δz_w, because initial tests have shown that otherwise the model simulates too large dilution compared to observations. In fact, the initial contrail width B_1 is parameterized,

$$B_1 = N_{dil}(t_c)m_F/[(\pi/4)\rho D_1], \tag{17}$$

so that the dilution N_{dil} at the time $t = t_0$ of wake vortex formation fits an often used empirical function

$$N_{dil}(t) \approx 7000(t/t_s)^{0.8}, \tag{18}$$

with $t_s = 1$ s (Schumann et al., 1998).

For a fleet of aircraft and typical meteorological conditions, Fig. 4 illustrates the initial depth and width results. These scales increase with aircraft mass, as expected. For the same aircraft mass, the initial depth is largest for weak stratification. The initial width is usually far smaller than the depth.

2.6 Initial contrail ice crystal mass concentration

We simulate the contrail ice properties using two plume-bulk ice quantities, the mass mixing ratio I of ice in the contrail, and the total number concentration N of contrail ice

particles per contrail length. We prescribe N and not the volume specific ice number concentration $n = N/A$ because N is conserved during plume mixing.

We assume that the plume vapor is at ice saturation within the effective cross-section area A (Eq. 3) of the contrail plume at all times. Besides for young contrails with low ice mass and low particle concentrations, this assumption is supported for contrails after the vortex formation even for large ambient supersaturation by large eddy simulations (Lewellen and Lewellen, 2001; Unterstrasser and Gierens, 2010a; Paugam et al., 2010) and measurements (Heymsfield et al., 1998). The temperature increase in the plume from combustion heat and later by sublimation heat is small after a few seconds of contrail age, see Appendix A6. Hence, the contrails are assumed to be in thermal equilibrium with ambient air in the wake phase after contrail formation. Otherwise, we would have to solve also a budget equation for heat, and the resolution of vertical oscillations in stratified air would require time steps smaller than N_{BV}^{-1}. These assumptions are essential for efficient simulation. As a consequence, the ice mass content I can be computed form pure thermodynamics.

The initial value I_0 at stage "0" is computed in a module ICEINI as the sum of the water mass emitted by the engines from burning kerosene per flight distance plus the water mass concentration available from humidity in the air mass entrained into the young contrail:

$$I_0 = \frac{\mathrm{EI}_{H_2O} m_F}{(\pi/4)\rho D_0 B_0} + q_0 - q_s(p_0, T_0) \tag{19}$$

Here, q_0 is the ambient humidity (mass ratio) and $q_s(p, T) = (R_0/R_1)p_{ice}(T)/p$ is the saturation humidity at point "0". I_0 is replaced by zero if the above expression gives a negative result (in dry air), and this ends the contrail life cycle for such cases.

During sinking of the contrail with the wake vortex, part of the initial ice mass sublimates because of adiabatic warming (Holzäpfel and Gerz, 1999; Sussmann and Gierens, 1999; Lewellen and Lewellen, 2001). Hence, the ice water mass fraction

Full Screen / Esc

Printer-friendly Version

Interactive Discussion

I_1 in the contrail at stage "1" (at the end of the wake vortex phase) is smaller:

$$I_1 = I_0 - \Delta I_{ad} \tag{20}$$

where

$$\Delta I_{ad} = \frac{R_0}{R_1} \left[\frac{p_{ice}(T_0 + \Delta T_{ad})}{p_1} - \frac{p_{ice}(T_0)}{p_0} \right] \tag{21}$$

and

$$\Delta T_{ad} = T_0 (R_0/c_p)(p_1 - p_0)/p_0, \tag{22}$$

with gas constant R_0 and specific heat capacity c_p of air. Again, the contrail life cycle ends if the above expression gives a negative result (in dry air). Without aircraft emissions, a plume starting at $p_0 = 250$ hPa, $T_0 = 220$ K, with RHi = 1.5 has to descend 400 m according to these equations to reach saturation (RHi=1), in agreement with earlier estimates (Lewellen and Lewellen, 2001; Unterstrasser et al., 2008).

2.7 Initial contrail ice crystal number concentration

The initial number of ice particles is a result of liquid droplets which form by nucleation on emitted and ambient aerosols and which freeze shortly thereafter (Kärcher et al., 1996; Fahey et al., 1999). The local relative humidity at the place of contrail formation in the exhaust plume exceeds liquid saturation, so that liquid droplets form at least on the larger soot particles in the young contrail, which then freeze quickly because they are relatively large (compared to volatiles), and form at low temperature and high relative humidity in the contrail. This nucleation process depends on aerosol properties, mixing, and local temperature and humidity in the plume. This process has been extensively studied with models and measurements (Busen and Schumann, 1995; Schumann et al., 1996; Kärcher et al., 1996; Brown et al., 1997; Jensen et al., 1998b; Kärcher, 1998; Kärcher et al., 1998; Schumann et al., 2002; Paoli et al., 2008; Wong and Miake-Lye, 2010). Ice particle formation is a self-limiting process in which

Contrail cirrus model

U. Schumann

Title Page

Abstract | Introduction

Conclusions | References

Tables | Figures

◄ | ►

◄ | ►

Back | Close

Full Screen / Esc

vapor depletion by the first ice particles limit further nucleation (Jensen et al., 1998b; Kärcher et al., 1998). The initial number of ice particles is essentially determined by the number of soot particles emitted by the engines (Brown et al., 1997; Kärcher, 1998). In principle, also volatile materials, e.g. from sulfuric acid and organic material, contribute to ice formation, however, the contribution of volatile particles is small for typical soot emissions and moderately low temperatures (Kärcher and Yu, 2009). The few existing measurements of ice and soot particle concentrations in young contrails are hardly accurate enough to test this assumption (Schumann et al., 2002). However, analysis of experiments for different fuel sulfur contents show that the number of ice particles in young contrails increases by only about a factor of 1.3 for an increase in fuel sulfur content from 6 to 2800 mg g^{-1} (Brown et al., 1997; Kärcher et al., 1998; Kärcher and Yu, 2009; Schumann et al., 2002). Volatile particles contribute a larger share to ice particles for low soot particle emissions (below 10^{14} kg^{-1}) and low ambient temperatures (below 210 K) (Kärcher et al., 2009a).

Hence, the initial number N_0 of ice particles per contrail length in the freshly formed contrail at stage "0" is assumed to be determined by soot, and prescribed (in a module ICEINI) as a function of the soot emission index and the fuel consumption rate per flight distance,

$$N_0 = EI_{soot} m_F. \tag{23}$$

Contributions of ice particles from other sources (such as volatiles or aerodynamic contrails (Gierens et al., 2009; Kärcher et al., 2009b) could be included when proper parameterizations become available.

Only a fraction of the ice crystals survives the transition between stages "0" and "1". Ice particle loss by coagulation from Brownian motion after the jet phase is small (Gierens, 1996; Kärcher, 1998; Paoli et al., 2008). However, important loss is caused in the sinking vortex (Sussmann and Gierens, 1999; Lewellen and Lewellen, 2001; Unterstrasser et al., 2008). Any initial supersaturation gets reduced by deposition of humidity on ice particles quickly and before the vortex has reached its lowest altitude.

Contrail cirrus model

U. Schumann

Full Screen / Esc

Printer-friendly Version

Interactive Discussion

The sinking vortex with adiabatic heating causes local subsaturation around the ice particles. As a consequence, the ice particles sublimate and some of them disappear (Unterstrasser and Sölch, 2010). Also turbulent detrainment from the sinking wake vortex in dry air may contribute to particle losses. These losses depend on aircraft type, aircraft speed and mass, soot and heat emissions, humidity, temperature, shear, stratification, ambient turbulence, and particle sizes (Huebsch and Lewellen, 2006; Unterstrasser et al., 2008; Unterstrasser and Gierens, 2010a,b).

Hence we prescribe a "survival factor" f_{surv} of ice particles remaining after the vortex phase:

$$N_1 = f_{surv} N_0. \tag{24}$$

As a first approximation we assume that the surviving particle fraction is in line with ice mass changes, i.e., we use the simple approximation

$$f_{surv} = I_1/I_0, \ 0 < f_{surv} < 1. \tag{25}$$

Implicitly this is a function of ambient humidity and temperature. The survival factor varies between 1 and about 0.7. LES models compute smaller factors (Unterstrasser et al., 2008; Kärcher et al., 2009a). The difference is partly caused by the small sinking distance z_1 of the bulk plume (in contrast to maximum sinking), see Eq. (15). In principle, ice mass and ice number evolve differently (Gierens and Bretl, 2009) implying different survival factors. Therefore, we cannot exclude at this stage that smaller survival factors might give better results. Anyway, the ratio I_1/I_0 is aircraft dependent. Possibly, the survival factor depends mainly on the difference to SAC threshold conditions, see Fig. 5 because the plume starts sinking with humidity depending on this threshold.

2.8 Time integration and segment trajectories

After contrail initialization at stage "1" slightly below the aircraft track, the contrail trajectories and properties are followed with the Gaussian plume model until a given time

of analysis or until final disappearance of the contrail at any later stage "2" (Fig. 1). This evolution is computed by numerical integration of the Lagrangian contrail position and properties in a sub-module INTCOCIP. The integration in time is performed over a sequence of time steps from t to $t + \Delta t$. For global simulations we may use large time steps, of the order of 1 h, for computational efficiency. The ice mass and particle concentrations have to stay non-negative. Hence the integration scheme has to be accurate, positive definite and unconditionally stable.

The state of the contrail is characterized by a state vector $X(t,i)$, $i = 1, 2, \ldots, N_W$, containing $X = x, y, p, \sigma, I, N$, including horizontal positions, static pressure, plume parameters, mass specific ice mass content, and total number of ice particles per contrail length. All components of X depend on position in space and time t. The integration is performed for each contrail segment between two successive contrail points.

For the trajectoy part $X = (x, y, p)$ of the state vector, we could use the standard second-order two-step Runge-Kutta scheme (Abramowitz and Stegun, 1964). Lagrangian models for trajectory calculation in meteorology often use a first order or the two-step second order scheme, which is unconditionally stable for smooth wind fields, without iterations (Danilin et al., 1994; Nair et al., 2003; Stohl et al., 1998, 2001; Wernli and Davies, 1997). However, for accuracy at large time steps and because of strong nonlinearities of other plume parameters, we apply the Runge-Kutta scheme with a few (2–6) iteration steps. Accuracy tests have shown that the time step Δt does not need to be taken much smaller than the time step of the available NWP results. This is very important for the efficiency of the scheme.

The integration over one step is performed in a sub-module RUNGE. Time derivatives of X are computed in module DTCONTR. For each time step, these routines internally assume that the input was given for a time point "1" and the integration ends after one step at a time "2", with $\Delta t = t_2 - t_1$.

The Runge-Kutta scheme starts with a predictor step:

$$\tilde{X} = X(t) + \Delta t \frac{\partial}{\partial t} X(t), \tag{26}$$

Contrail cirrus model

U. Schumann

Printer-friendly Version

Interactive Discussion

followed by one or several corrector steps,

$$X(t + \Delta t) = X(t) + \frac{\Delta t}{2} \left[\frac{\partial}{\partial t} X(t) + \frac{\partial}{\partial t} \tilde{X} \right], \tag{27}$$

$$\tilde{X} := X(t + \Delta t). \tag{28}$$

The time derivatives of the positions are computed from the wind vector (U, V, ω) and
5   ice particle terminal fall speed V_T,

$$\partial x / \partial t = U, \, \partial y / \partial t = V, \, \partial p / \partial t = \omega + g \rho V_T. \tag{29}$$

Here, we assume that the contrail follows the mid point of the bulk of the ice particles
under sedimentation so that the point "2" gets displaced downwards according to the
terminal fall speed V_T. The other components of X are integrated quasi analytically as
10 described below.

For numerical integration, one has to keep the way-point variables at the start of the
time-step, at the intermediate level denoted with tilde, and at the end of the time step.
Thereafter, older results may be forgotten, unless required for later analysis. For old
contrail waypoints originating from the same aircraft at times before t_1, integration is
15 performed with the given time step. For new contrail waypoints getting initiated within
the time interval, a smaller time step is used to reach t_2. Polewards of $|y| > 80°$, these
calculations are performed in Cartesian coordinates to avoid the pole singularity, see
Appendix A7. This seems to be common practice in trajectory models (Nair et al.,
2003), but details have not been published. Moreover, care is needed to make sure that
20 the coordinates stay consecutive when passing the date line (at $\pm 180°$) for periodicity
in longitude (see Appendix A8).

It should be noted that advection with horizontally diverging wind fields changes the
segment length L between waypoints. Individual waypoints may depart from each other
considerably over the time of integration, so that L changes by factors of order 0.5 to 2.
25 Because of continuity, horizontal divergence is connected with convergence in vertical
planes and this reduces the cross-section area. The change in segment length $L(t)$

Full Screen / Esc

Printer-friendly Version

Interactive Discussion

is taken into account when integrating cross-sections and the particle concentration N per unit contrail length in time. Segment length is computed efficiently as square root of the sum of squared geographical coordinate differences (in meters), except in polar regions where great circle equations are used (http://www.astro.uu.nl/~strous/AA/en/reken/grootcirkel.html).

For illustration, Fig. 6 shows contrails analyzed for global traffic and for ECMWF NWP data for a time slice at an arbitrary analysis time 06:00 UTC for a day in June 2006. This analysis includes contrails with maximum age of $< 36\,\mathrm{h}$. The code actually reads NWP data for a 5-days period including the period from 36 h before and until the analysis time. The plot shows in red the contrails existing at the analysis time. In addition the flight paths of aircraft cruising in cold and humid air causing at least short contrails are plotted for the 3-h time interval before the analysis time. Most of the contrails plotted in red originate from recent flights but some from flights that occurred more than one day (and up to 36 h) before. Young contrails experience little advection, but older contrails get advected partly over large distances as can be seen from the separation between red and black lines. Contrails occur in clusters in regions with supersaturation. Many of these regions also include natural cirrus. This coexistence of cirrus and contrails will be taken into account when analyzing the radiative forcing and contrail cirrus cover. The results will be discussed further below.

2.9 Evolution of Gaussian plume parameters

The initially symmetrical Gaussian contrail inclines and grows in cross-section area A with time because of shear (vertical gradient of the horizontal velocity normal to the contrail axis), $S = dV_n/dz$, of either sign, and horizontal and vertical diffusivities, D_H and D_V, and possibly shear diffusivity D_S (of either sign) with the constraint

$$D_S^2 \leq D_V D_H \tag{30}$$

for positiv definite solutions. As derived by Konopka (1995), with extension for variable segment length $L(t)$, the temporal evolution of $\sigma(t)$ for constant values of S, D_H, D_V,

D_S follows from

$$\sigma_{yy}(t + \Delta t) = [\tfrac{2}{3}S^2 D_V \Delta t^3 + (S^2 \sigma_{zz}(t) + 2D_S S)\Delta t^2$$
$$+2(D_H + S\sigma_{yz}(t))\Delta t + \sigma_{yy}(t)][L(t)/L(t+\Delta t)]^2 \qquad (31)$$

$$\sigma_{zz}(t+\Delta t) = 2D_V \Delta t + \sigma_{zz}(t) \qquad (32)$$

$$\sigma_{yz}(t+\Delta t) = [SD_V \Delta t^2$$
$$+(2D_S + S\sigma_{zz}(t))\Delta t + \sigma_{yz}(t)]L(t)/L(t+\Delta t). \qquad (33)$$

The equations assume that only the horizontal plume scales change inversely to the segment length $L(t)$, while the vertical stays constant. The vertical to horizontal divergence ratio could be estimated from the NWP model, if necessary.

The contrail model starts from initial values $\sigma_{yy}(t=0) = B^2/8$, $\sigma_{zz}(t=0) = D^2/8$, $\sigma_{yz}(t=0) = 0$, see Eqs. (16, 17). Thereafter, these equations are used with equal-weight algebraic mean values of D_H, D_V, D_S and S at times t and $t + \Delta t$ to integrate over time to $t + \Delta t$. (The accuracy of the method might be improved by weighting the contributions differently.) Linear diffusivity changes with time could be treated analytically (Konopka, 1995), but any parameterization of the diffusivities as a function of plume scales makes the equations nonlinear. Hence, the solutions are no longer exact and the accuracy becomes time-step dependent. However, the integration is unconditionally stable and guarantees positive definite solutions of σ.

In the code we compute A from Eq. (3) for each waypoint. However, the analytical solution for A is

$$A(t+\Delta t) = 2\pi\big[\tfrac{1}{3}S^2 D_V^2(\Delta t)^4 + \tfrac{2}{3}S^2 D_V \sigma_{zz}(t)(\Delta t)^3$$
$$+(2SD_V \sigma_{zz}(t) - 2SD_S \sigma_{zz}(t) + 4D_H D_V - 4D_S^2)(\Delta t)^2$$
$$+(2D_V \sigma_{zz}(t) + 2D_H \sigma_{zz}(t) - 4D_S \sigma_{yz}(t))\Delta t$$
$$+\sigma_{yy}(t)\sigma_{zz}(t) - \sigma_{yz}^2(t)\big]^{1/2}. \qquad (34)$$

Contrail cirrus model

U. Schumann

Full Screen / Esc

Except for a factor 2, Eq. (34) is the same as Eq. (9) of Dürbeck and Gerz (1996). It should be noted that shear alone does not increase the cross-section A. It makes the elliptical contrail cross-section wider but also thinner. But in combination with turbulent diffusion, mainly vertically, shear enhances mixing considerably. The vertical diffusivity is most important for growth, since for $D_V = 0$ ($D_S = 0$ because of Eq. 30), Eq. (34) reduces to $A(t + \Delta t) = 2\pi[2D_H\sigma_{zz}\Delta t + \sigma_{yy}\sigma_{zz} - \sigma_{yz}^2]^{1/2}$ regardless of the shear value. The value D_S looses importance for $A(t)$ when shear increases (Dürbeck and Gerz, 1996). The same would be true for D_H if it were shear-independent.

2.10 The turbulence model

Most of the contrails form in the upper troposphere or lower stratosphere where strong winds, shear and stratification prevail (Birner et al., 2002; Houchi et al., 2010; Manney et al., 2011). Shear production of turbulence is driven by total shear S_T, while plume distortion follows the vertical shear S of the plume-normal velocity,

$$S_T^2 = (dU/dz)^2 + (dV/dz)^2, S = dV_n/dz. \tag{35}$$

The Brunt-Vaisaila frequency N_{BV} measures stratification, and the Richardson number Ri the ratio of both.

$$N_{BV}^2 = (d\Theta/dz)g/\Theta, Ri = N_{BV}^2/S_T^2. \tag{36}$$

Molecular diffusion is negligible at plume scales because of large Reynolds numbers. The state of turbulence in this region is highly anisotropic and often composed of large-scale horizontal quasi two-dimensional motions with little vertical motions. These motions are composed of wavy motions and intermittent turbulent spots (Dewan, 1979; Dörnbrack and Dürbeck, 1998; Riley and Lindborg, 2008). The kinetic energy spectrum follows a −3-power law for the large scales and a −5/3-power law for smaller scales, suggesting either 2d turbulence or 3d inertial range turbulence, but local isotropy requires smaller scales (Nastrom and Gage, 1985; Riley and Lindborg, 2008). Wavy

motions advect and distort the plumes without mixing. As mentioned before, the dissipation rate is often small (Schumann et al., 1995; Kantha and Hocking, 2011; Gultepe and Starr, 1995; Clayson and Kantha, 2008). Vertical motions in stratified air are limited by kinetic energy convertible to potential energy (buoyancy scale $L_B = w'/N_{BV}$). Overturning turbulence occurs only for scales below the Ozmidov scale $L_{Oz} = \epsilon^{1/2} N_{BV}^{-3/2}$ (Riley and Lindborg, 2008). Only dissipating turbulence causes essential mixing between plume air and ambient air. The horizontal scales B of aged contrails are often in the transition region between the 2d-turbulence controlled by shear and stratification and even the smaller vertical scale D is often far too large for being within the isotropic inertial range turbulence. Estimates of kinetic energy from subgrid scale models require knowledge of the Richardson number and the length scales of mixing and dissipation (Schumann, 1991), see Appendix A9, which is uncertain for NWP grids with grid scales far outside the inertial range. Turbulence experienced by cruising aircraft (including but not restricted to clear air turbulence) can be estimated from coarse NWP fields (Sharman et al., 2005; Frehlich and Sharman, 2010) but the scaling of this turbulence (composed of waves and turbulence) to plume scales has still to be investigated.

Since the plume trajectory meanders with ambient air motions at the scales of the contrail segments by advection in a Lagrangian manner, internal mixing is limited to motions at segment scales. The assumption of the same constant diffusivities for young and aged contrails would certainly not be appropriate. Instead the diffusivities depend on shear and stratification at plume scales. The diffusivity model used here is based on classical fluid dynamics arguments such as Prandtl's mixing length for shear driven mixing and equilibrium between dissipation and energy production by shear and (negative) buoyancy due to vertical mixing in stably stratified fluids (Hunt et al., 1988; Schumann, 1991; Schumann and Gerz, 1995).

Vertical diffusivities derived from measurements in the free atmosphere range typically from 0 to $1\,m^2\,s^{-1}$ (Pavelin et al., 2002). Only slightly larger values occur locally in buoyant plumes (Pisso et al., 2009) or in breaking gravity waves (Dörnbrack and Dürbeck, 1998). Smaller values ($0-0.6\,m^2\,s^{-1}$) should be effective at plume scales.

The horizontal diffusivities within a Lagrangian plume are of order $5-20\,\mathrm{m^2\,s^{-1}}$ for young plumes but grow large up to values of the order $10^4\,\mathrm{m^2\,s^{-1}}$ for wider and thicker plumes (Schumann et al., 1995; Dürbeck and Gerz, 1996; Pisso et al., 2009). Large eddy simulations are prone to numerical diffusion in particular in the presence of shear and stratification (Dürbeck and Gerz, 1995, 1996). They compute mixing in an Eulerian frame and do not identify the Lagrangian and scale-dependent mixing. Differences between analytical plume models and large eddy simulations (Naiman et al., 2010; Unterstrasser and Gierens, 2010a) can hardly be used to constrain the model parameters for diffusivities, therefore.

Vertical mixing can be parameterized either for given dissipation rate ϵ or for given root-mean-square (rms) vertical turbulence fluctuations w'_N (Schumann and Gerz, 1995). Here, we prescribe $w'_N = 0.1\,\mathrm{m\,s^{-1}}$ to compute

$$D_V = \frac{c_V}{N_{BV}} w'^2_N + f_T V_T D_{eff}, c_V = 0.2, f_T = 0.1, \tag{37}$$

$$D_H = c_H D^2 S_T, D_S = 0, c_H = 0.1. \tag{38}$$

(To avoid division by zero, we constrain $N_{BV} > 0.001\,\mathrm{s^{-1}}$.) The value of w'_N is related to the dissipation rate by

$$\epsilon = A_S w'^2_N S^2, A_S = 0.5. \tag{39}$$

(Hunt et al., 1988; Schumann and Gerz, 1995). Typical shear values ($S = 10^{-3}$ to $10^{-2}\,\mathrm{s^{-1}}$) and typical stratifications, $N_{BV} = 0.01$ to $0.03\,\mathrm{s^{-1}}$, for $D = 100\,\mathrm{m}$, imply $D_V \approx 0.07-0.2\,\mathrm{m^2\,s^{-1}}$, $D_H \approx 1-10\,\mathrm{m^2\,s^{-1}}$, and $\epsilon \approx 5\times10^{-7}-0.05\,\mathrm{m^2\,s^{-3}}$. These values are within the range of measured data (Schumann et al., 1995). The buoyancy and Ozmidov scales are astonishingly small in this range, $L_B \approx 3-10\,\mathrm{m}$, $L_{Oz} \approx 0.07-0.7\,\mathrm{m}$, i.e., not much larger than the Kolmogorov scale $L_K = (\nu^3/\epsilon)^{1/4} \approx 0.3-6\,\mathrm{mm}$ where kinematic viscosity ν becomes important.

For quasi-steady homogeneous turbulence at low Richardson numbers, c_V is a constant and $c_V = 0.2$ is supported by atmospheric boundary layer measurements (Hunt, 1985). For large values of Ri, c_V decreases (Schumann and Gerz, 1995) but N_{BV} gets large and hence D_V gets small in this limit anyway, so that this decrease is less important. D_H would become unrealistically large when replacing the mixing length scale D in Eq. (38) by B. The coefficient $c_H = 0.1$ is a free adjustable model coefficient. Its value is of minor importance because mixing is mainly controlled by the product of $D_V S$ and less by D_H, see Eq. (34). The essential free parameter is w'_N which measures the turbulence level at flight altitude.

Ice particles in contrails differ from passive tracers in that they sediment, grow or sublimate, release latent heat, and interact with radiation. Larger ice particles efficiently increase the effective depth of a contrail by sedimentation (Schumann, 1994; Atlas et al., 2006). We account for the vertical growth of the contrail cross-section by increasing the vertical diffusivity for given fall velocity V_T (as computed below). Also f_T is an important adjustable parameter.

Except for the constraint $D_S^2 \leq D_V D_H$, little is known about the off-diagonal "shear" diffusivity D_S (which has either sign). The shear diffusivity increases A only if $SD_S < 0$, see Eqs. (34) and (33). This sign is imposed by shear driven correlations between vertical and horizontal velocity fluctuations.

$$D_S = -C_{DS}(D_V D_H)^{1/2} S/|S|. \tag{40}$$

As noted before, the value of D_S is unimportant for strong shear. Therefore, in the absence of further information, we set $D_S = 0$.

The shear S is determined numerically from the wind field provided by the NWP model. The vertical grid spacing Δz in such models is usually far larger than the contrail depth D. Hence, the magnitude of the shear at contrail scale may be larger because of shear by subgrid velocity fluctuations. The effective vertical resolution Δz_{eff} in respect to shear is usually larger than the numerical resolution Δz. By comparisons to radiosondes, Houchi et al. (2010) show that the effective vertical resolution of the

Full Screen / Esc

ECMWF model for shear is about $\Delta z_{eff} = 2000$ m. We therefore use a shear value which is enhanced by a factor

$$f_S = (1 + (\Delta z_{eff}/D)^n)/2, \, n \geq 0. \tag{41}$$

This can be justified by considering the relationship between the mean squared shear and the kinetic energy spectrum $E(k)$ of homogeneous turbulence versus wave number k (Lilly, 1967):

$$\langle (\frac{\partial u}{\partial z})^2 \rangle \simeq \int_0^{\pi/\Delta z} k^2 E(k) \, dk \tag{42}$$

The angular brackets denote a suitable statistical mean operator. For $E(k) \sim k^{-m}$ follows

$$\langle (\frac{\partial u}{\partial z})^2 \rangle \sim (D/\Delta z)^{3-m}. \tag{43}$$

For isotropic turbulence in Komogorov's inertial subrange, $m = 5/3$, and hence $n = 2/3$. For stably stratified flows one expects steeper spectra, e.g., $m = 3$, and, hence, $n = 0$. The true value of n needs to be determined empirically (Adelfang, 1971; Riley and Lindborg, 2008). For this model, we assume $n = 1/2$.

The lower panel of Fig. 7 illustrates the order of magnitude of the contrail mixing properties computed this way. The vertical and horizontal diffusivities, D_V and D_H are small initially and grow with time when the contrails spread. D_H is about 10 to 100 times larger than D_V. The details depend on age, shear, and stratification and, for high supersaturation, also on sedimentation. The numbers for the early period (0.01–0.5 m^2 s^{-1} vertically and 5–20 m^2 s^{-1} horizontally) are fully consistent with estimates derived from measurements and large eddy simulations (Dürbeck and Gerz, 1996; Schumann et al., 1995). Also the later values are consistent with observations (Pisso et al., 2009). The thickness and width values, D and B, are of the right order of magnitude compared to ground-based lidar and satellite observations (Detwiler and Pratt, 1984; Freudenthaler et al., 1995; Duda et al., 2004; Atlas et al., 2006; Immler et al., 2008). More detailed comparisons have still to be made.

Contrail cirrus model

U. Schumann

Full Screen / Esc

Printer-friendly Version

Interactive Discussion

2.11 Contrail ice mass integration in time

The ice content changes with time according to mixing of the water mass mixing ratio in the plume with humidity from the ambient air. To simulate this process, we consider the mass budgets of contrail air mass $M = \rho AL$ and contrail water mass $M_{H_2O} = M(I + q)$ per contrail segment. The humidity q inside the plume is assumed, as before, at ice-saturation, $q = q_s$.

The air mass $M(t_+)$ at $t_+ \equiv t + \Delta t$ is

$$M(t_+) = \rho(t_+)A(t_+)L(t_+). \tag{44}$$

Here $\rho(t_+)$ is computed for given ambient pressure and temperature at t_+, and the contrail cross-section $A(t_+)$ from Eq. (3). The segment length L is computed from the waypoint geometry.

The water mass M_{H_2O} in the segment is composed of contrail water in the ice phase and water in the vapor phase at ice-saturation. The water mass budget changes by mixing with humid ambient air. The ambient air contains water vapor at mass specific concentration q_a, and it may be supersaturated or subsaturated. Hence, at the end of the time step, the amount of water mass in the contrail is

$$M(t_+)(I(t_+) + q_s(t_+)) = M(t)(I(t) + q_s(t)) + \Delta M q_a, \tag{45}$$

with contrail mass change $\Delta M = M(t_+) - M(t)$, and ambient humidity $q_a = (q_a(t_+) + q_a(t))/2$ on average during the time step. We do not include ice from ambient cirrus and ignore the latent heat release for phase changes, because the resultant temperature changes are small, see Appendix A6. As a consequence, we find

$$I(t_+) = [M(t)(I(t) + q_s(t)) + \Delta M q_a]/M(t_+) - q_s(t_+). \tag{46}$$

Equations (44, 46) are used in CoCiP in their discrete form to compute $M(t_+)$ and $I(t_+)$ for each time step. In case of mixing with subsaturated ambient air and for decreasing saturation vapor inside the plume, the contrail may dry out. In this case, we set $I(t_+)$ to zero.

Here we could distinguish contrails inside and outside the cloud covered part of a NWP grid cell, as assumed in the ECMWF model. Tompkins et al. (2007) assumed ice saturation inside the cloudy part of the cell, $q_a = q_s$. Outside the cloudy part, $q_a = (q - Cq_s)/(1 - C)$, where C ist the cloud cover in the grid cell. However, assuming that contrails occur uniformly inside the grid cell, with a share C inside clouds and a share $1 - C$ outside clouds, implies that the ambient humidity q_a equals on average the grid mean value, $q_a = q$. Still, there could be differences in the contrail properties inside and outside of clouds because of nonlinearities. Full treatment of such differences would require considering two types of contrails, within and outside cloudy parts of a grid cell. For simplicity, we ignore these differences in the present CoCiP version.

For interpretation we note that Eqs. (44, 46) are discrete representations of

$$dI/dt = (dM/dt)(q_a - q_s - I)/M - dq_s/dt. \tag{47}$$

We see that this differential equation describes the uptake of ice water mass from the ambient air in supersaturated air masses and the loss of ice water in subsaturated air masses according to the change in contrail mass $M(t)$. The ice water content of the contrail adapts to changes of saturation humidity inside the contrail with given plume mass. The contrail mass and the ice content grow mainly by mixing with ambient air masses. If the ambient air is supersaturated, this supersaturation of the air entrained into the plume is converted to ice. If the ambient air is subsaturated, ice particles in the plume sublimate keeping the mixed plume in ice saturation until all ice is consumed. For $q_a = q_s$, we have $dI/dt = -I(dM/dt)/M$, i.e., the ice mass content gets distributed over a growing plume mass with decreasing concentration. Moreover the ice water content of the contrail adapts to changes of saturation humidity due to temperature or pressure changes inside the contrail with given plume mass. Finally we note that $I = $ const in this approximation for constant ambient conditions, as it should.

The lower panel of Fig. 7 shows that the ice water content of the contrails at a given time instant varies little with their ages. In fact, the IWC is mainly a function of ambient ice supersaturation and temperature. Temperature determines the amount of water

mass condensable for given relative humidity, consistent with empirical relationships (Schumann, 2002; Schiller et al., 2008), see Fig. 8.

2.12 Contrail life time and ice number integration

For given ice water content I and total number of ice particles N, we compute the ice particle number concentration per volume n and the volume-mean ice particle radius r (needed for sedimentation and optical depth computations)

$$n = N/A, \tag{48}$$

$$r = [\rho I / (n \rho_{ice} 4\pi/3)]^{1/3}. \tag{49}$$

Here, $\rho_{ice} = 917\,\mathrm{kg\,m^{-3}}$ is a commonly used bulk density of ice particles. Mixing of air between the contrail plume and ambient air conserves N but reduces n by spreading the ice particles over an increasing plume cross-section.

Without microphysical loss processes (and without nucleation, without mixing with ambient cirrus, and for constant segment length L) the total number N of ice particles remains conserved. (The change in segment length $L(t)$ is taken into account, see Eq. (58), later). As a consequence, contrails would stay infinitely for constant ice supersaturation, although getting thinner with time.

The life-time of contrail clusters should be similar to the lifetime of ice supersaturated regions (ISSR) (Gierens et al., 1999). However there are important differences: The lifetime of contrails is shorter because flight routes only exceptionally start when the air mass becomes supersaturated first. The lifetime of individual contrails may be shorter than the lifetime of contrail clusters. Moreover the phase speed of contrails and ISSR regions is basically different. Contrails get advected with the wind while ISSR regions may be stagnant (at mountains) or move slower (in the upward motion branch of cyclones, i.e., in so-called conveyor belts).

The life time of ISSR has been estimated from observations to be of the order of hours (Immler et al., 2008). A mean flight path length in ISSR of 150 km, with a standard deviation of 250 km, was derived from humidity measurements onboard commercial aircraft (Gierens and Spichtinger, 2000); hence, there were many small ISSR regions. The longest distance flown inside an ISSR extended over more than 3700 km (Gierens and Spichtinger, 2000). The mean values are consistent with observed contrail cluster diameters of a few 100 km (Mannstein et al., 1999). If age scales with this length and with the mean wind speed (possibly of order $50 \, \mathrm{m \, s^{-1}}$), a maximum ISSR age of about a day is to be expected, but most have likely shorter life times. In two cases-studies, at different scales, the life time derived from ECMWF trajectories was 6 and 24 h (Spichtinger et al., 2005b,a). Values exceeding one day are consistent with contrail cluster observations (Bakan et al., 1994).

Here, we estimate the life-time of ISSR regions by computing the age of trajectories which start at aircraft waypoints satisfying the SAC in ice supersaturated air and last until the ambient humidity drops below ice saturation. This aircraft-related ISSR-life-time is not the life-time of ISSR per se, but the the life-time of ice supersaturation relevant for contrails. For this purpose we use the advection scheme for a passive tracer (without sedimentation) with ECMWF data for three days in June 2006. Most of such trajectories end after less than one hour, see Fig. 9, the mean, median, and maximum (mean, med, max) ages of these aircraft-related ISSR trajectories are computed this way as 9.5 h, 7.3 h, and >36 h, respectively. Apparently the age frequency distribution follows an exponential function. Based on such a fit the mean and median ages are 14.6 and 10.1 h. Simulated ISSR lifetimes exceeding 24 h are found for about 1 % of all flights, which is not unrealistic (Bakan et al., 1994).

When we apply CoCiP without particle number loss processes we compute even larger ages, see Fig. 9. The mean, med, max ages of these contrails would be 11.2 h, 8.7 h, >36 h. The larger life time can be explained by the reservoir of ice water built up while staying in the ISSR, which is maximum just when the ISSR regime ends, and which takes time to sublimate. At this time t, the contrails have large cross-sections

Contrail cirrus model

U. Schumann

Full Screen / Esc

Printer-friendly Version

Interactive Discussion

$A(t)$. It takes a further time of order $\tau_{\text{dil}} = A/(dA/dt)$ to dilute the plume to subsaturation. For dilution following a power-law with time, $A(t) = A_0 t^n$ and for $n \approx 0.8$ (Schumann et al., 1998), the mixing time $\tau_{\text{dil}} = t/n$ is large and the total contrail age $t + \tau_{\text{dil}}$ could reach twice the age of ISSR masses.

5　　The lifetime of contrails is highly variable (Detwiler and Pratt, 1984). Contrail ages up to 18 h and possibly more have been observed (Bakan et al., 1994; Minnis et al., 1998; Haywood et al., 2009). These ages may be exceptions, not the rule. Contrails were traced in time with data from geostationary (Duda et al., 2001, 2004; Vazquez-Navarro, 2009) and polar orbiting satellites (Atlas et al., 2006). Contrails become first

10　visible in these data after a dwell time of about 0.5–1 h, depending on satellite resolution (Atlas and Wang, 2010). Contrail clusters were often followed for 2–5 h (Duda et al., 2001, 2004). An automatic contrail-tracking algorithm identified many contrails in METEOSAT satellite scenes with mean, med, max ages (without this dwell time) of 51 min, 20 min, 14 h, respectively (Vazquez-Navarro, 2009). Hence, we expect me-

15　dian contrail lifetimes of order of a few hours, definitely shorter than what is computed without losses.

　　Therefore, we add particle loss models to CoCiP. So far, the model contains three of them:

$$(dN/dt)_{\text{loss}} = (dN/dt)_{\text{turb}} + (dN/dt)_{\text{agg}} + (dN/dt)_{\text{meso}} \tag{50}$$

20　Loss processes include (turb:) spectral broadening by turbulent mixing (Kärcher et al., 2009a), (agg:) sedimentation and sedimentation-induced aggregation (Sölch and Kärcher, 2010), and (meso:) losses induced by turbulent humidity fluctuations by mesoscale turbulence and gravity waves (Kärcher and Ström, 2003) and possibly plume turbulence (Gierens and Bretl, 2009; Unterstrasser and Gierens, 2010a). Also

25　radiative heating of the contrail plume and of individual (large) ice particles may contribute to particle losses (Gierens, 1994; Chlond, 1998; Jensen et al., 1998a; Unterstrasser and Gierens, 2010b). Efficient treatment of radiative heating is possible (similar to radiative forcing, see Sect. 2.14), but not considered in this paper (Schumann

et al., 2010). We note that the humidity in aged contrails may deviate from saturation because of low ice particle concentration. This may contribute to an overestimate of ice mass content and the life-time of contrails.

Mixing of contrails with dry ambient air masses was considered for ice mass in the Sect. 2.11. If the ice size distribution would be narrow and if the plume is well mixed, then it seems conceivable that the number of ice particles stays constant until all ice mass is sublimated, when all particles disappear suddenly. However, this is not realistic (Gierens and Bretl, 2009). While growth of particles would narrow the size distribution, turbulent mixing of cloud air masses with particles of different sizes tends to broaden the size distribution (Kärcher et al., 2009a). Eventually, mixing causes some of the smaller particles to sublimate. We roughly model this with the first loss term, "turb",

$$(dN/dt)_{\text{turb}} = -E_T \left(\frac{D_{\text{H}}}{\max(B,D)^2} + \frac{D_{\text{V}}}{D_{\text{eff}}^2} \right) N \tag{51}$$

with $E_T = 1$ as an adjustable parameter. The maximum function avoids large losses for the initially narrow plume, when $B < D$, because the initial losses are included in the survival factor, Eq. (24). The scale D_{eff} is used instead of D because it enhances the loss for vertically thin contrails. Parameter studies with and without this and the other loss models, show that the "turb" part contributes to losses relatively to all loss terms most strongly at low ice supersaturation.

Sedimentation limits the lifetime of contrails for high ambient supersaturation (Schumann, 1996; Unterstrasser and Gierens, 2010a). During sedimentation, large falling particles may collide and aggregate with smaller ice particles so that the total number of ice particles N decreases. In a size-resolved model, with n_i representing the number density of ice particles in a size range r_i to r_{i+1}, the aggregation process could be parameterized by a rate equation (e.g., Pruppacher and Klett, 1997; Sölch and Kärcher, 2010)

$$(dn_k/dt)_{\text{agg}} = \frac{1}{2} \sum_{i+j=k} K_{ij} n_i n_j - n_k \sum_{j=1}^{\infty} K_{kj} n_j, \tag{52}$$

with rate coefficients

$$K_{ij} = E_A \pi (r_i + r_j)^2 |V_i - V_j|, \tag{53}$$

accounting for aggregation due to collision of particles of different sizes r_i and different fall speeds V_i.

5   Since we have no explicit information on the particle size spectrum, we assume that the size spectrum in the contrails has a width of order r, so that $(r_i + r_j)^2 \approx 4r^2$, and $|V_i - V_j| \approx V_T(2r) \approx 2V_T(r)$. Hence, an approximate aggregation rate as a function of mean particle size r is

$$(dN/dt)_{\text{agg}} = -E_A 8\pi r^2 V_T N^2/A, \tag{54}$$

10   with an adjustable model parameter $E_A = 1$.

The terminal fall velocity $V_T(r, T, p)$ is computed using the Stokes-Cunningham solution for small crystals ($r < 5\,\mu$m) (Pruppacher and Klett, 1997) and a parameterization for rough hexagonal solid column ice crystals (Mitchell and Heymsfield, 2005) otherwise, as described in Sölch and Kärcher (2010). Most particles stay small with small
15   fall speeds. Once they grow and start sedimenting, the plume deepens (and widens by shear) and more water vapor becomes available for deposition. Hence, the contrail life cycle ends quite suddenly when sedimentation starts to become effective. The coagulation efficiency E_A may depend on temperature (Sölch and Kärcher, 2010). However, the aggregation rate is smaller for lower temperatures anyway, because of lower ice
20   water content and smaller particles, therefore.

Finally, we roughly parameterize the effect of sub-grid scale vertical velocity fluctuations w'_{meso}, e.g. from mesoscale turbulence and gravity waves (Kärcher and Ström, 2003). The velocity fluctuations induce temperature fluctuations depending on vertical stratification and mixing. For adiabatic vertical motion of a contrail parcel,
25    $T'_{\text{meso}} \approx w'_{\text{meso}} dT/dz$. Particles are assumed to get lost when T'_{meso} becomes large. In place for a better scale still to be found, we compare to the temperature change for doubling ice mass (Pruppacher and Klett, 1997),

$$\Delta T_c = (R_1 T^2 / L_s). \tag{55}$$

Here, $L_s \approx 2.8 \times 10^6 \, \text{J kg}^{-1}$ is the latent heat of sublimation and $R_1 = 461.5 \, \text{J(K kg)}^{-1}$ the gas constant for water vapor; typically, $\Delta T_c \approx 9 \, \text{K}$. Note that w'_{meso} is different from w'_N, because it includes wave motions. Moreover, w'_{meso} is a mesoscale property related to a NWP grid scale ℓ and possibly plume segment length, but different from the plume cross-section scales. Hence, a separate turbulence model is needed for this. We estimate

$$w'^2_{\text{meso}} = w'^2_{\text{SGS}} + \bar{w}^2 \tag{56}$$

from the variance w'^2_{SGS} of vertical SGS turbulence and of vertical motions $\bar{w}$ (possibly gravity wave driven) at NWP scales. The computations show that the latter contribute the larger part in most cases. The method to analyse SGS velocity variance follows Schumann (1991), his Eqs. (10, 12, 14). Details are given in Appendix A9. These velocity fluctuations w'_{meso} are mostly small, of the order 1–10 cm s^{-1}. We further assume that the time scale for reducing the number of ice particles by wave induced vertical fluctuations is of order N_{BV}^{-1}. With these relations we set

$$(dN/dt)_{\text{meso}} = -E_{\text{meso}} N_{\text{BV}} w'_{\text{meso}} (dT/dz)/\Delta T_c, \tag{57}$$

Presently we use this model with $E_{\text{meso}} = 2$, but further studies are needed to optimise this selection.

For keeping $N \geq 0$ during numerical integration of N in time, even for strong loss processes, instead of using the standard Runge-Kutta scheme, we use an analytical integral (see Appendix A10), which provides the exact solution for constant coefficients and positive approximate solutions otherwise.

$$N(t + \Delta t) = \frac{N(t)\beta \exp(-\beta \Delta t)}{\beta + \alpha y_0 [1 - \exp(-\beta \Delta t)]} \frac{L(t)}{L(t + \Delta t)}. \tag{58}$$

(The length scale ratio corrects for the change in segment length during the time step.) The coefficients α and β

$$\alpha = -\frac{\Delta t}{N^2}(\partial N/\partial t)_{\text{agg}}, \beta = -\frac{\Delta t}{N}(\partial N/\partial t)_{\text{turb}}, \tag{59}$$

are computed as average of the values at times t and $t + \Delta t$.

Figure 9 shows that the contrail ages get considerably reduced with these particle loss parameterizations. The contrail ages are now below the ISSR ages. The mean, med, max ages for this June-case are 2.9 h, 2.0 h, 24 h. These ages are consistent with the observations cited. From parameter studies, we find that all three loss models are important for the mean statistics.

The computed particle concentrations are consistent with observations: The lower panel in Fig. 7 shows that the total ice crystal number N in the ensemble of contrails ranges from 1 to $50 \times 10^{11}\,\text{m}^{-1}$, slowly decreasing with plume age. For comparison, Spinhirne et al. (1998) deduced values of 1 to $3 \times 10^{11}\,\text{m}^{-1}$ slightly decreasing with plume age from remote sensing of two contrails with estimated ages in the order of one or a few hours. The computations show ice particle concentrations n decreasing more strongly than N because of dilution from about 0.1 to $0.001\,\text{cm}^{-3}$ for one hour aged contrails, which is roughly consistent with extensive in-situ observations in cirrus (Krämer et al., 2009). For aged contrails, one expects ice particle concentrations similar to ambient cirrus (Gayet et al., 1996; Spinhirne et al., 1998; Schröder et al., 2000; Schumann et al., 2011b).

The lower panel of Fig. 8 shows the relationship between particle sizes and fall speeds. The fall speeds depend on Reynolds number and, hence, the scatter or data reflects variations of viscosity with pressure and temperature. The range of computed sedimentation speeds is consistent with the few observations: Duda et al. (2004) found best agreement with observations for computed contrail positions, depending on wind shear and altitude, for fall speeds between 0 and $0.045\,\text{m s}^{-1}$. Konrad and Howard (1974) deduced fall speeds up to $1.4\,\text{m s}^{-1}$ from radar observations in contrail fall-streaks.

2.13 Contrail optical depth for solar radiation

The optical depth for solar radiation is the vertical integral of the local extinction $\beta(\mathbf{x})$ over the cloud height (Hansen and Travis, 1974). The mean optical depth τ of the contrail is defined in the Gaussian plume model, such that

$$B\tau = \beta \iint \exp[-\frac{1}{2}\mathbf{x}^T \sigma^{-1} \mathbf{x}]dz\,dy = \beta A \tag{60}$$

is the product of width and optical depth effective for radiation. Here, β is the extinction in the plume center. Hence, by definition, $\tau = \beta D_{\text{eff}}$, with effective plume depth

$$D_{\text{eff}} = A/B. \tag{61}$$

The extinction $\beta = Q_{\text{ext}}\bar{A}_p$ is a function of the extinction coefficient Q_{ext} (assumed constant) and the sum of the projected areas $\bar{A}_p$ of all ice particles weighted with the size distribution $n_p(r)$. By definition (Hansen and Travis, 1974), the effective radius r_{eff} relates $\bar{A}_p$ to $\bar{V}_p$, the corresponding volume of all particles:

$$r_{\text{eff}} = \frac{3\bar{V}_p}{4\bar{A}_p} = \frac{3\int V_p(r)n_p(r)dr}{4\int A_p(r)n_p(r)dr} \tag{62}$$

Hence, $\beta = 3Q_{\text{ext}}\bar{V}_p/(4r_{\text{eff}})$. The particle volume can be expressed as a function of the ice mass mixing ratio I, air density ρ, and ice bulk density ρ_{ice} as $\bar{V}_p = \rho I/\rho_{\text{ice}}$. With ice water path

$$\text{IWP} = \rho I D_{\text{eff}} \tag{63}$$

we finally obtain

$$\tau = 3Q_{\text{ext}}\text{IWP}/(4\rho_{\text{ice}}r_{\text{eff}}). \tag{64}$$

The product $B\tau$ is relevant for radiative forcing calculations. The local value of $\tau(y)$ for given y is needed, e.g., for analysis of contrail cover for given optical depth. As derived in Appendix A11, the local $\tau(y) = f_\tau\tau$ is a factor

$$f_\tau = (4/\pi)^{1/2}\exp[-(1/2)y^2/\sigma_{yy}] \tag{65}$$

larger than the bulk value τ; $f_\tau(0) = 1.13$.

The effective radius r_{eff} depends on the particle shape (habit) and the size distribution $n_p(r)$ of the ice particles. An extensive study (Schumann et al., 2011b) showed that the effective radius can be estimated from the volume mean radius r, Eq. (49), using a coefficient

$$r_{\text{eff}} = r/C_r, \tag{66}$$

with $C_r = 0.9 \pm 0.3$, though with considerable uncertainty.

The solar radiation extinction efficiency is approximated by Mie-theory as

$$Q_{\text{ext}} = 2 - (4/\rho_\lambda)(\sin(\rho_\lambda) - (1-\cos(\rho_\lambda))/\rho_\lambda. \tag{67}$$

with $\rho_\lambda = 4\pi r_{\text{eff}}(\kappa-1)/\lambda$, where $\kappa = 1.31$ is the real refractive index of ice and $\lambda = 0.55$ nm the wavelength of visible light (van de Hulst, 1957).

The integration ends when τ gets small ($< 10^{-4}$), or when the number concentration n of ice particles gets small ($< 1\,\text{L}^{-1}$) or when the contrail center of gravity falls below the lower boundary of the computational domain (typically $p > 600$ hPa).

Figure 10 shows that the optical depth varies between 0.001 and 0.5 in most cases, with larger values for young contrails. This is fully consistent with observations and other models (Kärcher et al., 2009a; Atlas and Wang, 2010; Voigt et al., 2011). However, with respect to climate impact, it is the product of τ with the contrail width B which counts. This value generally increases and takes a maximum after about a few hours in this model, consistent with observations (Atlas and Wang, 2010). Only a few of the older contrails reach larger values. It implies that the largest climate impact comes from contrails of a few hours age.

Contrail cirrus model

U. Schumann

2.14 Radiative forcing

We use an efficient parameterization for approximate computation of the longwave (LW) and shortwave (SW) radiative forcing (RF) by contrails. The model, with details as described elsewhere (Schumann et al., 2009, 2012), computes the flux changes at top of the atmosphere (TOA) induced by additional contrails as a function of the solar optical depth τ, effective radius r_{eff}, and temperature T of the contrail, and optical depth τ_c of cirrus above the contrail. It uses NWP input for outgoing longwave radiation (OLR), reflected solar radiation (RSR), and solar direct radiation (SDR) (Blanco-Muriel et al., 2001) without contrails. Moreover S_0 varies a few percent around the solar constant of 1365.42 W m^{-2} with the day of the year (Blanco-Muriel et al., 2001; Paltridge and Platt, 1976). From these input values, the model (in module RADI) computes the LW and SW RF per contrail area,

$$\text{RF}_{\text{LW}} = [\text{OLR} - k_T(T - T_0)][1 - \exp(-\delta_\tau F_{\text{LW}}(r_{\text{eff}}))\tau]$$
$$\times E_{\text{LW}}(\tau_c) \qquad \geq 0, \qquad (68)$$

with 5 fit parameters per crystal habit: T_0, k_T, δ_τ and 2 further parameters in $F_{\text{LW}}(r_{\text{eff}})E_{\text{LW}}(\tau_c, T)$;

$$\text{RF}_{\text{SW}} = -\mu S_0(t_A - A_{\text{eff}})^2 A_c(\mu, \tau)$$
$$\times F_{\text{SW}}(r_{\text{eff}})E_{\text{SW}}(\mu, \tau_c) \leq 0, \qquad (69)$$

with effective albedo $A_{\text{eff}} = \text{RSR}/\text{SDR}$, cosine of solar zenith angle $\mu = \cos(\theta) = \text{SDR}/S_0$, and 10 fit parameters. RF$_{\text{LW}}$ is constrained to positive values, so that contrails at low altitudes with high ambient temperatures have zero contribution. Likewise, RF$_{\text{SW}}$, is constrained to negative values. The model prescribes the contrail habit mixture as a function of radius r (Schumann et al., 2011b). The parameterization has been calibrated for an extensive set of atmospheres/surfaces against libRadtran forward calculations (Mayer and Kylling, 2005). The approximate results and the libRadtran results correlate better than 98 %. The RF parameterization is consistent with previous results

(Meerkötter et al., 1999). Preliminary RF results have been presented in Schumann et al. (2011a).

2.15 Contrail cirrus cover

The ensemble of contrails together with the natural (non-aviation) NWP-cirrus is con-
5 sidered as the "total cirrus" in this model. The additional cirrus induced by contrails is interpreted as "contrail cirrus". Contrail cirrus differs from young isolated contrails in shape. Single contrails widen by turbulent diffusion and shear, get distorted by variable winds, and disrupted by contrail free segments, but still remain identifiable as a near-linear sequence of contrail segments in clear air. Single contrails change their shape
10 when overlapping with natural cirrus. A cluster of contrails with different histories over-lap irregularly so that the line-shaped structure gets lost. CoCiP in this version does not account for physical interactions between contrails among each other nor with cirrus. However, CoCiP does simulate irregularly structured contrail cirrus.

We define the regional cover C of a cirrus as that fractional horizontal area in which
15 the solar optical depth τ of the cirrus is larger than a critical value τ_c. This seems plausible, because only cirrus with a minimum optical depth is visible. Moreover, the optical depth controls its radiative forcing and hence its climate impact. Details of detectability depend on underground properties, ambient atmosphere, illumination, etc. The threshold is observer and instrument dependent. Hence, cloud cover may be ill-
20 defined. Here, we orient ourselves on satellite observations, where a value of $\tau_c \approx 0.1$ may be realistic.

Overlapping contrails are treated according to their known position and optical depth. The coverage of overlapping contrails is far smaller than the summed coverage of individual contrails. In regions with many overlapping contrails the contrail cirrus cover
25 increases less than linear with air traffic and saturates at a maximum value (which may be 100 %). The cover gets even smaller when contrails overlap with natural cirrus. Hence, it is important to have a clear definition of cover C. Here we define the cover of contrail-cirrus (CO) as the cover of total cirrus (COCI) minus the cover of natural cirrus

(CI),

$$C_{CO} = C_{COCI} - C_{CI}, \tag{70}$$

based on their solar optical depth values, respectively, above a critical value,

$$\tau_{COCI} > \tau_c \text{ and } \tau_{CI} > \tau_c. \tag{71}$$

5 More complex criteria, e.g., the contrast in brightness temperature and reflectance of contrails and cirrus, computed similar to RF, Sect. 2.14, might be included in future versions.

Here, the cover is computed pixel-wise based on optical depth. The NWP grid is far too coarse to resolve the contributions from the relatively narrow contrails. Instead,
10 we use a fine-resolution matrix of optical depth values ("cloud mask") $\tau_{i,j}$ in grid cells (pixels) with far higher resolution and independent of the NWP. For global analysis, the grid center points are located at $x_i = i\Delta x$, $y_j = j\Delta y$, $i = 0,1,...,N_{xT}$, $j = 0,1,...,N_{yT}$, with grid spacing $\Delta x = 360/(N_{xT} - 1)$, $\Delta y = 180/(N_{yT} - 1)$. We use $N_{xT} = 5001$, $N_{yT} = 3601$ in our global reference cases. The pixel area size is $\Delta x \times \Delta y$. In this implementation its
15 value is $5.7 \times 5.6\,\mathrm{km}^2$ at 45° latitude. Even this fine grid cannot resolve the very narrow young contrails, but these contribute little to the total cover. The resolution error because of finite grid depends on the ratio of contrail width relative to grid resolution and on the threshold ratio τ_c/τ. It decreases with increasing contrail width and decreasing threshold. The error gets small in particular for many randomly distributed and over-
20 lapping contrails. For example, for a region over the North Atlantic, for $\tau_c = 0.1$, mean width $B = 7\,\mathrm{km}$ and mean optical depth $\tau = 0.12$, the contrail cover changes by 5% if the grid scale is reduced by a factor of ten. This appears to be acceptable.

The contrail contributions to $\tau_{i,j}$ are computed within a module TAU2DS within the loop over all flights. The NWP-cirrus contributions are added in module TAU2DX at the
25 end. As explained in Appendix A12 and Fig. 24, a segment contributes to $\tau_{i,j}$ when the normal from x_i, y_j onto the segment (W_n, W_{n+1}) crosses the segment at a cross-point x_s, y_s between its endpoints. The amount $\tau f_\tau(s)$, see Eq. (65), of contribution depends

on the distance s between x_s, y_s and x_i, y_j. In order to add all τ-contributions from all contrail segments, one has to test the distance to all points (i, j) in the cloud mask. This time-consuming test can be reduced to pixels in a certain distance from the segment end-points, depending on the maximum product $B\tau$ of the contrail segments. By this strategy, the computing time increases about linearly with the total number of contrail segments from all flights.

For analysis of contributions of natural cirrus to $\tau_{i,j}$ in the upper troposphere and lower stratosphere (between $z_{min} = 6.0$ km and $z_{max} = 16.1$ km), we first compute the solar optical depth $\tau_C = \int_{z_{min}}^{z_{max}} \beta_C \, dz$ of this cirrus for given cirrus-extinction $\beta_C = 3Q_{Cext}\text{IWC}_C/(4\rho_{ice}r_{effC})$, and extinction efficiency $Q_{Cext} = 2$. The effective radius is determined from the NWP data as a function of temperature and ice water content IWC_C of the NWP-cirrus. When using ECMWF data, we compute r_{effC} consistently (Sun, 2001; Sun and Rikus, 1999).

Moreover we account for the three-dimensional distribution of cirrus cover $C_C(x,y,z,t)$ inside a cirrus, which is provided as input for each NWP grid cell: From $C_C(x,y,z,t)$ we first compute a two-dimensional cirrus cover effective for observers from above, $Ci_C(x,y,t) = \max_z[C_C(x,y,z,t)]$. Since the cloud mask has a far higher resolution than the NWP-grid, we distribute the broken cirrus coverage in the cloud mask randomly. For this purpose we distribute the cirrus optical depth τ_C in at least partially covered grid cells onto pixels, keeping its grid mean value constant at τ_C. For each grid cell i, j with $Ci_C > 0$, a random number R, uniformly distributed between 0 and 1, decides, if $R > 1 - Ci_C$ then $\tau_c = \tau_C/Ci_C$, else $\tau_c = 0$. The value τ_c is added to $\tau_{i,j}$ as cirrus contribution. The randomly distributed cloud cover is evident in Figs. 11–12.

For example, the top panel of Fig. 11 shows the optical depth of contrails (τ_{CO}), for all the contrails identified by red lines in Fig. 6, while the lower panel shows the optical depth of contrails and cirrus together (τ_{COCI}). Figure 11 (upper panel) exhibits again clusters of contrails over North America, the North Atlantic and mid Europe. Some contrails plotted in Fig. 6 (e.g. near 90° latitude in the Southern Indian Ocean) are invisible in Fig. 11, because of low optical depth. When plotted together with the

Contrail cirrus model

U. Schumann

optical depth of natural cirrus (lower panel) only few contrails (e.g. over North America) remain visible.

Figure 12 shows the computed cover for a contrail outbreak over parts of North America. The upper part shows the cover C_{CO} of contrails ($\tau_{CO} > 0.1$) alone, while the lower panel shows the cover of total cirrus C_{COCl} as composed of natural cirrus ($\tau_{Cl} > 0.1$, blue pixels) and contrail-cirrus ($\tau_{Cl} < 0.1$ and $\tau_{COCl} > 0.1$, red pixels). Contrails inside (or above/below) thick cirrus do not contribute to contrail-cirrus cover. In fact, a large fraction of contrail pixels (about 2/3 globally) become invisible inside natural cirrus. However, even thin contrails may push the optical depth of thin cirrus above the critical value. The contrail outbreak happens to occur in this simulation over North America (at 10 pm local time). Some contrails are still identifiable as line-shaped structures. However, the line-shape gets lost in contrail clusters, which mostly occur in the neighborhood of natural cirrus. Still part of the contrail pixels remain visible in the total cirrus results while others submerge in natural cirrus. Some of the additional contrail cirrus pixels are closing cloud gaps in the natural cirrus cover. Regionally, over about 100 to 600 km scales in this example, the contrails cause 100 % cirrus cover.

From this cloud mask we finally compute global or regional cloud covers by summing the areas of pixel cells with $C_{COCl} = 1$ and $C_{Cl} = 0$, and dividing by the respective global or regional total horizontal area. Here we show the results for a single time slice. The results depend nonlinearly on the threshold value τ_c. For $\tau_c = 0.1$ and 0.05, in this example, the global contrail coverage is 0.23 % and 0.36 %, respectively (NWP cirrus cover: 19 % and 27 %), respectively. Hence, the value of τ_c has to be carefully selected for meaningful comparisons to observations. This will be one of the many topics that can be studied with CoCiP in the future.

3 Results

3.1 Example simulation of contrails

As discussed before, see Figs. 6, and 11 to 12, CoCiP has been applied for a global case study using NWP data from ECMWF and traffic data from FAA-EUROCONTROL. The global simulation identifies 31 575 flights in the time period 03:00–06:00 UTC for a day in June 2006, forming at least short contrails. The computation time is 3.5 min (including a large fraction for I/O time). Hence, for each contrail less than 0.01 s is needed. For a snapshot at 06:00 UTC that day, a total of 3402 contrails are found. This clearly demonstrates the size of the problem and the efficiency of the method. Still, to simulate a full year with an order 30 million flights globally, requires about 7 h of computing time and lot of memory for the data.

Figures 7 to 10 show the contrail properties for a random subset of contrail segments over the North Atlantic. As discussed above, the resultant contrail dimensions and ice properties exhibit magnitudes and trends with age at least roughly consistent with observations. The simulations were performed with model parameters as explained. The most important parameters and their values are set as listed in Table 2. For quantitative assessment, we next consider case studies for single contrails.

3.2 Dilution

The dilution ratio of passive tracers emitted form aircraft was discussed before. It determines the mass specific concentration above background for given emission index EI as $\Delta c = \mathrm{EI}/N_{\mathrm{dil}}$. The empirical function, Eq. (18), was derived from measurements for plume ages t up to 5000 s, with about factor three uncertainty (Schumann et al., 1998). The rather large spread of the data relative to this approximation has to be expected because aircraft details and atmospheric shear and stratification are not taken into account.

CoCiP is applied to compute the dilution of a passive tracer for a flight in a uniform model atmosphere, and for a range of values of shear S and Brunt-Vaisaila frequency

N_{BV}, and for three typical commercial aircraft of different sizes, similar to B747, A310, and B737, see Table 3.

Figure 13 shows that the dilution depends on aircraft properties and, in particular, on ambient shear and ambient stratification. As to be expected, the dilution is quicker for larger aircraft, stronger shear, and weaker stratification. Overall, the order of magnitude agrees with Eq. (18). In fact, CoCiP provides a generalization of this function for given parameters. This agreement is sensitive to various model parameters listed in Table 2. Smaller initial downwash (C_{z1}), vertical diffusivity (w'_N), and shear Δz_{eff} reduce dilution. On the other hand these parameters also control the contrail depth, and larger parameter values may bring our depth results closer to observed values (Freudenthaler et al., 1995).

Figure 13 also shows the dilution for integration with two different time steps of either $\Delta t = 60$ or 3600 s. The model results are only weakly sensitive to such drastic time step changes. Thus, CoCiP can be applied with rather large time steps. This is essential for computational efficiency in global applications.

3.3 Aged contrail in comparison with other model results

CoCiP is designed to simulate contrails with large ages. Comparisons with in-situ measurements for short and mid time-scales will be reported in Sect. 3.4. Here we describe model results for an artificial case, discuss their plausibility, and compare with results from a more complex fluid and microphysics 2d model (Unterstrasser, 2008; Unterstrasser and Gierens, 2010a) for nearly the same case.

We consider a long-lived contrail, up to 10 h age, in a static, clear, and uniformly ice-supersaturated atmosphere without vertical motions. Note that the real atmosphere will never be uniform for such a long time period. Both models use the same parameters except that the uniformly supersaturated layer in the 2d model is only 1 km thick, with decreasing humidity above and below (Unterstrasser and Gierens, 2010b). The simulations are performed for a "B747" as listed in Table 3, at $p = 250$ hPa, $T = 217$ K,

$N_{BV} = 0.01\,\text{s}^{-1}$, $S = 0.002\,\text{s}^{-1}$, and RHi = 1.2. We vary EI_{soot} by a factor of 3 to study the impact of wake-induced particle losses. In addition we vary D_V to explain differences between CoCiP and the 2d model, see Figs. 14 and 15.

CoCiP is run in this case with time steps of 150 s (5 s in the 2d model). Small wiggles in the CoCiP τ values are caused by Mie oscillations, Eq. (67). Wiggles at late times are caused by accumulation of approximation errors in the late exponential particle growth phase. Note that the model contains no smoothing which could damp oscillations along waypoint tracks. These wiggles are avoided when using smaller time steps.

Qualitatively, the results from the two models are similar in magnitude and trends, but some differences are notable. The CoCiP contrail width (Fig. 14 left upper panel), initially increases about linearly with time because shear dominates the lateral spread at early times. Note that the width B as defined by the Gaussian plume model is plotted. Smaller plume concentrations spread further away from the contrail center line. In the 2d model, the width of the contrail is defined as that part with optical depth larger than given threshold values, as identified in the figure legend (0.01, 0.02, 0.05, and 0.1). Our reference case agrees best with the 2d results for an optical depth in between 0.01 and 0.05. In principle, a similar analysis would be possible with the CoCiP results. But more important is the product of optical depth with contrail width (or its integral over the lateral coordinate), see Eq. (60), which controls cover and radiative forcing. The right panels of Fig. 14 show τ and this integral value or product τB. We see that the two models agree for these important parameters to the order of magnitude. Best agreement is achieved at early times for enhanced vertical diffusivity. Later the width grows stronger than linear in CoCiP because of increasing depth making shear dispersion more efficient. The thicker depth at later times is mainly caused by sedimentation. For reduced particle emissions, sedimentation becomes important earlier, as expected, so that the width grows more quickly. The thickness also increases for enhanced vertical diffusivity.

The dilution at one hour age (not shown) is about a factor 4 larger for enhanced vertical diffusivity. Sedimentation effects on dilution are still small (10 to 20 %) at this age. For lower diffusivity, the dilution is slightly (30 %) below, for higher diffusivity it is

Full Screen / Esc

Printer-friendly Version

Interactive Discussion

3 times above the empirical function Eq. (18). Hence, both versions and both models are roughly compatible with measured dilution.

The number of ice particles per flight distance N (left lower panel of Fig. 14), remains fairly constant for the first few hours in both models, after the wake vortex period. Later, N decreases more quickly in CoCiP. Figure 16 shows that aggregation, Eq. (54), has by far the strongest impact on particle losses in this model. However, the other processes also contribute to these losses.

We note that CoCiP agrees far better with the 2d model for reduced particle emissions. This is unexpected, because of the rather low ambient temperature and high humidity. The contrail is formed at conditions far above the SAC threshold ($RHi_{LC} = 3.3$, $T_{LC} = 8.3\,K$). Therefore, in spite of the size of the aircraft, CoCiP computes large survival fractions of ice particles ($f_{surv} = 0.91$), see Fig. 5. An enhanced vertical diffusivity has a minor impact on N. The slow decrease in the first hours is caused by the turbulent decay process simulated according to Eq. (51). Later the loss by aggregation dominates by far.

The optical depth values of the two models differ most strongly. The CoCiP optical depth comes closer to the 2d model result for enhanced vertical diffusivity. Later the optical depth increases in CoCiP because the contrail particles start to sediment. Hence the contrail gets thicker, and collects more humidity from the ambient air, giving larger ice mass, with larger particles and hence larger optical thickness values. In contrast, the 2d model predicts a decrease in optical depth after 3 h age. One possible reason for this difference is the limited depth of the supersaturated layer in this example with ice sedimenting out of the layer in the 2d model, while CoCiP follows the plume in Lagrangian manner without loss of ice mass. A second reason may result from the assumed ice saturation in CoCiP. At late times, the humidity may exceed ice saturation causing less ice water content.

Figure 15 shows further results to explain the contrail dynamics. The left lower panel of this figure shows the small initial downward displacement of the contrail center simulated for the wake vortex phase. Later this displacement grows and exceeds 1 km

because of sedimentation. The near constant number N of particles share in the growing amount of ice mass from entrained humidity in supersaturated air. Hence, the particles grow in size, see top left panel. Eventually the particles become large and start sedimenting quickly. In reality the largest particles would sediment first while the smaller ones stay longer at the initial altitude (Jensen et al., 1998a). This separation of particles cannot be simulated with the plume-bulk model. Instead, CoCiP simulates this process by letting the center of gravity of the contrail sink with time (see left lower panel), similar to what has been deduced from observations (Atlas et al., 2006). At the same time, the contrail depth increases by enhanced vertical diffusivity, see Eq. (37). At contrail ages of 8.7 and 6.7 h, for the high and low emission cases, respectively, the particle sizes exceed 100 µm in radius, the fall speed exceeds $0.7\,\mathrm{m\,s^{-1}}$ (see lower panel of Fig. 8). Hence, the contrail falls quickly and precipitates at lower altitudes. We note that a reduction of the initial particle number and an increase of vertical diffusivity have similar effects on sedimentation (see mean radius and vertical displacement in the left panels of Fig. 15).

In a rough approximation, the model simulates the effects of fallstreaks which have been observed to form below contrails at high ambient humidity (Schumann, 1994; Heymsfield et al., 1998; Atlas et al., 2006). This process effectively limits the contrail life cycle at high ambient humidity. Contrails would live longer for lower ambient humidity because of less sedimentation and aggregation. For this reason the contrail climate impact does not increase linearly with humidity. The example results show also the importance of soot emissions. Reduced soot emissions reduce the number of ice particles but increase their sizes. As a consequence, both the optical depth and the life time of the contrail get reduced. Both effects reduce the climate impact of contrails.

Although we can explain most of the differences, some differences remain. It is tempting to take the 2d model as benchmark. However, dynamics and microphysics in the 2d model also have uncertainties. Obviously, correct representation of turbulent mixing is as important as that of cloud physics. Therefore, in the absence of detailed measurements it is hard to decide which model is closer to the truth.

3.4 Young and mid-aged contrails in comparison with in-situ observations

CoCiP is applied to compute the ice bulk properties of contrails for comparison with in-situ measurements for various contrail ages (5–2000 s) behind various aircraft as reported by Schröder et al. (2000), Febvre et al. (2009) and for the CONCERT campaign (Voigt et al., 2010). (We do not expect good agreement for CoCiP for the youngest contrails.) For plume ages larger 150 s, some of the data have been used before to test the 2d model of Unterstrasser and Gierens (2010a). Also CoCiP has been tested before by comparison to data for six contrails measured during one measurement flight in CONCERT; here we compare in more detail to the data for a CRJ2 aircraft from that campaign (Voigt et al., 2010).

The observational data are compiled in Table 4. We replace the reported ice particle concentration n_m by $n_{ice} = \mathrm{IWC}/((\pi/6)\rho_{ice}d_{mean}^3)$, i.e. the value consistent with the reported ice water content IWC and volume mean diameter d_{mean}; both values, partly with large differences, are listed in Table 4. The measured concentrations are uncertain due to variable lower cut-off size of ice particles in the data analysis (Febvre et al., 2009). Some aircraft types and humidity values were unknown and had to be estimated.

Measurements of relative humidity at low ambient temperatures are prone to large uncertainties. The ambient humidity may be estimated from the measured ice water content assuming that the ice water content stems from condensing ambient supersaturation and from the emitted water. Hence, we invert Eq. (19), and use the dilution function, Eq. (18) to obtain

$$\mathrm{RHi}_i = 1 + \left[\frac{\mathrm{IWC}}{\rho} - \frac{\mathrm{EI}_{H_2O}}{7000(t_{age}/t_s)^{0.8}}\right]\frac{R_1 p}{R_0 \rho_{ice}(T)}. \tag{72}$$

Table 5 compares the measured relative ice humidity values RHi_m with the computed values RHi_0 (for zero engine emissions) and RHi_i. We see that the computed values generally are close to the measured ones. The values RHi_0 and RHi_i differ considerably

for young plumes. This highlights the importance of the water emitted by the aircraft engines in addition to water from ambient supersaturation for young contrails. The measured IWC for the youngest plume cannot be explained this way. The computation for the small age would imply negative ambient humidity. The maximum analyzed

5　humidity values are in a reasonable range, above saturation but below homogeneous nucleation thresholds (Koop et al., 2000), as expected for persistent contrails.

We apply CoCiP for static atmospheres (without subsidence and other changes with time), mostly under ice supersaturated conditions in clear air. During these conditions and ages the ice loss terms of CoCiP, Eq. (50), though included in these computations,

10　are small. Table 5 lists the model parameters as used for these simulations.

The results are most sensitive to ambient humidity RHi and to dispersion (as a function of ambient shear S), as to be expected. CoCiP is run with RHi= 0.9 for those cases where the table indicates smaller RHi$_i$ values. Unfortunately, also ambient shear, as listed in Table 5, and stratification had to be estimated. In most cases, shear was not

15　reported. Even when the velocity profile was measured (Febvre et al., 2009), where shear was quite large, the effective shear value is difficult to derive because of large variability. Hence, we apply the model with a set of S-values, 0, 0.001 and 0.002 s^{-1}.

The results are shown in Fig. 17. The CoCiP results for low and high shear values embrace most of the observed data points. The IWC results for this input are close to

20　the observed values as they should because of adjusted humidity values. The agreement is not perfect, because the dilution in CoCiP depends on the unknown shear, and differs from the empirical dilution function, as expected. With this input, CoCiP reproduces the data as observed in most cases, see Fig. 17. For example, the model comes closest to the observations of Febvre et al. (2009) (ages 150 and 900 s) for the largest

25　S-value. An exception is case A of Schröder et al. (2000), with smallest (5 s) plume age, for which the measured IWC is far less than computed. This may be caused by incomplete condensation in the young plume.

Because of the uncertainty in ice particle nucleation and in the fraction of ice particles surviving the wake vortex phase, we run CoCiP with reduced and increased initial

particle emissions. For this purpose, we simply multiply the soot emission index with factors 0.5 or 2. We found that the agreement gets worse when simulating a smaller survival ratio by reducing the particle emissions. The agreement gets also worse for enhanced particle emissions, which should provide better results if ice particle formation,

5 e.g. from volatiles, is important. This result is in part a consequence of the selected shear values. Nevertheless, the test shows that the data are consistent with the model for the selected parameter values.

Finally, we test again the sensitivity to the vertical diffusivity. We changed D_V by factors 0.5 and 10 compared to the reference case. For plume ages below 3 min, the

10 impact of D_V is minor, as expected. For larger plume ages, e.g. case U, an increase in D_V by a factor of 10 causes more dilution and considerably (factor 7) smaller particle concentrations, therefore. The ice water content increases slightly (by 5 %) and the particles become a factor of 2 larger in diameters. However, the agreement with observations deteriorates when D_V gets increased compared to the reference case. Hence,

15 the diffusivity parameterization should stay unchanged.

It appears that the bulk microphysics model used in CoCiP is sufficient to explain the contrail properties consistent with the observations. The agreement between results and observations is at least as well for CoCiP as it is for the 2d model (Unterstrasser and Gierens, 2010a). To some extent this implies that the set of measurements are not

20 complete (e.g., for shear) or accurate enough (e.g., for humidity) to provide rigorous constrains. However, the comparison shows that the model gives a fair representation of the fraction of particles surviving the early wake vortex. There is no hint for important ice nucleation from volatiles in these cases.

4 Conclusions

25 The contrail physics model implemented in the "Contrail Cirrus Prediction Tool" (CoCiP) has been described in detail. The model has been applied successfully for a global case and for individual contrails in comparison with other model results and in-situ measurements.

Contrail cirrus model

U. Schumann

Back | Close

Full Screen / Esc

The Lagrangian Gaussian contrail model treats the life cycle of contrails with bulk contrail ice physics. The model is efficient in treating mixing and cloud processes quasi analytically. The numerical scheme is unconditionally stable and guarantees positive definite solutions. The simulation of an individual contrail along a flight track

5 with hundreds of waypoints with maximum life time of order a day requires far less than a second computing time on a laptop. This makes contrail simulations for a large fleet of aircraft feasible. In the present version, the contrails are simulated without feedback among each other or with the background meteorology. This may be overcome when coupling the model with a climate model.

10 The model accounts for the influence of aircraft properties and ambient meteorology. The model accounts for standard contrail formation thresholds, for advection, and turbulent mixing, and for ice mass formation from emitted and ambient humidity, with ice crystal number depending on the number of soot particles emitted. The model includes simple approximations for ice particle survival in the adiabatically sinking wake

15 vortices, and particle losses in aged contrails. These model parts may need to be further improved when comparing to further observations. Moreover we note the strong sensitivity to turbulent diffusivities. This calls for further refinement of the parameters for this purpose, e.g., kinetic energy and dissipation rates from NWP input data.

CoCiP provides a generalization of an often used simple dilution function derived

20 previously from measurements (Schumann et al., 1998). The dilution of passive tracers from aircraft engines depends on aircraft properties and more strongly on shear and stratification in the ambient atmosphere.

The model reproduces measured contrail properties for given aircraft type in terms of ice water content, crystal number concentration, and mean crystal diameters, in

25 contrails of about 100 to 2000 s age. Comparable measurements in isolated single contrails at larger ages are missing.

The CoCiP model constrains the ambient relative humidity at the time of contrail formation, which is difficult to measure. It also is used to estimate the ambient wind shear controlling contrail dispersion. The comparison supports the assumption that

the number of ice particles in the contrail at several minutes plume age is mainly determined by the number of soot particles emitted from the aircraft engines. Turbulence and cloud physics are equally important for explaining observed contrail dynamics.

Particle loss processes, in particular sedimentation in ice supersaturated air masses, control the contrail life time. Such contrails end with fallstreaks. Contrails persist shorter for smaller soot particle emissions. Aged contrails contribute most to climate change because of largest product of optical depth and width. More data are needed to constrain the maximum ages of contrails and their final dissipation processes.

We have shown an example with contail-cirrus outbreaks. The line-shape of young contrails gets lost in this model by overlap with other contrails and cirrus. The global-mean contrail-cirrus cover is small, but reaches 100 % regionally at scales of a few 100 km, depending nonlinearly on traffic density and threshold values for cloud detectability.

Appendix A   Model Details

A1   Gaussian area integral

The area integral, Eq. (3), can be evaluated using a principal axis transformation
$$\mathbf{x}^T \sigma^{-1} \mathbf{x} = \mathbf{z}^T \mathbf{X}^{-1} \mathbf{\Lambda X z}.$$
With eigenvalues $\mathbf{\Lambda}$, defined by
$$\sigma^{-1} \mathbf{X} = \mathbf{\Lambda X}, \quad \mathbf{\Lambda} = \mathbf{diag}(\lambda_1, \lambda_2),$$
and substitution $\mathbf{y} = \mathbf{Xz}$,
we have
$$A = \int\int \exp[-(1/2)\mathbf{y}^T \mathbf{\Lambda y}]d\mathbf{y}.$$
With,
$$\mathbf{y}^T \mathbf{\Lambda y} = y_1 \lambda_1 y_1 + y_2 \lambda_2 y_2,$$
we obtain
$$A = \int\int \exp[-(1/2)(y_1 \lambda_1 y_1 + y_2 \lambda_2 y_2)]dy_1 dy_2$$

Contrail cirrus model

U. Schumann

⏮ | ⏭

◀ | ▶

Back | Close

Full Screen / Esc

Printer-friendly Version

Interactive Discussion

$$= [\int \exp[-(1/2)\lambda_1 y_1^2] dy_1][\int \exp[-(1/2)\lambda_2 y_2^2] dy_2].$$

With (Abramowitz and Stegun, 1964)

$$\int_{-\infty}^{\infty} \exp[-(1/2)\lambda y^2] dy = (2\pi/\lambda)^{1/2},$$

and

5 $\lambda_1 \lambda_2 = \det(\sigma^{-1}) = 1/\det(\sigma),$

we obtain the result as given in Eq. (3),

$$A = 2\pi[\det(\sigma)]^{1/2}.$$

In many applications of the Konopka model, the first factor two in Eq. (3) was missing.

A2 Interpolation aspects

10 Interpolation is performed, e.g., for a function $F_{i,j}$ at discrete grid-points (i,j) in a Cartesian x–y–plane, with equidistant grid spacings Δx and Δy, and mid-cell coordinates x_i, y_j, using bilinear interpolation:

$$F(x,y) = \tfrac{1}{4}(g_1 F_{i,j} + g_2 F_{i+1,j} + g_3 F_{i+1,j+1} + g_4 F_{i,j+1}),$$

where $g_1 = (1-\gamma)(1-\eta)$, $g_2 = (1+\gamma)(1-\eta)$, $g_3 = (1+\gamma)(1+\eta)$, $g_4 = (1-\gamma)(1+\eta)$, with
15 $\gamma = (x - x_i)2/\Delta x$, $\eta = (y - y_j)2/\Delta y$.

Relative (RHi) and absolute (q) humidity, for given temperature T and pressure p, are nonlinearly related by saturation pressure $p_{ice}(T)$ and $q = \mathrm{RHi}(p_{ice}(T)/p)R_0/R_1$. Interpolation of humidity may be performed in NWP input in either variable. Both variants introduce up to 7.2 % errors (either in RHi or in q) for 50 hPa pressure intervals,
20 see Fig. 18. CoCiP has been coded in both variants, and the differences have been found to be important because of strong sensitivity to relative humidity in the SAC and to absolute humidity in the ice water content and optical depth. The results in this paper were computed with interpolation in q, partly (Sects. 3.2 to 3.4) with fine vertical resolution.

A3 Saturation pressure

Saturation pressure over liquid and ice water surfaces, p_{liq} and p_{ice}, is approximated as in Sonntag (1994):

$$p_{\text{liq}}(T) =$$
$$100\exp[-6096.9385/T + 16.635794 - 0.02711193T$$
$$+ 1.67395210^{-5}T^2 + 2.433502\ln(T)] \tag{A1}$$

$$p_{\text{ice}}(T) =$$
$$100\exp[-6024.5282/T + 24.7219 + 0.010613868T$$
$$- 1.319882510^{-5}T^2 - 0.49382577\ln(T)] \tag{A2}$$

The equation for ice saturation agrees better than 1 % with approximations recommended by Murphy and Koop (2005) for temperatures down to $-100\,°C$. Somewhat larger differences are found for liquid saturation.

A4 Altitude in the standard atmosphere

In the ICAO standard atmosphere ($T = 15\,°C$ at the surface, decreasing linearly with constant laspe rate $dT/dz = -6.5\,\text{K km}^{-1}$ up to $T = -56.5\,°C$ at 11 km altitude, and constant above), the flight level z is converted to a static pressure p according to the standard atmosphere of aviation (ICAO, 1964), for p in Pa and z in m: In the troposphere ($z < 11000\,\text{m}$, $p > 22632\,\text{Pa}$),

$$p_{\text{ICAO}} = 101325(1 - 2.2557710^{-5}z)^{5.25589},$$
$$z_{\text{ICAO}} = 44330.8[1 - (p/101325)^{0.190263}]. \tag{A3}$$

Otherwise,

$$p_{\text{ICAO}} = 22632\exp[-1.5768910^{-4}(z - 11000)],$$
$$z_{\text{ICAO}} = [11000 - 6341.62\ln(p/22632)]. \tag{A4}$$

A5 Contrail formation conditions

The SAC requires computing a threshold temperature $T_{LC} \leq T_{LM}$ depending on ambient relative humidity over liquid water $U = \text{RHi} p_{ice}(T)/p_{liq}(T)$ and the steepness G of the mixing line, see Eq. (11).

The exact solutions for T_{LM} and T_{LC} follow implicitly from (Schumann, 1996)

$$p'_{liq}(T_{LM}) = G \tag{A5}$$

and

$$T_{LC} = T_{LM} - \frac{p_{liq}(T_{LM}) - U p_{liq}(T_{LC})}{G}. \tag{A6}$$

For $U \ll 1$ and $U = 1$, and for given T_{LM}, e.g., from Eq. (10), an explicit solution for the threshold temperature T_{LC} follows from:

$$T_{LC} = T_{LM} - (1 - U)p_{liq}(T_{LM})/G \text{ and } T_{LC} = T_{LM}, \tag{A7}$$

respectively. So far, no explicit approximation was available for T_{LC}, for $0 < U < 1$.

A solution can be found by solving Eq. (A6) iteratively for given humidity U and value of G. To start the iteration we use a quadratic Taylor series of $p_{liq}(T_{LM})$ around T_{LM} with $\Delta T = T_{LM} - T_{LC}$,

$$p_{liq}(T_{LC}) \approx$$
$$p_{liq}(T_{LM}) - \Delta T p\prime_{liq}(T_{LM}) + \frac{\Delta T^2}{2} p''_{liq}(T_{LM}). \tag{A8}$$

With this series, Eq. (A6) implies

$$T_{LC} = T_{LM} + A - \sqrt{A^2 + 2B}. \tag{A9}$$

Schumann (1996) gives expressions for A and B requiring to calculate the second derivative of $p''_{liq}(T_{LC})$ with respect to T. (Eq. 34 of this reference contains a mistake:

U^2 should be replaced by U (Ferrone, 2011).) The second derivative of $p_{\text{liq}}(T)$ can be approximated by (e.g., Ferrone, 2011)

$$p''_{\text{liq}}(T_{\text{LM}}) \approx \frac{2p_{\text{liq}}(T_{L0})G^2}{p_{\text{liq}}(T_{\text{LM}})}. \tag{A10}$$

This gives

$$A = \frac{(1-U)p_{\text{liq}}(T_{\text{LM}})(T_{\text{LM}} - T_{L0})}{2U p_{\text{liq}}(T_{L0})}, \tag{A11}$$

$$B = A(T_{\text{LM}} - T_{L0}), T_{L0} = T_{\text{LM}} - p_{\text{liq}}(T_{\text{LM}})/G. \tag{A12}$$

The approximate result, Eq. (A9), deviates from the exact solution with maximum errors up to 0.3 K at humidity U near 0.92, nearly independent of G. Higher accuracy is achieved with a few Newton iteration steps:

$$F = p_{\text{liq}}(T_{\text{LM}}) - G(T_{\text{LM}} - T_{\text{LC}}) - U p_{\text{liq}}(T_{\text{LC}}), \tag{A13}$$

$$F' = G - U p\prime_{\text{liq}}(T_{\text{LC}}), \tag{A14}$$

$$\Delta T = F/F', T_{\text{LC}} = T_{\text{LC}} - \Delta T, \tag{A15}$$

until ΔT is less than about 0.001 K.

The iteration is delicate because it requires the first and second derivatives of the saturation pressure and because T_{LC} varies smoothly for low U but suddenly increases near $U = 1$, see Fig. 20. For these reasons, it was not easy to find better fitting approximations. The analytical solutions for a third order Taylor series instead of Eq. (A8) were found to be sensitive to round-off errors.

A suitable fit extends Eq. (A7):

$$T_{\text{LC}} = T_{\text{LM}} - (1-U)\frac{p_{\text{liq}}(T_{\text{LM}})}{G} - \Delta T_c, \tag{A16}$$

with a correction ΔT_c which is zero for $U = 0, 1$ and increases sharply near $U = 1$,

$$\Delta T_c = F_1 U [W - F_2 (1 - W)], \tag{A17}$$

with

$$F_1 = x_1 + x_3 \ln(G), \ W = (1 - U^2)^{x_2}, \tag{A18}$$

$$F_2 = \left[\frac{1}{4} - (U - \frac{1}{2})^2 \right]^4. \tag{A19}$$

The fit uses three fit coefficients $x_1 = 5.68618$, $x_2 = 0.38395$, $x_3 = 0.65936$. The maximum error is $0.13\,\text{K}$ over the full range $0 \le U \le 1$, $0.24\,\text{Pa}\,\text{K}^{-1} < G < 23\,\text{Pa}\,\text{K}^{-1}$, see Fig. 19. It is efficient because T_{LC} is computed with just one evaluation of $p_{\text{liq}}(T_{\text{LM}})$.

A6 Contributions of emitted heat and water and latent heat release

Engine water emissions increase the relative humidity over ice within the plume as a function of dilution, $\Delta\text{RHi} = \text{EI}_{\text{H}_2\text{O}} R_1 p / (R_0 p_{\text{ice}}(T) N_{\text{dil}}(t))$. The dilution can be estimated from Eq. (18). Figure 21 shows the change in relative humidity versus time after emission for selected values of ambient temperature T ($200\,\text{K}$ and $240\,\text{K}$) and pressure p ($100\,\text{hPa}$ and $400\,\text{hPa}$). The water vapor emission contributes considerably to relative humidity at low temperatures (where ambient air contains little water vapor). The contribution increases linearly with pressure because the plume mass, over which the emissions get spread, increases with pressure. Hence, the emitted water vapor is important (order 5 % or larger) for times up to about one hour at low temperatures near $200\,\text{K}$. For higher temperatures, near $240\,\text{K}$, the emitted water vapor is important only for shorter times, up to about a minute.

The temperature increase ΔT due to combustion heat release is $\Delta T = Q_{\text{fuel}}(1 - \eta)/(c_p N_{\text{dil}}(t))$, see Fig. 22. For comparison, we note that a vertical potential temperature gradient of typically $0.003\,\text{K}\,\text{m}^{-1}$ in the troposphere implies $0.3\,\text{K}$ warming for $100\,\text{m}$ altitude increase. The combustion induced temperature increases stay below

0.3 K after about a minute. The warming by latent heat release by condensing all emitted water would be about a factor of ten smaller because the latent heat is so much smaller than the combustion heat.

Typical ice water contents in cirrus and contrails are

$I/(\text{mg m}^{-3}) = \exp(6.97 + 0.103 T/°\text{C})$

(Schumann, 2002; Schiller et al., 2008). If all this water gets sublimated, the resultant temperature change remains below 0.1 K in cold air, for $T < 240$ K.

A7 Advection near the Poles

To avoid singularities at the Poles, for large latitudes y, we invert the longitude (E) and latitude (N) coordinates x_n and y_n at the previous time step t_n first into Cartesian coordinates $\tilde{X}$, $\tilde{Y}$ (in the directions of 90° and 180° from the Pole), then compute advection over the time step $\Delta t = t_{n+1} - t_n$ with the horizontal velocity components U, V at (x_n, y_n) in ms^{-1}, and then return the new longitude/latitude coordinates x_{n+1}, y_{n+1} in degree. The angle α measures the negative longitude relative to the $\tilde{X}$-axis-direction.

$S_x = \sin(x_n \pi/180°)$, $C_x = \cos(x_n \pi/180°)$,
$X = S_x(90° - y_n)$, $Y = -C_x(90° - y_n)$,
$C_y = \cos(y_n \pi/180°)$,
$\tilde{U} = C_y U C_x - V S_x$, $\tilde{V} = C_y U S_x + V C_x$,
$\tilde{X} = x_n + \Delta t \tilde{U}$, $\tilde{Y} = y_n + \Delta t \tilde{V}$,
$Z = \tilde{X}^2 + \tilde{Y}^2$, $y_{n+1} = 90° - Z^{1/2}$,
$\alpha = \text{atan}(\tilde{Y}, \tilde{X}) 180°/\pi$, $x_{n+1} = 90° + \alpha$.

After call of this routine, one has to make sure (by adding or subtracting values of 360°) that consecutive way points are consecutive in longitude with increments less than 180°.

GMDD

4, 3185–3293, 2011

Contrail cirrus model

U. Schumann

Title Page

Abstract	Introduction
Conclusions	References
Tables	Figures

|◄ | ►|

◄ | ►

Back | Close

Full Screen / Esc

Printer-friendly Version

Interactive Discussion

A8   Flight and contrail segments passing the date line

Flights across the Pacific and some flights near the Poles pass the date line at $\pm 180°$ once or several times. On input, flight way points are given consecutively with small longitude increments (we require increment less than $300°$, which should be sufficient even close to the Poles). However, flights passing the date line, with some longitude values exceeding $180°$ in magnitude require special attention.

For contrail analysis, all segment coordinates are left unchanged and as evolving from the input. This allows for straightforward computation of segment length and direction values (the latter is needed for computing the horizontal velocity component V_n normal to the segment). Only for interpolation in NWP data, we shift longitudes by $\pm 360°$ into the inner range $-180° < x \leq 180°$.

However for plots and related analysis, one needs to map the flight paths and contrail segment coordinates to the inner range. This is done (in module TESTD) by inserting two extra points into a segment whenever passing the date line, one with $x = 180°$, the other with $x = -180°$, where the sequence depends on the flight direction. All other contrail properties are interpolated linearly between the original endpoints to the new end points. Special care was needed with input coordinates $|x| > 540°$. Such rare segments crossing this secondary date line are eliminated from further analysis (in module LIMITX).

A9   Subgrid-scale vertical velocity variance

The kinetic energy of mesoscale subgrid-scale turbulent motions e per unit mass and its vertical variance part w'_{meso} as needed in Eq. (57), are computed following Schumann (1991):

$$e = \ell_e(\ell_m S_T^2 - \ell_h N_{BV}^2), \tag{A20}$$

$$w'^2_{SGS}/e = (2/3)[\ell_h/(c_h\ell)]^2, \tag{A21}$$

with

$$\ell_h = c_h \ell e/(e + 0.3\ell^2 N_{BV}^2),$$
$$\ell_\varepsilon = \ell/c_\varepsilon, \ell_m = c_m \ell. \tag{A22}$$

Most of the model coefficients are consequences of an inertial range spectrum assumed at subgrid scales (Schumann, 1991): $c_\varepsilon = 0.845$, $c_m = 0.0856$, $c_h = 0.204$. The NWP grid scale is set to $\ell = 700\,\text{m}$. A larger ℓ implies a smaller E_{meso} in Eq. (57). Hence this is essentially not an additional free parameter in this application.

Because of the dependence of ℓ_h on e, these equations are quadratic in e. The solution is $e = b + \sqrt{b^2 + c}$, with $b = \alpha_S S_T^2 + \alpha_N N_{BV}^2$, $c = \alpha_c S_T^2 N_{BV}^2$, $\alpha_S = \ell_\varepsilon \ell_m/2$, $\alpha_N = (0.3\ell + \ell_\varepsilon c_h)\ell/2$, $\alpha_c = 0.3\ell^2 \ell_\varepsilon \ell_m$. The solution e is non-negative for any positive or negative stratification.

Normalized results are functions of the Richardson number Ri. The energy e stays rather large, but the turbulence becomes highly anisotropic with decreasing w'^2_{SGS} for growing Ri. The ratio of vertical to total kinetic SGS energy w'^2_{SGS}/e is (2/3) for locally isotropic turbulence at weak stratification and tends to zero for $\ell^2 N_{BV}^2/e \to 0$, see Fig. 23.

For $S_T = 0.002\,\text{s}^{-1}$, $N_{BV} = 0.02\,\text{s}^{-1}$, the result is $e \approx 0.11\,\text{m}^2\,\text{s}^{-2}$, which is within the range of measured values (Schumann et al., 1995). For $Ri \approx 10$, the modeled ratio is $w'^2/e \approx 0.02$, while the measurements show a ratio of about 0.15. Therefore, we enhance w'^2_{SGS} by adding the variance of mean vertical motions $\bar{w}$ at grid scales, see Eq. (56).

A10 Particle number integration

For the number of particles per contrail length, we need to integrate an ordinary differential equation of the form

$$N' = -AN^2 - BN, N(0) = N_0 \tag{A23}$$

The analytical solution of this equation is:

$$N(t) = \frac{BN_0 e^{-Bt}}{B + AN_0(1 - e^{-Bt})}, \text{ for } Bt > 0.$$ (A24)

The solution simplifies to

$$N(t) = \frac{N_0}{1 + AN_0}, \text{ for } Bt \ll 1,$$ (A25)

5   $$N(t) = N_0 e^{-Bt}, \text{ for } AN_0 \ll B.$$ (A26)

A11   One-dimensional Gaussian integral

The function $f_\tau(y)$, Eq. (65), follows from
$f_\tau(y) = (B/A)I(y),$ with
$I(y) = \int_{-\infty}^{\infty} \exp[-(1/2)\mathbf{x}^T \sigma^{-1} \mathbf{x}] dz.$

10   This integral can be evaluated (Abramowitz and Stegun, 1964, 7.4.2, 7.1.2 and 7.1.9),
$I(y) = \int_{-\infty}^{\infty} \exp[-(az^2 + 2bz + c)] dz$
$= (\pi/a)^{1/2} \exp[(b^2 - ac)/a]$
where

15   $a = (1/2)\sigma_{yy}/\det\sigma, \; b = (1/2)\sigma_{yz}/\det\sigma,$
and $c = (1/2)\sigma_{zz}/\det\sigma.$
With Eqs. (3, 8),
$A = 2\pi(\det\sigma)^{1/2}$ and $\sigma_{yy} = B^2/8,$
this results into Eq. (65),

20   $f_\tau(y) = (4/\pi)^{1/2}(A/B)\exp[-(1/2)y^2/\sigma_{yy}],$
independent of $\sigma_{yz}.$

A12 Contrail segment contribution to optical depth in the cloud-mask

For given Cartesian segment end-point $(x_1,y_1),(x_2,y_2)$, we compute the contribution of the segment to the optical depth $\tau_{0,0}$ at the pixel position, e.g. at (x_0,y_0), using linear geometry, see Fig. 24, as follows.

First, a parameter w is computed which is between 0 and 1 if the normal from (x_0,y_0) crosses the segment line between the given end points:

$$\Delta x_0 = x_2 - x_1$$
$$\Delta y_0 = y_2 - y_1$$
$$\det = (\Delta x_0)^2 + (\Delta y_0)^2$$
$$\Delta x_1 = x_0 - x_1$$
$$\Delta y_1 = y_0 - y_1$$
$$w = (\Delta x_1 \Delta x_0 + \Delta y_1 \Delta y_0)/\det$$

where $\det > 0$ needs to be checked. If the cross-point (x_s,y_s) is within the segment line, i.e., for $(|w - 1/2| < 1/2)$ we compute the distance s to the pixel point and with this the contribution to optical depth.

$$x_s = x_1 + w(x_2 - x_1)$$
$$y_s = y_1 + w(y_2 - y_1)$$
$$s^2 = (x_0 - x_s)^2 + (y_0 - y_s)^2$$
$$B = w B_2 + (1 - w) B_1$$
$$\delta = s^2/(B^2/8)$$
$$\gamma = (4/\pi)^{1/2} \exp[-(1/2)\delta]$$
$$\tau = w \tau_2 + (1 - w)\tau_1$$
$$\tau_{0,0} := \tau_{0,0} + \gamma \tau$$

Here B_m and τ_m are the contrail width and optical depth at the segment end points, $m = 1,2$.

Contrail cirrus model

U. Schumann

Title Page

Abstract | Introduction

Conclusions | References

Tables | Figures

|◄ | ►|

◄ | ►

Back | Close

Full Screen / Esc

Printer-friendly Version

Interactive Discussion

References

Abramowitz, M. and Stegun, I. A.: Handbook of Mathematical Functions, Dover Publisher, New York, 1964. 3203, 3238, 3246

Adelfang, S. I.: On the relations between wind shears over various altitude intervals, J. Appl. Meteor., 10, 156–159, 1971. 3211

Appleman, H.: The formation of exhaust contrails by jet aircraft, B. Am. Meteor. Soc., 34, 14–20, 1953. 3186, 3187, 3194

Atlas, D. and Wang, Z.: Contrails of small and very large optical depth, J. Atmos. Sci., 67, 3065–3073, doi:10.1175/2010JAS3403.1, 2010. 3187, 3216, 3222

Atlas, D., Wang, Z., and Duda, D. P.: Contrails to cirrus – Morphology, microphysics, and radiative properties, J. Appl. Meteor. Climatol., 45, 5–19, 2006. 3186, 3187, 3188, 3210, 3211, 3216, 3232

Bakan, S., Betancor, M., Gayler, V., and Gral, H.: Contrail frequency over Europe from NOAA-satellite images, Ann. Geophys., 12, 962–968, doi:10.1007/s00585-994-0962-y, 1994. 3187, 3215, 3216

Birner, T., Dörnbrack, A., and Schumann, U.: How sharp is the tropopause at midlatitudes?, Geophys. Res. Lett., 29, 45–1–45–4, doi:10.1029/2002gl015142, 2002. 3207

Blanco-Muriel, M., Alarcón-Padilla, D. C., López-Moratella, T., and Lara-Coira, M.: Computing the solar vector, Solar Energy, 70, 431–441, 2001. 3223

Brown, R. C., Miake-Lye, R. C., Anderson, M. R., and Kolb, C. E.: Aircraft sulphur emissions and

Contrail cirrus model

U. Schumann

the formation of visible contrails, Geophys. Res. Lett., 12, 385–388, doi:10.1029/97GL00107, 1997. 3187, 3200, 3201

Burkhardt, U. and Kärcher, B.: Global radiative forcing from contrail cirrus, Nature Clim. Change, 1, 54–58, doi:10.1038/NCLIMATE1068, 2011. 3187

5 Burkhardt, U., Kärcher, B., and Schumann, U.: Global modelling of the contrail and contrail cirrus climate impact, B. Am. Meteor. Soc., 91, 479–484, doi:10.1175/2009BAMS2656.1, 2010. 3187

Busen, R. and Schumann, U.: Visible contrail formation from fuels with different sulfur contents, Geophys. Res. Lett., 22, 1357–1360, doi:10.1029/95GL01312, 1995. 3200

10 Cariolle, D., Caro, D., Paoli, R., Hauglustaine, D. A., Cuenot, B., Cozic, A., and Paugam, R.: Parameterization of plume chemistry into large-scale atmospheric models: Application to aircraft NO_x emissions, J. Geophys. Res., 114, D19302, doi:10.1029/2009JD011873, 2009. 3187

Chlond, A.: Large eddy simulations of contrails, J. Atmos. Sci., 55, 796–819, 1998. 3188, 3216

15 Clayson, C. A. and Kantha, L.: On turbulence and mixing in the free atmosphere inferred from high-resolution soundings, J. Atmos. Oceanic Technol., 25, 833–852, 2008. 3208

Danilin, M., Ebel, A., Elbern, H., and Petry, H.: Evolution of the concentrations of trace species in an aircraft plume: Trajectory study, J. Geophys. Res., 99, 18951–18972, doi:10.1029/94JD01820, 1994. 3191, 3203

20 deBruin, A. and Kannemans, H.: Analysis of NLR Cessna Citation flight test data for flight test-1 in AWIATOR project, Tech. rep., NLR, Techn. Report AW-NLR-113-010, 2004. 3272

Delisi, D. P. and Robins, R.: Short-scale instabilities in trailing wake vortices in a stratified fluid, AIAA J., 38, 1916–1923, 2000. 3272

Detwiler, A. and Pratt, R.: Clear-air seeding: Opportunities and strategies, J. Wea. Mod., 16, 25 46–60, 1984. 3187, 3211, 3216

Dewan, E. M.: Stratospheric wave spectra resembling turbulence, Science, 204, 832–835, doi:10.1126/science.204.4395.832, 1979. 3207

Dörnbrack, A. and Dürbeck, T.: Turbulent dispersion of aircraft exhausts in regions of breaking gravity waves, Atmos. Environ., 32, 3105–3112, 1998. 3207, 3208

30 Duda, D., Minnis, P., and Nguyen, L.: Estimates of cloud radiative forcing in contrail clusters using GOES imagery, J. Geophys. Res., 106, 4927–4937, 2001. 3187, 3216

Duda, D., Minnis, P., Nyuyen, L., and Palikonda, R.: A case study of the development of contrail clusters over the Great Lakes, J. Atmos. Sci., 61, 1132–1146, 2004. 3188, 3211, 3216, 3220

Duda, D. P., Palikonda, R., and Minnis, P.: Relating observations of contrail persistence to numerical weather analysis output, Atmos. Chem. Phys., 9, 1357–1364, doi:10.5194/acp-9-1357-2009, 2009. 3187, 3188

Dürbeck, T. and Gerz, T.: Large-eddy simulation of aircraft exhaust plumes in the free atmosphere: Effective diffusivities and cross-sections, Geophys. Res. Lett., 22, 3203–3206, doi:10.1029/95GL03021, 1995. 3191, 3209

Dürbeck, T. and Gerz, T.: Dispersion of aircraft exhausts in the free atmosphere, J. Geophys. Res., 101, 26007–26015, 1996. 3191, 3207, 3209, 3211

EUROCONTROL: Aircraft Performance Summary Tables for the Base of Aircraft Date (BADA), Revision 3.7, Tech. rep., European Organisation for the Safety of Air Navigation, 2009. 3194

Eyers, C. J., Addleton, D., Atkinson, K., Broomhead, M. J., Christou, R., Elliff, T., Falk, R., Gee, I., Lee, D. S., Marizy, C., Michot, S., Middel, J., Newton, P., Norman, P., Plohr, M., Raper, D., and Stanciou, N.: AERO2k Global Aviation Emissions Inventories for 2002 and 2025, Tech. rep., QinetiQ for European Commission under Contract No. G4RD-CT-2000-00382, http://www.cate.mmu.ac.uk/aero2k.asp, 2004. 3194

Fahey, D., Schumann, U., Ackerman, S., Artaxo, P., Boucher, O., Danilin, M. Y., Kärcher, B., Minnis, P., Nakajima, T., and Toon, O. B.: Aviation-produced aerosols and cloudiness, in: Aviation and the Global Atmosphere. A Special Report of IPCC Working Groups I and III, edited by: Penner, J. E., Lister, D. H., Griggs, D. J., Dokken, D. J., and McFarland, M., 65–120, Cambridge University Press, New York, http://www.ipcc.ch/ipccreports/sres/aviation/index.php?idp=0, 1999. 3187, 3200

Febvre, G., Gayet, J.-F., Minikin, A., Schlager, H., Shcherbakov, V., Jourdan, O., Busen, R., Fiebig, M., Kärcher, B., and Schumann, U.: On optical and microphysical characteristics of contrails and cirrus, J. Geophys. Res., 114, D02204, doi:10.1029/2008JD010184, 2009. 3233, 3234, 3265

Ferrone, A.: Aviation and climate change in Europe: from regional climate modelling to policy-options, Ph.D. thesis, Université Catholique de Louvain, 2011. 3241

Frehlich, R. and Sharman, R.: Climatology of velocity and temperature turbulence statistics determined from rawinsonde and ACARS/AMDAR data, J. Appl. Meteor. Climatol., 49, 1149–1169, doi:10.1175/2010JAMC2196, 2010. 3208

Freudenthaler, V., Homburg, F., and Jäger, H.: Contrail observations by ground-based scanning lidar: Cross-sectional growth, Geophys. Res. Lett., 22, 3501–3504, doi:10.1029/95GL03549, 1995. 3191, 3211, 3229

Garber, D. P., Minnis, P., and Costulis, P. K.: A commercial flight track database for upper tropospheric aircraft emission studies over the USA and southern Canada, Meteor. Z., 14, 445–452, 2005. 3193

Gayet, J.-F., Febvre, G., Brogniez, G., Chepfer, H., Renger, W., and Wendling, P.: Microphysical and optical properties of cirrus and contrails, J. Atmos. Sci., 53, 126–138, 1996. 3220

Gerz, T. and Ehret, T.: Wake dynamics and exhaust distribution behind cruising aircraft, in: The Characterization and Modification of Wakes from Lifting Vehicles in Fluids, 35.1–35.8, AGARD CP 584, 1996. 3188

Gerz, T., Dürbeck, T., and Konopka, P.: Transport and effective diffusion of aircraft emissions, J. Geophys. Res., 103, doi:10.1029/98JD02282, 1998. 3191

Gierens, K.: Numerical simulations of persistent contrails, J. Atmos. Sci., 53, 3333–3348, 1996. 3188, 3201

Gierens, K. and Bretl, S.: Analytical treatment of ice sublimation and test of sublimation parameterisations in twomoment ice microphysics models, Atmos. Chem. Phys., 9, 7481–7490, doi:10.5194/acp-9-7481-2009, 2009. 3202, 3216, 3217

Gierens, K. and Jensen, E.: A numerical study of the contrail-to-cirrus transition, Geophys. Res. Lett., 25, 4341–4344, 1998. 3188

Gierens, K. and Spichtinger, P.: On the size distribution of ice-supersaturated regions in the upper troposphere and lowermost stratosphere, Ann. Geophys., 18, 499–504, doi:10.1007/s00585-000-0499-7, 2000. 3215

Gierens, K., Schumann, U., Helten, M., Smit, H., and Marenco, A.: A distribution law for relative humidity in the upper troposphere and lower stratosphere derived from three years of MOZAIC measurements, Ann. Geophys., 17, 1218–1226, doi:10.1007/s00585-999-1218-7, 1999. 3214

Gierens, K., Kärcher, B., Mannstein, H., and Mayer, B.: Aerodynamic contrails: Phenomenology and flow physics, J. Atmos. Sci., 66, 217–226, doi:10.1175/2008JAS2767.1, 2009. 3201

Gierens, K. M.: The influence of radiation on the diffusional growth of ice crystals, Beitr. Phys. Atmos., 67, 181–193, 1994. 3216

Green, J. E.: Greener by design – the technology challenge, Aeron. J., 106, 57–113, 2002. 3187

Gultepe, I. and Starr, D. O.: Dynamical structure and turbulence in cirrus clouds: Aircraft observations during FIRE, J. Atmos. Sci., 52, 4159–4182, 1995. 3197, 3208

Hansen, J. E. and Travis, L. D.: Light scattering in planetary atmospheres, Space Sci. Rev., 16,

Contrail cirrus model

U. Schumann

Back | Close

Full Screen / Esc

Printer-friendly Version

Interactive Discussion

527–610, 1974. 3221

Haywood, J. M., Allan, R. P., Bornemann, J., Forster, P. M., Francis, P. N., Milton, S., Rädel, G., Rap, A., Shine, K. P., and Thorpe, R.: A case study of the radiative forcing of persistent contrails evolving into contrail-induced cirrus, J. Geophys. Res., 114, D24201, doi:10.1029/2009JD012650, 2009. 3187, 3192, 3216

Hennemann, I.: Deformation und Zerfall von Flugzeugwirbelschleppen in turbulenter und stabil geschichteter Atmosphäre, Tech. rep., Deutsches Zentrum für Luft- und Raumfahrt, Forschungsbericht 2010–21, 2010. 3272

Heymsfield, A. J., Lawson, R. P., and Sachse, G. W.: Growth of ice crystals in a precipitating contrail, Geophys. Res. Lett., 25, 1335–1338, 1998. 3186, 3199, 3232

Holzäpfel, F.: Probabilistic two-phase wake vortex decay and transport model, J. Aircraft, 40, 323–331, 2003. 3196, 3197, 3272

Holzäpfel, F. and Gerz, T.: Two-dimensional wake vortex physics in the stably stratified atmosphere, Aeros. Sci. Techn., 5, 261–270, 1999. 3194, 3197, 3199

Holzäpfel, F., Misaka, T., and Hennemann, I.: Wake-vortex topology, circulation, and turbulent exchange processes, in: AIAA Paper 2010-7992, 1–16, 2010. 3188, 3191

Houchi, K., Stoffelen, A., Marseille, G. J., and De Kloe, J.: Comparison of wind and wind shear climatologies derived from high-resolution radiosondes and the ECMWF model, J. Geophys. Res., 115, D22123, doi:10.1029/2009JD013196, 2010. 3207, 3210

Huebsch, W. W. and Lewellen, D. C.: Sensitivity study on contrail evolution, in: 36th AIAA Fluid Dynamics Conference and Exhibit, AIAA 2006–3749, 1–14, 2006. 3202

Hunt, J. C. R.: Diffusion in the stably stratified atmospheric boundary layer, J. Climate Appl. Meteor., 24, 1187–1195, 1985. 3210

Hunt, J. C. R., Stretch, D. D., and Britter, R. E.: Length scales in stably stratified turbulent flows and their use in turbulence models, in: Stably Stratified Flows and Dense Gas Dispersion, edited by Puttock, J. S., 285–321, Clarendon, 1988. 3208, 3209

ICAO: Manual of the ICAO Standard Atmosphere, Tech. rep., ICAO Document No. 7488, 2nd Edition, 1964. 3193

Immler, F., Treffeisen, R., Engelbart, D., Krger, K., and Schrems, O.: Cirrus, contrails, and ice supersaturated regions in high pressure systems at northern mid latitudes, Atmos. Chem. Phys., 8, 1689–1699, doi:10.5194/acp-8-1689-2008, 2008. 3187, 3211, 3215

IPCC: Climate Change 2007: The Physical Science Basis. Contribution of Working Group I to the Fourth Assessment Report of the Intergovernmental Panel on Climate Change,

Cambridge Univ. Press, Cambridge, UK, 2007. 3187

Jensen, E. J., Ackermann, A. S., Stevens, D. E., Toon, O. B., and Minnis, P.: Spreading and growth of contrails in a sheared environment, J. Geophys. Res., 103, 13557–13567, 1998a. 3188, 3216, 3232

5 Jensen, E. J., Toon, O. B., Pueschel, R. F., Goodman, J., Sachse, G. W., Anderson, B. E., Chan, K. R., Baumgardner, D., and Miake-Lye, R. C.: Ice crystal nucleation and growth in contrails forming at low ambient temperatures, Geophys. Res. Lett., 25, 1371–1374, doi:10.1029/97GL03592, 1998b. 3187, 3200, 3201

Kantha, L. and Hocking, W.: Dissipation rates of turbulence kinetic energy in the free 10 atmosphere: MST radar and radiosondes, J. Atm. Sol. Terr. Phys., 73, 1043–1051, doi:10.1016/j.jastp.2010.11.024, 2011. 3208

Kärcher, B.: A trajectory box model for aircraft exhaust plumes, J. Geophys. Res., 100, 18835–18844, doi:10.1029/95JD01638, 1995. 3191

Kärcher, B.: Physicochemistry of aircraft-generated liquid aerosols, soot, and ice particles: 1. 15 Model description, J. Geophys. Res., 103, 17111–17128, 1998. 3187, 3200, 3201

Kärcher, B. and Ström, J.: The roles of dynamical variability and aerosols in cirrus cloud formation, Atmos. Chem. Phys., 3, 823–838, doi:10.5194/acp-3-823-2003, 2003. 3216, 3218

Kärcher, B. and Yu, F.: Role of aircraft soot emissions in contrail formation, Geophys. Res. Lett., 36, L01804, doi:10.1029/2008GL036649, 2009. 3194, 3201

20 Kärcher, B., Peter, T., Biermann, U. M., and Schumann, U.: The initial composition of jet condensation trails, J. Atmos. Sci., 53, 3066–3083, 1996. 3187, 3200

Kärcher, B., Busen, R., Petzold, A., Schröder, F. P., Schumann, U., and Jensen, E. J.: Physicochemistry of aircraft-generated liquid aerosols, soot, and ice particles. 2. Comparison with observations and sensitivity studies, J. Geophys. Res., 103, 17129–17147, 1998. 3188, 25 3200, 3201

Krcher, B., Burkhardt, U., Unterstrasser, S., and Minnis, P.: Factors controlling contrail cirrus optical depth, Atmos. Chem. Phys., 9, 6229–6254, doi:10.5194/acp-9-6229-2009, 2009a. 3187, 3201, 3202, 3216, 3217, 3222

Kärcher, B., Mayer, B., Gierens, K., Burkhardt, U., Mannstein, H., and Chatterjee, R.: 30 Aerodynamic contrails: Microphysics and optical properties, J. Atmos. Sci., 66, 227–243, doi:10.1175/2008JAS2768.1, 2009b. 3201

Karol, I. L., Ozolin, Y. E., and Rozanov, E. V.: Box and Gaussian plume models of the exhaust composition evolution of subsonic transport aircraft in- and out of the flight corridor, Ann.

Contrail cirrus model

U. Schumann

Title Page

Abstract	Introduction
Conclusions	References
Tables	Figures

|◄ | ►|

◄ | ►

Back | Close

Full Screen / Esc

Printer-friendly Version

Interactive Discussion

Geophys., 15, 88–96, doi:10.1007/s00585-997-0088-0, 1997. 3191

Knollenberg, R.: Measurements of the growth of the ice budget in a persisting contrail, J. Atmos. Sci., 29, 1367–1374, 1972. 3186

Koch, A., Nagel, B., Gollnick, V., Dahlmann, K., Grewe, V., Kärcher, B., and Schumann, U.: Integrated analysis and design environment for a climate compatible air transport system, in: 9th AIAA Aviation Technology, Integration and Operations (ATIO) Conference, pp. AIAA 2009–7050, AIAA, 2009. 3187

Konopka, P.: Analytical Gaussian solutions for anisotropic diffusion in a linear shear flow, J. Non.-Equilib. Thermodyn., 20, 78–91, 1995. 3189, 3190, 3205, 3206

Konrad, T. G. and Howard, J. C.: Multiple contrail streamers observed by radar, J. Appl. Meteor., 13, 563–572, 1974. 3220

Koop, T., Luo, B., Tsias, A., and Peter, T.: Water activity as the determinant for homogeneous ice nucleation in aqueous solutions, Nature, 406, 611–614, 2000. 3192, 3234

Kraabøl, A. G., Flatøy, F., and Stordal, F.: Impact of NO_x emissions from subsonic aircraft: Inclusion of plume processes in a three-dimensional model covering Europe, North America, and the North Atlantic, J. Geophys. Res., 105, 3573–3581, 2000. 3191

Krämer, M., Schiller, C., Afchine, A., Bauer, R., Gensch, I., Mangold, A., Schlicht, S., Spelten, N., Sitnikov, N., Borrmann, S., de Reus, M., and Spichtinger, P.: Ice supersaturations and cirrus cloud crystal numbers, Atmos. Chem. Phys., 9, 3505–3522, doi:10.5194/acp-9-3505-2009, 2009. 3195, 3220

Lamquin, N., Gierens, K., Stubenrauch, C. J., and Chatterjee, R.: Evaluation of upper tropospheric humidity forecasts from ECMWF using AIRS and CALIPSO data, Atmos. Chem. Phys., 9, 1779–1793, doi:10.5194/acp-9-1779-2009, 2009. 3192

Lee, D., Pitari, G., Grewe, V., Gierens, K., Penner, J. E., Petzold, A., Prather, M. J., Schumann, U., Bais, A., Berntsen, T., Iachetti, D., Lim, L. L., and Sausen, R.: Transport impacts on atmosphere and climate: Aviation, Atmos. Environ., 44, 4678–4734, doi:10.1016/j.atmosenv.2009.06.005, 2010. 3187, 3196

Lewellen, D. C. and Lewellen, W. S.: Large-eddy simulations of the vortex-pair breakup in aircraft wakes, AIAA J., 34, 2337–2345, 1996. 3188, 3197

Lewellen, D. C. and Lewellen, W. S.: The effects of aircraft wake dynamics on contrail development, J. Atmos. Sci., 58, 390–406, 2001. 3188, 3191, 3194, 3199, 3200, 3201

Lilly, D. K.: The representation of small-scale turbulence in numerical simulation experiments, in: IBM Sci. Comput. Symp. on Environm. Sci., 195–210, Thomas J. Watson Res. Center,

Contrail cirrus model

U. Schumann

Title Page

Abstract | Introduction

Conclusions | References

Tables | Figures

|◄ | ►|

◄ | ►

Back | Close

Full Screen / Esc

Printer-friendly Version

Interactive Discussion

Yorktown Heights, N.Y., IBM Form 320-1951, 1967. 3211

Manney, G. L., Hegglin, M. I., Daffer, W. H., Santee, M. L., Ray, E. A., Pawson, S., Schwartz, M. J., Boone, C. D., Froidevaux, L., Livesey, N. J., Read, W. G., and Walker, K. A.: Jet characterization in the upper troposphere/lower stratosphere (UTLS): applications to climatology and transport studies, Atmos. Chem. Phys., 11, 6115–6137, doi:10.5194/acp-11-6115-2011, 2011. 3207

Mannstein, H. and Schumann, U.: Aircraft induced contrail cirrus over Europe, Meteor. Z., 14, 549–554, 2005. 3187

Mannstein, H., Meyer, R., and Wendling, P.: Operational detection of contrails from NOAA-AVHRR data, Int. J. Rem. Sens., 20, 1641–1660, 1999. 3215

Mannstein, H., Spichtinger, P., and Gierens, K.: How to avoid contrail cirrus, Transp. Res., D 10, 421–426, 2005. 3187

Mayer, B. and Kylling, A.: Technical note: The libRadtran software package for radiative transfer calculations – description and examples of use, Atmos. Chem. Phys., 5, 1855–1877, doi:10.5194/acp-5-1855-2005, 2005. 3223

Meerktter, R., Schumann, U., Doelling, D. R., Minnis, P., Nakajima, T., and Tsushima, Y.: Radiative forcing by contrails, Ann. Geophys., 17, 1080–1094, doi:10.1007/s00585-999-1080-7, 1999. 3224

Meilinger, S. K., Krcher, B., and Peter, Th.: Microphysics and heterogeneous chemistry in aircraft plumes - high sensitivity on local meteorology and atmospheric composition, Atmos. Chem. Phys., 5, 533–545, doi:10.5194/acp-5-533-2005, 2005. 3187

Miake-Lye, R., Martinez-Sanchez, M., Brown, R., and Kolb, C. E.: Plume and wake dynamics, mixing and chemistry behind a high speed civil aircraft, J. Aircraft, 30, 467–479, 1993. 3187

Minnis, P., Young, D. F., Garber, D. P., Nguyen, L., Smith Jr., W. L., and Palikonda, R.: Transformation of contrails into cirrus during SUCCESS, Geophys. Res. Lett., 25, 1157–1160, 1998. 3187, 3216

Misaka, T., Holzäpfel, F., Hennemann, I., Gerz, T., Manhart, M., and Schwertfirm, F.: Vortex bursting and tracer transport of a counter-rotating vortex pair, Phys. Fluids, submitted, 2012. 3188, 3191

Mitchell, D. L. and Heymsfield, A. H.: Refinements in the treatment of ice particle terminal velocities, highlighting aggregates, J. Atmos. Sci., 62, 1637–1644, 2005. 3218

Murphy, D. M. and Koop, T.: Review of the vapour pressures of ice and supercooled water for atmospheric applications, Q. J. Roy. Meteor. Soc., 131, 1539–1565, doi:10.1256/qj.04.94,

Contrail cirrus model

U. Schumann

Title Page

Abstract | Introduction

Conclusions | References

Tables | Figures

|◄ | ►|

◄ | ►

Back | Close

Full Screen / Esc

Printer-friendly Version

Interactive Discussion

2005. 3239

Naiman, A. D., Lele, S. K., Wilkerson, J. T., and Jacobson, M. Z.: Parameterization of sub-grid plume dilution for use in large-scale atmospheric simulations, Atmos. Chem. Phys., 10, 2551–2560, doi:10.5194/acp-10-2551-2010, 2010. 3188, 3191, 3209

Nair, R. D., Scroggs, J. S., and Semazzi, F. H. M.: A forward-trajectory global semi-Lagrangian transport scheme, J. Comput. Phys., 190, 275–294, doi:10.1016/S0021-9991(03)00274-2, 2003. 3203

Nastrom, G. D. and Gage, K. S.: A climatology of atmospheric wavenumber spectra of wind and temperature observed by commerical aircraft, J. Atmos. Sci., 42, 950–960, 1985. 3207

Paltridge, G. W. and Platt, C. M. R.: Radiative processes in meteorology and climatology, Elsevier, Amsterdam, 1976. 3223

Paoli, R. and Garnier, F.: Interaction of exhaust jets and aircraft wake vortices: small-scale dynamics and potential microphysical-chemical transformations, Compt. Rend. Phys., 6, 525–547, 2005. 3188

Paoli, R., Vancassel, X., Garnier, F., and Mirabel, P.: Large-eddy simulation of a turbulent jet and a vortex sheet interaction: particle formation and evolution in the near field of an aircraft wake, Meteor. Z., 17, 131–144, doi:10.1127/0941-2948/2008/0278, 2008. 3188, 3200, 3201

Paoli, R., Cariolle, D., and Sausen, R.: Review of effective emissions modeling and computation, Geosci. Model Dev., 4, 643–667, doi:10.5194/gmd-4-643-2011, 2011. 3187

Paugam, R., Paoli, R., and Cariolle, D.: Influence of vortex dynamics and atmospheric turbulence on the early evolution of a contrail, Atmos. Chem. Phys., 10, 3933–3952, doi:10.5194/acp-10-3933-2010, 2010. 3191, 3199

Pavelin, E., Whiteway, J. A., Busen, R., and Hacker, J.: Airborne observations of turbulence, mixing, and gravity waves in the tropopause region, J. Geophys. Res., 107, 4084, doi:10.1029/2001JD000775, 2002. 3208

Pisso, I., Real, E., Law, K. S., Legras, B., Bousserez, N., Attié, J. L., and Schlager, H.: Estimation of mixing in the troposphere from Lagrangian trace gas reconstructions during long-range pollution plume transport, J. Geophys. Res., 114, doi:10.1029/2008JD011289, 2009. 3208, 3209, 3211

Ponater, M., Brinkop, S., Sausen, R., and Schumann, U.: Simulating the global atmospheric response to aircraft water vapour emissions and contrails: a first approach using a GCM, Ann. Geophys., 14, 941–960, doi:10.1007/s00585-996-0941-6, 1996. 3195

Pruppacher, H. R. and Klett, J. D.: Microphysics of Clouds and Precipitation, Kluwer Academic

Title Page

Abstract | Introduction

Conclusions | References

Tables | Figures

◀ | ▶

◀ | ▶

Back | Close

Full Screen / Esc

Printer-friendly Version

Interactive Discussion

Publ., Dordrecht, 1997. 3217, 3218

Rädel, G. and Shine, K. P.: Evaluation of the use of radiosonde humidity data to pre-
dict the occurrence of persistent contrails, Q. J. Roy. Meteor. Soc., 133, 1413–1423,
doi:10.1002/qj.128, 2007, 2007. 3188, 3192, 3195

5   Riley, J. J. and Lindborg, E.: Stratified turbulence: A possible interpretation of some geophysi-
cal turbulence measurements, J. Atmos. Sci., 65, 2416–2424, doi:10.1175/2007JAS2455.1,
2008. 3207, 3208, 3211

Sarpkaya, T.: Trailing vortices in homogeneous and density-stratified media, J. Fluid Mech.,
136, 85–109, 1983. 3272

10 Sassen, K.: Contrail-cirrus and their potential for regional climate change, B. Am. Meteor. Soc.,
78, 1885–1903, 1997. 3187

Sausen, R., Gierens, K., Ponater, M., and Schumann, U.: A diagnostic study of the global
distribution of contrails. Part I: Present day climate, Theor. Appl. Clim., 61, 127–141, 1998.
3187

15 Schiller, C., Krämer, M., Afchine, A., Spelten, N., and Sitnikov, N.: Ice water content of Arctic,
midlatitude, and tropical cirrus, J. Geophys. Res., 113, D24208, doi:10.1029/2008JD010342,
2008. 3214, 3243, 3277

Schlager, H., Konopka, P., Schulte, P., Schumann, U., Ziereis, H., Arnold, F., Klemm, M., Hagen,
D. E., Whitefield, P. D., and Ovarlez, J.: In situ observations of air traffic emission signatures
20 in the North Atlantic flight corridor, J. Geophys. Res., 102, 10739–10750, 1997. 3191

Schmidt, E.: Die Entstehung von Eisnebel aus den Auspuffgasen von Flugmotoren, in:
Schriften der Deutschen Akademie der Luftfahrtforschung, Heft 44, 1–15, Verlag R. Old-
enbourg, München, 1941. 3186, 3194

Schröder, F., Kärcher, B., Duroure, C., Ström, J., Petzold, A., Gayet, J.-F., Strauss, B., Wendling,
25 P., and Borrmann, S.: The transition of contrails into cirrus clouds, J. Atmos. Sci., 57, 464–
480, 2000. 3220, 3233, 3234, 3265

Schumann, U.: Subgrid length-scales for large-eddy simulation of stratified turbulence, Theor.
Comput. Fluid Dyn., 2, 279–290, 1991. 3208, 3219, 3244, 3245

Schumann, U.: On the effect of emissions from aircraft engines on the state of the atmosphere,
30 Ann. Geophys., 12, 365–384, doi:10.1007/s00585-994-0365-0, 1994. 3210, 3232

Schumann, U.: On conditions for contrail formation from aircraft exhausts, Meteor. Z., 5, 4–23,
1996. 3186, 3188, 3194, 3195, 3217, 3240

Schumann, U.: Contrail cirrus, in: Cirrus, edited by: Lynch, D. K., Sassen, K., O'C. Starr, D.,

Contrail cirrus model

U. Schumann

⏮ | ⏭

◀ | ▶

Back | Close

Full Screen / Esc

Printer-friendly Version

Interactive Discussion

and Stephens, G., 231–255, Oxford Univ. Press, Oxford, 2002. 3214, 3243, 3277

Schumann, U.: A contrail cirrus prediction tool, in: Proceedings of the 2nd International Conference on Transport, Atmosphere and Climate (TAC-2), edited by: Sausen, R., van Velthoven, P. F. J., Brüning, C., and Blum, A., 69–74, Aachen, Germany, and Maastricht, The Netherlands, 22–25 June 2009, DLR-Forschungsbericht 2010-10, Cologne, Germany, ISSN 1434-8454, 2009. 3189

Schumann, U. and Gerz:, T.: Turbulent mixing in stably stratified shear flows, J. Appl. Meteor., 34, 33–48, 1995. 3208, 3209, 3210

Schumann, U. and Konopka, P.: A simple estimate of the concentration field in a flight corridor, in: Impact of Emissions from Aircraft and Spacecraft upon the Atmosphere. Proc. of an Intern. Sci. Colloquium, Köln (Cologne), Germany, April 18-20, 1994, edited by: Schumann, U. and Wurzel, D., 354–359, DLR-Mitt. 94-06, 1994. 3187, 3191

Schumann, U. and Wendling, P.: Determination of contrails from satellite data and observational results, in: Air Traffic and the Environment – Background, Tendencies and Potential Global Atmospheric Effects, edited by Schumann, U., 138–153, Springer, 1990. 3187

Schumann, U., Konopka, P., Baumann, R., Busen, R., Gerz, T., Schlager, H., Schulte, P., and Volkert, H.: Estimate of diffusion parameters of aircraft exhaust plumes near the tropopause from nitric oxide and turbulence measurements, J. Geophys. Res., 100, 14147–14162, 1995. 3191, 3197, 3208, 3209, 3211, 3245

Schumann, U., Ström, J., Busen, R., Baumann, R., Gierens, K., Krautstrunk, M., Schröder, F. P., and Stingl, J.: In situ observations of particles in jet aircraft exhausts and contrails for different sulfur-containing fuels, J. Geophys. Res., 101, 6853–6870, doi:10.1029/95JD03405, 1996. 3200

Schumann, U., Schlager, H., Arnold, F., Baumann, R., Haschberger, P., and Klemm, O.: Dilution of aircraft exhaust plumes at cruise altitudes, Atmos. Env., 32, 3097–3103, 1998. 3198, 3216, 3228, 3236

Schumann, U., Arnold, F., Busen, R., Curtius, J., Kärcher, B., Petzold, A., Schlager, H., Schröder, F., and Wohlfrom, K. H.: Influence of fuel sulfur on the composition of aircraft exhaust plumes: The experiments SULFUR 1-7, J. Geophys. Res., 107, 4247, doi:10.1029/2001JD000813, 2002. 3200, 3201

Schumann, U., Mayer, B., Graf, K., Mannstein, H., and Meerkötter, R.: A parametric radiative forcing model for cirrus and contrail cirrus, in: ESA Atmospheric Science Conference, Barcelona, Spain, ESA SP-676, edited by: Agency, E. S., 1–6, Frascati, Italy, 2009. 3223

Contrail cirrus model

U. Schumann

Schumann, U., Mayer, B., Hamann, U., and Graf, K.: Radiative heating in contrail cirrus, Geophys. Res. Abstr., 12, EGU2010–1501–1, 2010. 3216

Schumann, U., Graf, K., and Mannstein, H.: Potential to reduce the climate impact of aviation by flight level changes, in: 3rd AIAA Atmospheric and Space Environments Conference, AIAA paper 1020774, 1–22, 2011a. 3189, 3224

Schumann, U., Mayer, B., Gierens, K., Unterstrasser, S., Jessberger, P., Petzold, A., Voigt, C., and Gayet, J.-F.: Effective radius of ice particles in cirrus and contrails, J. Atmos. Sci., 68, 300–321, doi:10.1175/2010JAS3562.1, 2011b. 3220, 3222, 3223

Schumann, U., Mayer, B., Graf, K., and Mannstein, H.: A parametric radiative forcing model for contrail cirrus, J. Appl. Meteor. Climatol., submitted, 2012. 3223

Schwartz Dallara, E., Kroo, I. M., and Waitz, I.: Metric for comparing lifetime averaged climate impact of aircraft, AIAA J., 49, 1600–1613, 2011. 3187

Scorer, R. S. and Davenport, L. J.: Contrails and aircraft downwash, J. Fluid Mech., 43, 451–464, 1970. 3187, 3188

Sharman, R., Tebaldi, C., Wiener, G., and Wolff, J.: An integrated approach to mid- and upper-level turbulence forecasting, Weather Forecast., 21, 268–287, 2005. 3208

Sölch, I. and Kärcher, B.: A large-eddy model for cirrus clouds with explicit aerosol and ice microphysics and Lagrangian ice particle tracking, Quart. J. Roy. Meteor. Soc., 136B, 2074–2093, doi:10.1002/qj.689, 2010. 3216, 3217, 3218

Sonntag, D.: Advancements in the field of hygrometry, Meteor. Z., 3, 51–66, 1994. 3194, 3239

Spichtinger, P., Gierens, K., and Dörnbrack, A.: Formation of ice supersaturation by mesoscale gravity waves, Atmos. Chem. Phys., 5, 1243–1255, doi:10.5194/acp-5-1243-2005, 2005a. 3215

Spichtinger, P., Gierens, K., and Wernli, H.: A case studies of the formation and evolution of ice supersaturation in the vicinity of a warm conveyor belt's outflow region., Atmos. Chem. Phys., 5, 973–987, 2005b. 3215

Spinhirne, J. D., Hart, W. D., and Duda, D. P.: Evolution of the morphology and microphysics of contrail cirrus from airborne remote sensing, Geophys. Res. Lett., 25, 1153–1156, 1998. 3220

Stohl, A., Hittenberger, M., and Wotawa, G.: Validation of the Lagrangian particle dispersion model FLEXPART against large-scale tracer experiment data, Atmos. Environ., 32, 4245–4264, 1998. 3203

Stohl, A., Haimberger, L., Scheele, M. P., and Wernli, H.: An intercomparison of results from

three trajectory models, Meteor. Appl., 8, 127–135, 2001. 3203

Sun, Z.: Reply to comments by Greg M. McFarquhar, Q. J. Roy. Meteor. Soc., 127, 267–271, 2001. 3226

Sun, Z. and Rikus, L.: Parametrization of effective sizes of cirrus-cloud particles and its verification against observations, Q. J. Roy. Meteor. Soc., 125, 3037–3055, 1999. 3226

Sussmann, R. and Gierens, K.: Lidar and numerical studies on the different evolution of vortex pair and secondary wake in young contrails, J. Geophys. Res., 104, 2131–2142, 1999. 3191, 3199, 3201

Sussmann, R. and Gierens, K.: Differences in early contrail evolution of two-engine versus four-engine aircraft: Lidar measurements and numerical simulations, J. Geophys. Res., 106, 4899–4911, 2001. 3194

Tompkins, A., Gierens, K., and Rädel, G.: Ice supersaturation in the ECMWF Integrated Forecast System, Q. J. Roy. Meteor. Soc., 133, 53–63, doi:10.1002/qj.14, 2007. 3192

Unterstrasser, S.: Numerische Simulationen von Kondensstreifen und deren Übergang in Zirren, Ph.D. thesis, University of Munich, Department of Physics, http://edoc.ub.uni-muenchen.de/9464, DLR-FB 2009-15, 2008. 3229

Unterstrasser, S. and Gierens, K.: Numerical simulations of contrail-to-cirrus transition – Part 1: An extensive parametric study, Atmos. Chem. Phys., 10, 2017–2036, doi:10.5194/acp-10-2017-2010, 2010a. 3188, 3191, 3192, 3199, 3202, 3209, 3216, 3217, 3229, 3233, 3235

Unterstrasser, S. and Gierens, K.: Numerical simulations of contrail-to-cirrus transition – Part 2: Impact of initial ice crystal number, radiation, stratification, secondary nucleation and layer depth, Atmos. Chem. Phys., 10, 2037–2051, doi:10.5194/acp-10-2037-2010, 2010b. 3188, 3202, 3216, 3229

Unterstrasser, S. and Sölch, I.: Study of contrail microphysics in the vortex phase with a Lagrangian particle tracking model, Atmos. Chem. Phys., 10, 10003–10015, doi:10.5194/acp-10-10003-2010, 2010. 3188, 3202

Unterstrasser, S., Gierens, K., and Spichtinger, P.: The evolution of contrail microphysics in the vortex phase, Meteor. Z., 17, 145–156, 2008. 3200, 3201, 3202

van de Hulst, H. C.: Light Scattering by Small Particles, Wiley, New York, 1957. 3222

Vazquez-Navarro, M. R.: Life cycle of contrails from a time series of geostationary satellite images, Ph.D. thesis, University of Munich, Department of Physics, http://edoc.ub.uni-muenchen.de/10913/, DLR-FB 2010-19, 2009. 3187, 3216

Voigt, C., Schumann, U., Jurkat, T., Schuble, D., Schlager, H., Petzold, A., Gayet, J.-F., Krämer,

Contrail cirrus model

U. Schumann

Title Page

Abstract | Introduction

Conclusions | References

Tables | Figures

◄◄ | ►►

◄ | ►

Back | Close

Full Screen / Esc

Printer-friendly Version

Interactive Discussion

M., Schneider, J., Borrmann, S., Schmale, J., Jessberger, P., Hamburger, T., Lichtenstern, M., Scheibe, M., Gourbeyre, C., Meyer, J., Kübbeler, M., Frey, W., Kalesse, H., Butler, T., Lawrence, M. G., Holzäpfel, F., Arnold, F., Wendisch, M., Döpelheuer, A., Gottschaldt, K., Baumann, R., Zöger, M., Sölch, I., Rautenhaus, M., and Dörnbrack, A.: In-situ observations of young contrails – overview and selected results from the CONCERT campaign, Atmos. Chem. Phys., 10, 9039–9056, doi:10.5194/acp-10-9039-2010, 2010. 3187, 3189, 3194, 3195, 3197, 3233, 3265

Voigt, C., Schumann, U., Jessberger, P., Jurkat, T., Petzold, A., Gayet, J.-F., Krämer, M., Thornberry, T., and Fahey, D. W.: Extinction and optical depth of contrails, Geophys. Res. Lett., 38, L11806, doi:10.1029/2011GL047189, 2011. 3196, 3197, 3222, 3272

Wernli, H. and Davies, H. C.: A Lagrangian-based analysis of extratropical cyclones. I: The method and some applications, Q. J. Roy. Meteor. Soc., 123, 467–489, 1997. 3203

Wilkerson, J. T., Jacobson, M. Z., Malwitz, A., Balasubramanian, S., Wayson, R., Fleming, G., Naiman, A. D., and Lele, S. K.: Analysis of emission data from global commercial aviation: 2004 and 2006, Atmos. Chem. Phys., 10, 6391–6408, doi:10.5194/acp-10-6391-2010, 2010. 3187, 3193

Wong, H.-W. and Miake-Lye, R. C.: Parametric studies of contrail ice particle formation in jet regime using microphysical parcel modeling, Atmos. Chem. Phys., 10, 3261–3272, doi:10.5194/acp-10-3261-2010, 2010. 3200

Contrail cirrus model

U. Schumann

Title Page

Abstract | Introduction

Conclusions | References

Tables | Figures

◄ | ►|

◄ | ►

Back | Close

Full Screen / Esc

Printer-friendly Version

Interactive Discussion

Table 1. Modules.

Name	Purpose, in sequence of calls	Sect.
INITMET	meteorological fields	2.2
READFP	reads flight plans	2.3
AINIT	aircraft properties	2.3
SAC	Schmidt-Appleman criterion	2.4
WINIT	wake vortex	2.5
ICEINI	ice mass and number initialization	2.6–2.7
INTCOCIP	integration for several time steps	2.8
RUNGE	Runge-Kutta	2.8
DTCONTR	time derivatives and contrail properties	2.8–2.12
RADI	radiative forcing analysis	2.14
TAU2DS	cloud mask for one contrail	2.15
TAU2DX	cloud mask for cirrus	2.15

Table 2. Critical model parameters.

Variable	Explanation	Eq.
$C_{D0} = 0.5$	initial wake vortex depth	(16)
$C_r = 0.9$	volume mean to effective particle radius ratio	(66)
$C_{z1} = 0.25$	wake vortex downwash distance	(15)
$E_A = 1$	aggregation efficiency	(54)
$E_{meso} = 2$	mesoscale sublimation efficiency	(57)
$E_T = 1$	turbulent sublimation efficiency	(51)
$EI_{soot} = 3.57 \times 10^{14}\,kg^{-1}$	soot number emission index	(19)
$f_{surv} = I_1/I_0$	survival factor	(24)
$f_T = 0.1$	sedimentation impact on D_V	(37)
$RHI_c = 0.8$	critical humidity for persistence	(9)
$w'_N = 0.1\,m\,s^{-1}$	turbulent velocity scale	(37)
$\Delta z_{eff} = 2000\,m$	effective resolution for shear	(41)
$\tau_c = 0.1$	optical depth threshold for cover	(71)

Table 3. Aircraft parameters used for test cases.

	Large	Medium	small	Unit
Type	B747	A330	B737	
span s_a	64.4	60	34.4	m
mass M_a	310	190	65	Mg
fuel flow f_F	12	6.5	3	$g\,m^{-1}$
V_a	250	240	230	$m\,s^{-1}$
EI_{soot}	2.8	2.8	2.8	$10^{14}\,kg^{-1}$
η	0.3	0.3	0.3	1

Table 4. Observed contrail properties for comparison with simulations. Refer.: Schr – Schröder et al. (2000) with corresponding aircraft types indicated, Feb – Febvre et al. (2009) for young (y) and aged (a) contrails, and one case of Voigt et al. (2010). For explanation of negative RHi_i see text. Stars[*] indicate estimated values.

Refer. Unit	AC type	age s	T °C	p hPa	RHi_m 1	RHi_0 1	RHi_i 1	IWC mg m^{-3}	n_m cm^{-3}	n_{ice} cm^{-3}	d_{mean} µm
Schr A	A310	5	−58	238	0.53	−0.35	1.02	0.26	1200	2506	0.60
Schr AT	ATTAS	8	−54	287	1.02	0.45	1.12	2.80	2200	3374	1.20
Schr B	B757	30	−54	262	0.85	0.83	1.04	0.91	1200	2599	0.90
Schr A1	A310	70	−54	262	0.85	1.03	1.14	3.20	1100	3033	1.30
Voigt CRJ2	CRJ2	90	−52	263	1.00	0.99	1.06	1.65	125	156	2.80
Schr B1	B737	120	−57	238	0.91	1.15	1.25	3.90	2150	4700	1.20
Schr D	A330*	135	−53	287	1.35	1.22	1.28	7.30	1150	5540	1.40
Feb y	E170	150	−60	196	1.20	0.99	1.08	0.90	68	69	3.00
Schr A2	A300*	200	−54	262	0.77	1.04	1.09	2.00	290	1016	1.60
Schr E	A330*	340	−55	262	1.20	1.06	1.09	1.90	870	1442	1.40
Schr B2	B737	600	−57	238	0.91	1.21	1.23	3.70	180	963	2.00
Schr F	Falco	700	−55	262	1.20	1.12	1.14	2.90	130	652	2.10
Schr O	A330*	800	−54	274	1.40	1.13	1.15	3.40	95	665	2.20
Feb a	E170	900	−60	196	1.20	1.07	1.09	1.00	19	20	4.70
Schr U	B737*	2000	−56	238	1.10*	1.21	1.22	3.90	11	23	7.00

Table 5. Input and results of contrail simulation. The last three columns list the CoCiP output. References as in Table 4.

Refer. Unit	age s	η 1	V_a m s^{-1}	M_a Mg	f_F g m^{-1}	s_a m	EI$_{soot}$ 10^{14} kg^{-1}	S 10^{-3} s^{-1}	IWC$_c$ mg m^{-3}	n_c cm^{-3}	d_c µm
Schr A	5	0.33	230	120	4.40	43.9	3	0	13.50	3532	2.00
Schr AT	8	0.17	177	18	1.00	21.5	10	1	2.55	3910	1.11
Schr B	30	0.33	240	95	4.31	38.0	3	0	14.46	3960	1.97
Schr A1	70	0.33	230	120	5.06	43.9	3	0	15.26	3453	2.10
Voigt CRJ2	90	0.26	210	52	1.30	21.2	3	2	0.67	230	1.82
Schr B1	120	0.33	230	60	2.82	34.3	3	0	17.57	3582	2.17
Schr D	135	0.33	230	190	6.50	60.3	3	0	15.09	2298	2.39
Feb y	150	0.33	220	30	1.85	26.0	3	2	0.79	210	1.99
Schr A2	200	0.33	230	140	6.22	44.8	3	1	2.46	331	2.49
Schr E	340	0.33	230	190	6.50	60.3	3	0	10.27	2143	2.15
Schr B2	600	0.33	230	60	2.82	34.3	3	1	4.07	121	4.13
Schr F	700	0.33	180	10	0.57	16.3	3	1	2.95	49	4.99
Schr O	800	0.33	230	190	6.50	60.3	3	1	3.83	122	4.03
Feb a	900	0.37	220	30	1.85	26.0	3	2	1.07	53	3.48
Schr U	2000	0.33	230	60	2.82	34.3	3	2	4.14	27	6.85

Table 6. List of symbols.

Parameter	Explanation	Unit
A	contrail cross-section area	m^2
B	contrail breadth	m
c	concentration	$kg\,m^{-3}$
c_p	specific heat capacity of air	$J\,(kg\,K)^{-1}$
C	fractional cloud cover	1
C_0	mass of a plume species per length	$kg\,m^{-1}$
d	particle diameter	m
D	contrail depth	m
D_{eff}	effective contrail depth A/B	m
D_H	horizontal diffusivity	$m^2\,s^{-1}$
D_V	vertical diffusivity	$m^2\,s^{-1}$
D_S	off-diagonal "shear" diffusivity	$m^2\,s^{-1}$
e	kinetic energy of turbulent subgrid-scale motions	$m^2\,s^{-2}$
E_{SGS}	kinetic energy of all subgrid-scale motions	$m^2\,s^{-2}$
EI	emission index, mass or number per fuel mass	$kg\,kg^{-1}$, kg^{-1}
f_{surv}	fraction of particles surviving the wake vortex phase	1
g	gravity	$m\,s^{-2}$
G	mixing line gradient	$Pa\,K^{-1}$
I	ice mass mixing ratio	$kg\,kg^{-1}$
IWC	ice water concentration	$kg\,m^{-3}$
IWP	ice water path	$kg\,m^{-2}$
ℓ	NWP subgrid length scale	m
L	horizontal segment length	m
L_s	latent heat of sublimation	$J\,kg^{-1}$
m_F	fuel consumption per flight distance	$kg\,m^{-1}$
M	plume mass per contrail length	$kg\,m^{-1}$
M_s	molar mass of species s (air, H_2O)	$kg\,mol^{-1}$
M_a	aircraft mass	kg
n	number of ice particles per volume	m^{-3}
N	total ice number concentration per contrail length	m^{-1}
N_{BV}	Brunt-Vaisaila frequency	s^{-1}
N_W	number of waypoints	1
N_{dil}	ratio between contrail mass and fuel flow per length	1
OLR	outgoing longwave radiation	$W\,m^{-2}$
p	pressure	Pa
p_{liq}	liquid saturation pressure	Pa
p_{ice}	ice saturation pressure	Pa
q	absolute humidity (mass fraction of water vapor in air)	$kg\,kg^{-1}$
q_s	ice saturation humidity	$kg\,kg^{-1}$
Q_{ext}	solar radiation extinction efficiency	1

Contrail cirrus model

U. Schumann

Title Page

Abstract	Introduction
Conclusions	References
Tables	Figures

|◄ | ►|

◄ | ►

Back | Close

Full Screen / Esc

Printer-friendly Version

Interactive Discussion

Table 6. Continued.

Parameter	Explanation	Unit
Q_{fuel}	heat of fuel combustion	MJ kg^{-1}
r	volume mean particle radius	m
r_{eff}	optically effective particle radius	m
R_0, R_1	gas constants of air and water vapor	J (kg K)$^{-1}$
Ri	Richardson number N_{BV}^2/S_T^2	1
RF	radiative forcing	W m^{-2}
RSR	reflected shortwave radiation	W m^{-2}
s_a	aircraft wing span	m
SDR	solar direct radiation	W m^{-2}
S_0	solar constant	W m^{-2}
S_i	flight segment $(W_i, W_i + 1)$	
S, S_T	shear perpendicular to plume, total shear	s^{-1}
t	time or age	s
T	absolute temperature	K
T_{LC}	threshold temperature	K
T_{LM}	maximum threshold temperature	K
u	air speed in x-direction	m s^{-1}
U	relative humidity of liquid saturation	1
v	air speed in y-direction	m s^{-1}
V_a	aircraft true airspeed	m s^{-1}
V_T	particle terminal fall velocity	m s^{-1}
w	vertical velocity	m s^{-1}
w'_N	stratified turbulence velocity scale	m s^{-1}
W_i	waypoint (x_i, y_i, z_i, t_i), $i = 1, 2, \ldots, N_W$	°, °, m, s
x	longitude	°
X	vector of variables (x, y, p, σ, I, N)	
y	latitude	°
z	altitude above sea level	m
ϵ	kinetic energy dissipation rate	m^2 s^{-3}
Δt	time step	s
Δz_w	downwash distance	m
η	overall propulsion efficiency	1
Γ	wake vortex circulation	m^2 s^{-1}
μ	cosine of solar zenith angle	1
ρ, ρ_{ice}	air, bulk ice density	kg m^{-3}
ω	pressure change rate	Pa s^{-1}
σ	covariance matrix	m^2
$\sigma_{yy}, \sigma_{zz}, \sigma_{yz}$	elements of σ	m^2
τ	solar optical depth	1
τ_{dil}	time scale of dilution	s
θ	solar zenith angle	°
Θ	potential temperature	K

Table 7. Abbreviations.

Acronym	Explanation
ACCRI	FAA-project "Aviation Climate Change Research Initiative"
BADA	Base of Aircraft Date from EUROCONTROL
CATS	DLR-project "Climate-compatible Air Transport System"
CI	cirrus
CO	contrail
COCI	contrail cirrus
CoCiP	Contrail Cirrus Prediction tool
CONCERT	CONtrail and Cirrus ExpeRimenT
COSMO-DE	Consortium for Small Scale Modelling – Deutschland, NWP model of DWD
DFS	Deutsche Flugsicherung
DLR	Deutsches Zentrum für Luft- und Raumfahrt
DWD	Deutscher Wetterdienst
ECMWF	European Centre for Medium Range Weather Forecasts
EU	European Union
EURO- CONTROL	European Organization for the Safety of Air Navigation
FAA	Federal Aviation Administration
ICAO	International Civil Aviation Organization
IFS	Integrated Forecasting System
ISSR	ice supersaturated region
LES	large-eddy simulation
LW	longwave
NWP	numerical weather prediction
OLR	outgoing longwave radiation
RSR	reflected shortwave radiation
REACT-4C	EU project "Reducing Emissions from Aviation by Changing Trajectories for the benefit of Climate"
SAC	Schmidt-Appleman criterion
SGS	subgrid scale
TOA	top of atmosphere
US, USA	United States, ... of America
2d, 3d	two-dimensional, three-dimensional

Contrail cirrus model

U. Schumann

Title Page

Abstract | Introduction

Conclusions | References

Tables | Figures

◄ | ►|

◄ | ►

Back | Close

Full Screen / Esc

Printer-friendly Version

Interactive Discussion
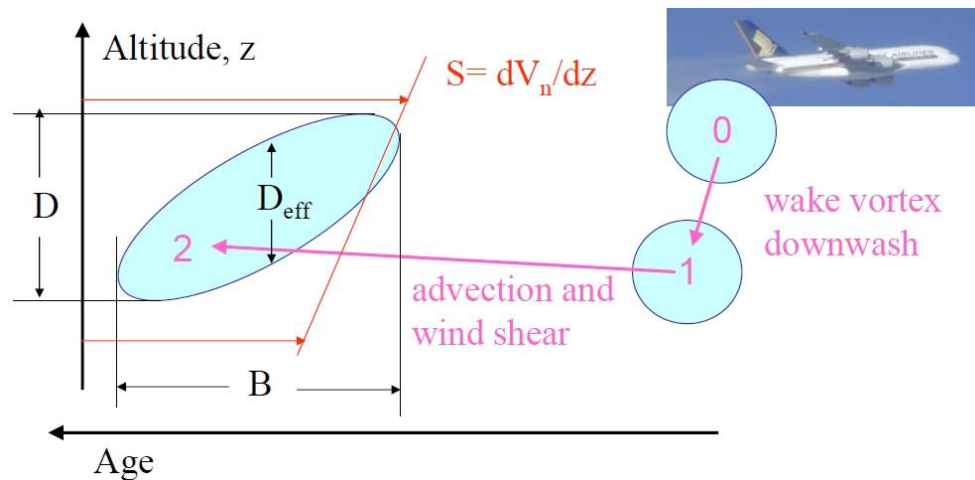
Fig. 1. Schematic of contrail dynamics versus altitude and contrail age with plume depth D, breadth B, and normal velocity shear dV_n/dz at stages 0: contrail formation, 1: downwashed wake vortex, 2: aged Gaussian cross-section.

Title Page

Abstract | Introduction

Conclusions | References

Tables | Figures

⏮ | ⏭

◀ | ▶

Back | Close

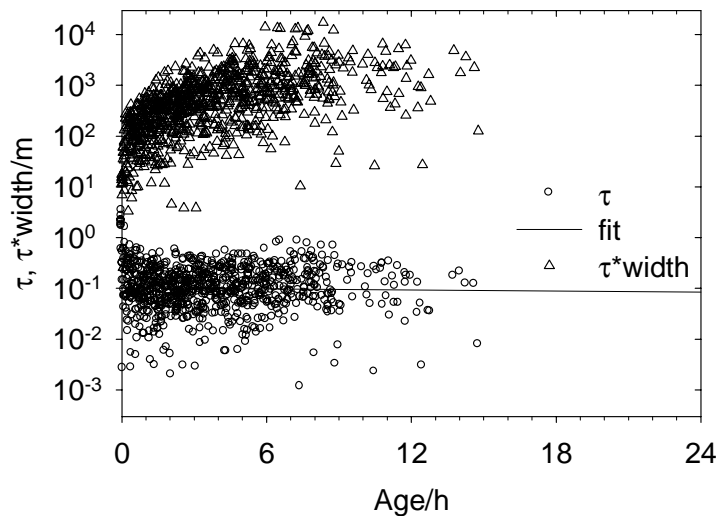Full Screen / Esc

Printer-friendly Version

Interactive Discussion

Initialization:
Read data base with aircraft properties
Read and store NWP input for all x, y, z, t (INITMET)

Loop over tracks and integration in time:
FOR n=1 UNTIL end of flight list DO
    Call READFP to read waypoints of flight path
    Check of flight path times, maximum age, and positions
    Complete aircraft properties (AINIT)
    Interpolate in meteorology for stage "0"
    IF (Schmidt-Appleman satisfied (SAC)?) THEN
        Init wake properties (WINIT)
        Compute properties at stage "1"
        Init ice mass and number (ICEINI)
        Call INTCOCIP for time integration
            FOR t = time of flight TO time of analysis
                    or UNTIL end of contrail life time DO
            CALL Runge Kutte (RUNGE) in steps of Δt
                CALL DTCONTR to compute time derivatives
            END time LOOP
        END of integration
        analyze τ, radiative forcing (RF), cover (TAU2DS) etc.
        output of individual contrail properties
    END IF
END flight LOOP

Post-processing:
analyze cover of contrail/cirrus ensemble (TAU2DX)
Write output for statistics and plots

Fig. 2. CoCiP simulation framework. For a list of CoCiP modules see Table 1.
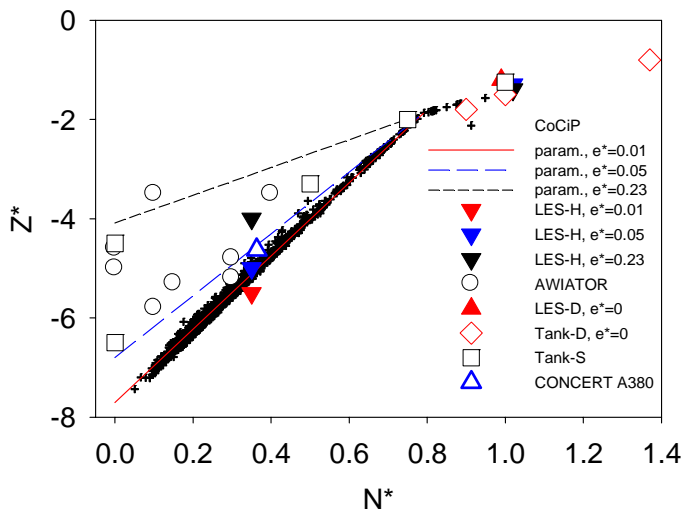
Fig. 3. Non-dimensional maximum wake vortex sinking distance versus nondimensional stratification. $Z* = -\Delta z/b_0$, $b_0 = (\pi/4)s_a$, $N* = N_{BV}t_0$, $t_0 = 2\pi b_0^2/\Gamma_0$, $\Gamma_0 = M_a g 4/(\pi s_a \rho V_a)$. Crosses depict CoCiP results. The deviation from a piece-wise straight line is a consequence of different (non-dimensional) turbulent dissipation rates $e* = (\epsilon b_0)^{1/3}/w_0$, $w_0 = b_0/t_0$. The lines depict the parameterization for fixed $e* = 0.01$, 0.05 and 0.23 (red, blue, black) (Holzäpfel, 2003). Filled symbols with corresponding colors are LES results (Hennemann, 2010; Delisi and Robins, 2000). Open symbols are experimental results in tanks (Sarpkaya, 1983; Delisi and Robins, 2000) and behind aircraft (deBruin and Kannemans, 2004; Voigt et al., 2011) (projects AWIATOR and CONCERT).

Contrail cirrus model

U. Schumann
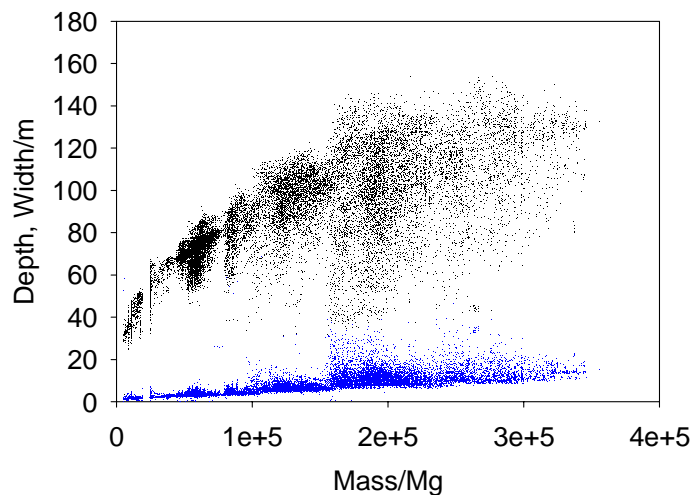
Fig. 4. Initial contrail depth (black) and width (blue) versus aircraft mass for an example traffic and meteorology over the North Atlantic in June 2006.
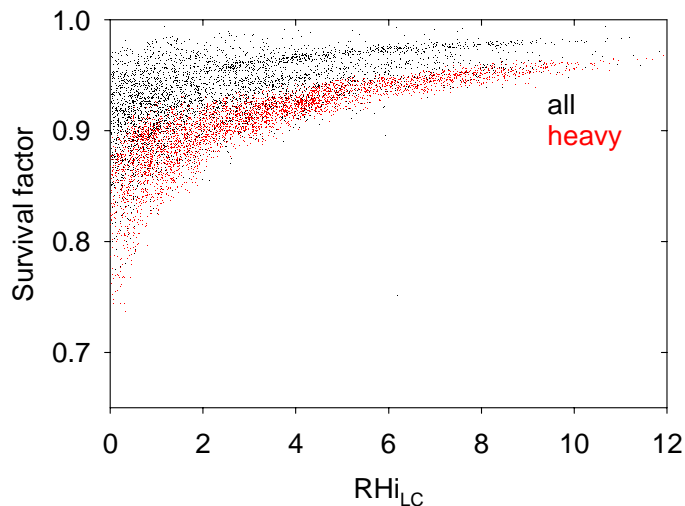
Fig. 5. Survival factor for ice mass due to adiabatic wake vortex sinking versus the critical relative humidity over ice RHi_{LC} for contrail formation for meteorology over the North Atlantic in June 2006 and for air traffic with all aircraft as occurring (black) or replaced by heavy aircraft (red).
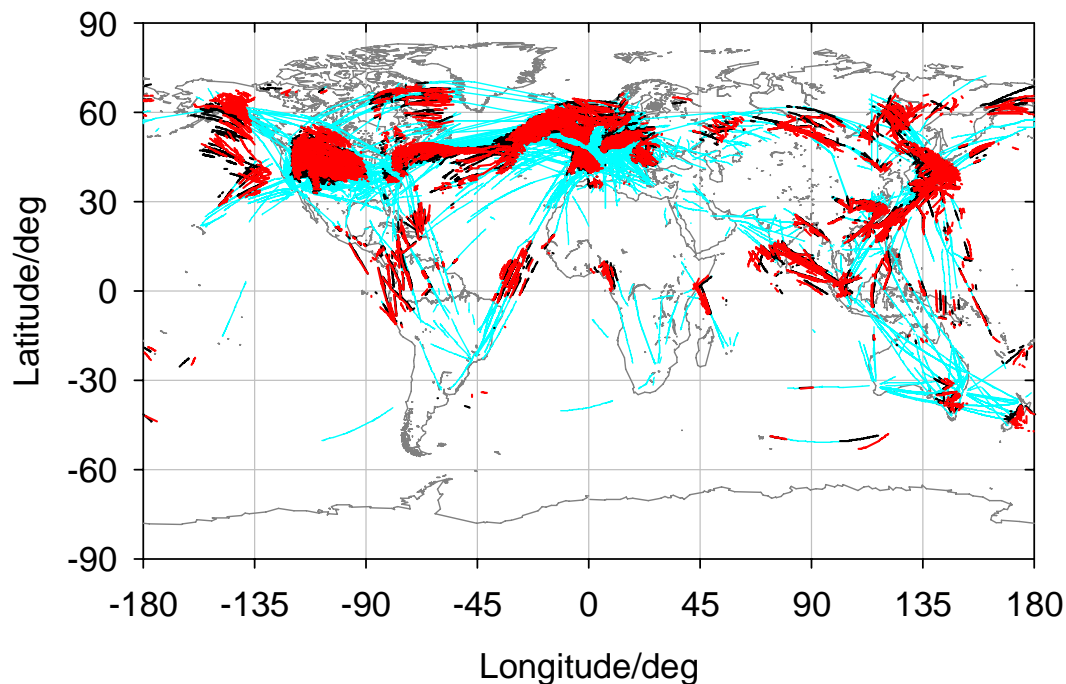
Fig. 6. Contrail forming flight paths (cyan) for global traffic between 03:00–06:00 UTC for a day in June 2006. Contrails existing at 06:00 UTC that day are identified by red lines. Those parts of the tracks from where these contrails originated are shown in black.
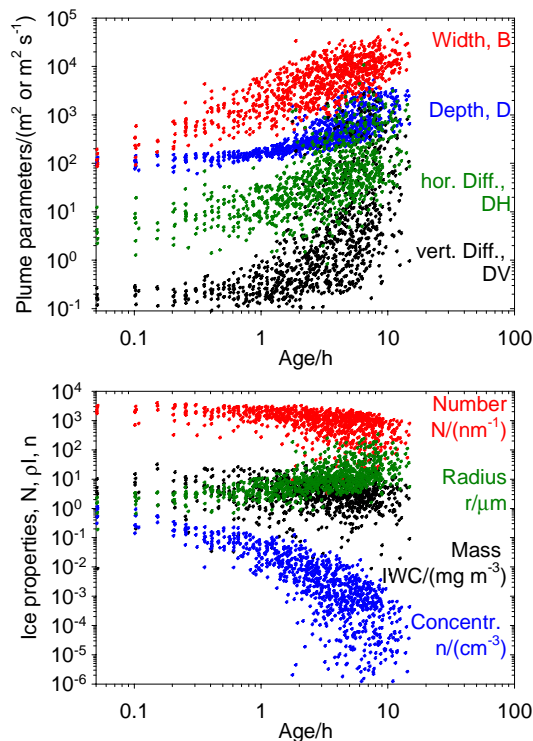
Fig. 7. Contrail properties versus contrail age. Top panel: Width B and depth D in m, horizontal and vertical diffusivity D_H and D_V in $m^2 s^{-1}$. Bottom panel: Total number of ice particles per nanometer flight distance, N, ice particle radius r, ice water mass content per volume ρI, and ice particle number per volume n for contrails in the North Atlantic region during 3 days in June 2006.
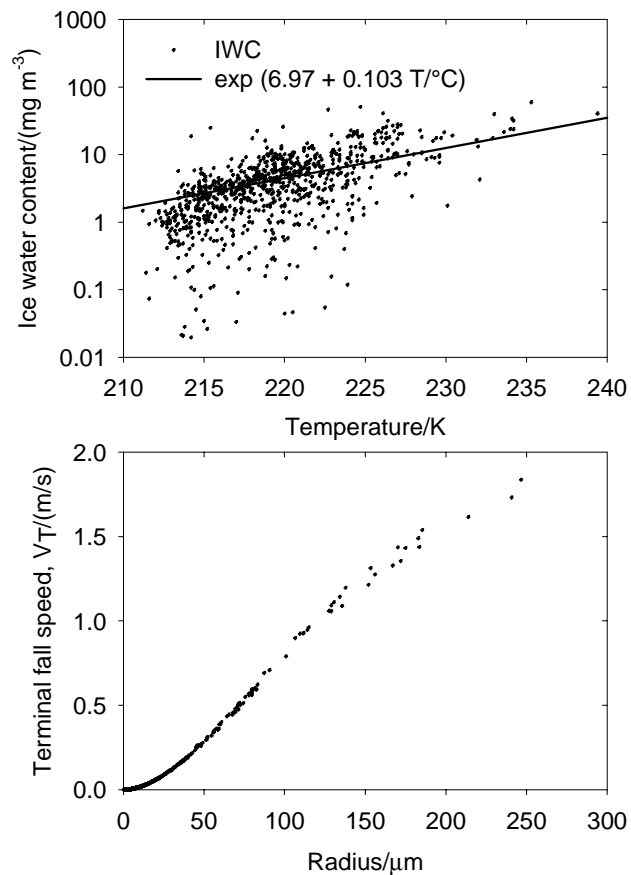
Fig. 8. Top:Ice water content versus temperature compared to an empirical approximation (Schumann, 2002; Schiller et al., 2008). Bottom: Terminal fall velocities versus particle radius.
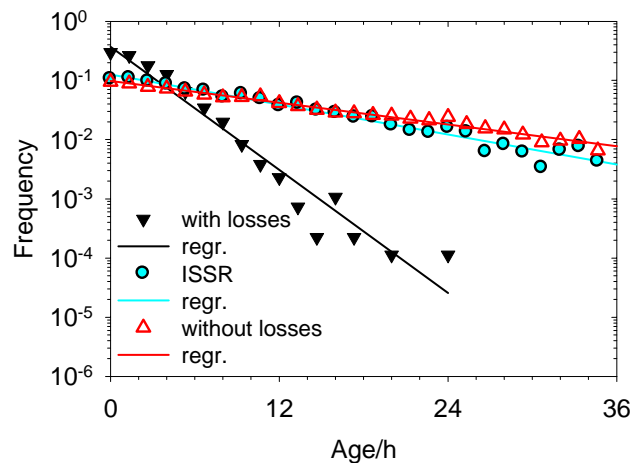
Fig. 9. Age frequency of ice supersaturated regions (cyan: ISSR) and of contrails (black: with losses, red: without losses).

Fig. 10. Solar optical depth and its product with contrail width versus contrail age.

Optical depth of contrails

Optical depth of cirrus including contrails
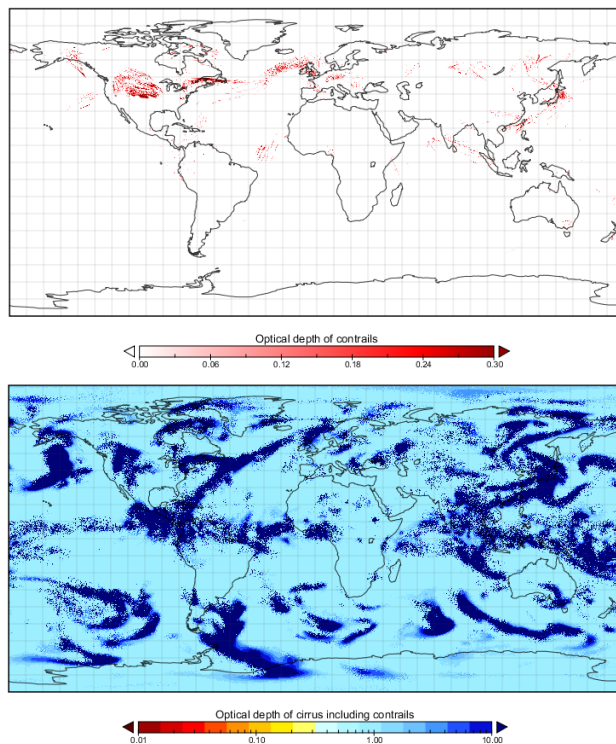
Fig. 11. Optical depth of contrail cover (top) and of cirrus and contrails (bottom) for traffic and time as in Fig. 6.
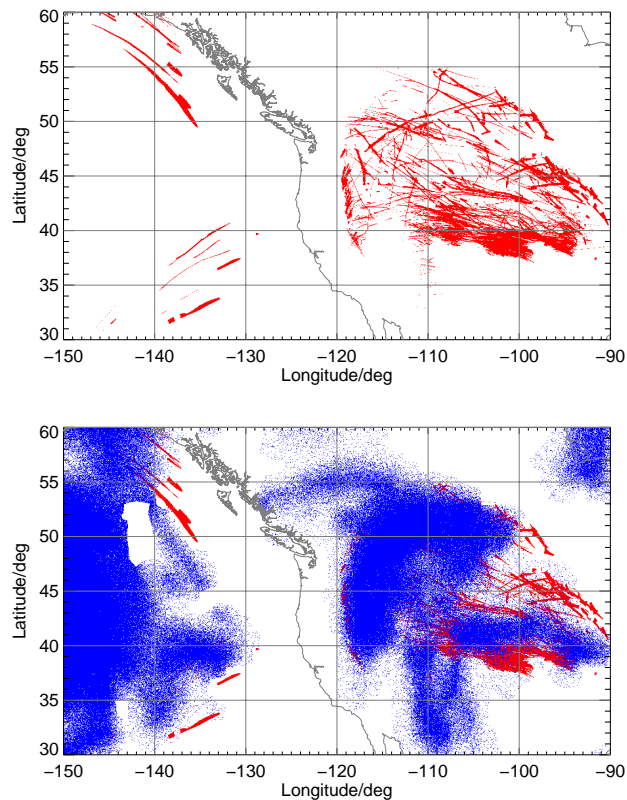
Fig. 12. Distribution of total cirrus-cover composed of natural cirrus and contrail-cirrus for a North American region with a contrail outbreak. Top: contrail-cirrus pixels (red); bottom: natural cirrus pixels (blue) and contrail-cirrus pixels (red).

Discussion Paper | Discussion Paper | Discussion Paper | Discussion Paper |

GMDD

4, 3185–3293, 2011

Contrail cirrus model

U. Schumann

Title Page

Abstract | Introduction

Conclusions | References

Tables | Figures

|◄ | ►|

◄ | ►

Back | Close

Full Screen / Esc

Printer-friendly Version

Interactive Discussion
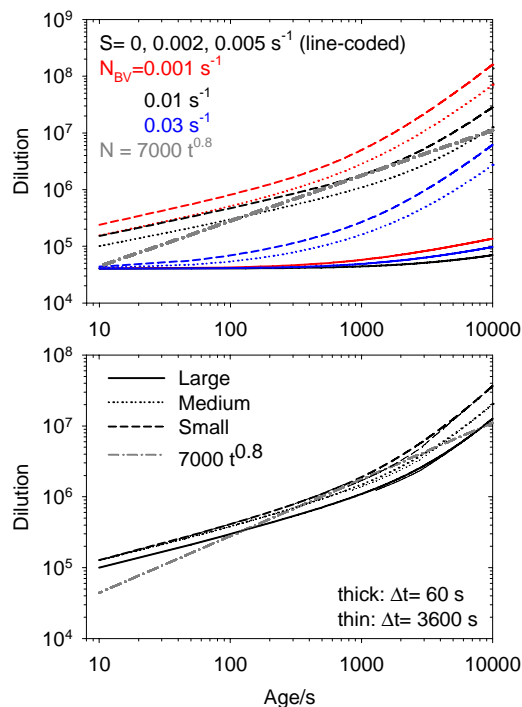
Fig. 13. Bottom: Dilution versus plume age for various aircraft sizes with results for two time step variants in comparison to an empirical dilution function Eq. (18) for fixed shear $S = 0.002\,\text{s}^{-1}$ and Brunt-Vaisaila frequency $N_{BV} = 0.01\,\text{s}^{-1}$. Top: Dilution versus plume age for a large aircraft for different shear S (full curve: 0, dotted: $0.002\,\text{s}^{-1}$, dashed: $0.005\,\text{s}^{-1}$) and different Brunt-Vaisaila frequency N_{BV} (red: $0.001\,\text{s}^{-1}$, black: $0.01\,\text{s}^{-1}$, blue: $0.03\,\text{s}^{-1}$), in comparison to the empirical dilution function.
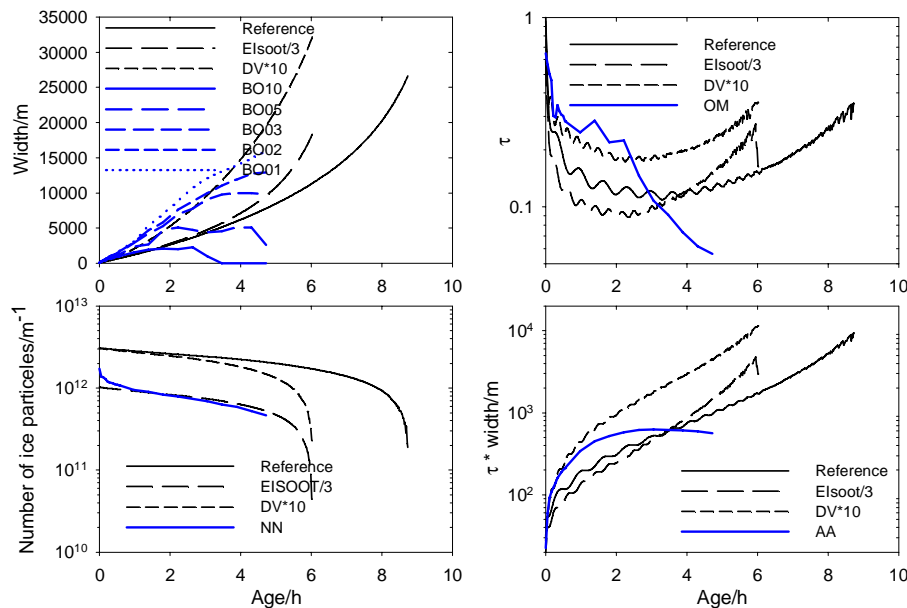
Fig. 14. Comparison of CoCiP results for various contrail properties (black lines) versus plume age with results of a 2d model (blue lines), for CoCiP reference case and for reduced soot emissions and increased vertical diffusivity.

Full Screen / Esc
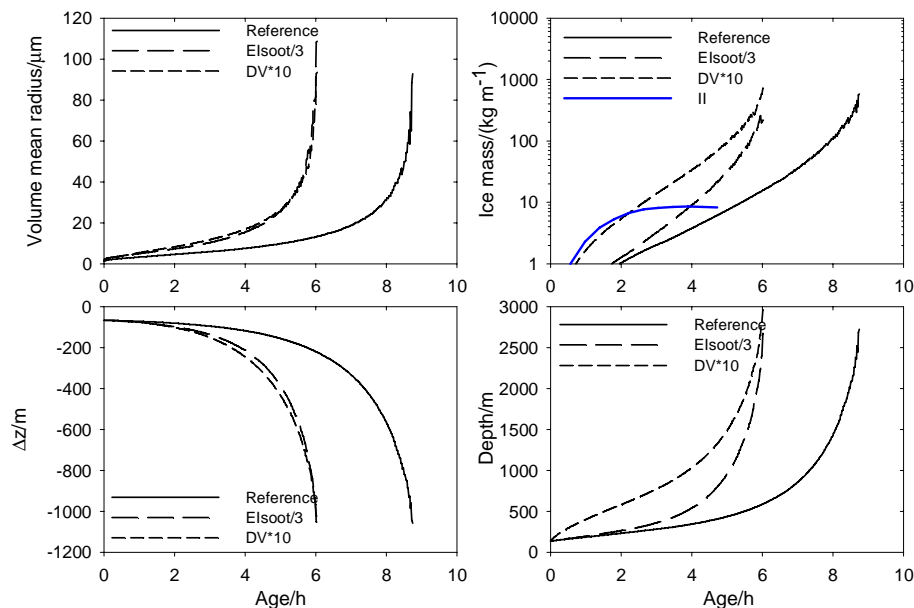
Fig. 15. Same as Fig. 14 for further contrail properties.
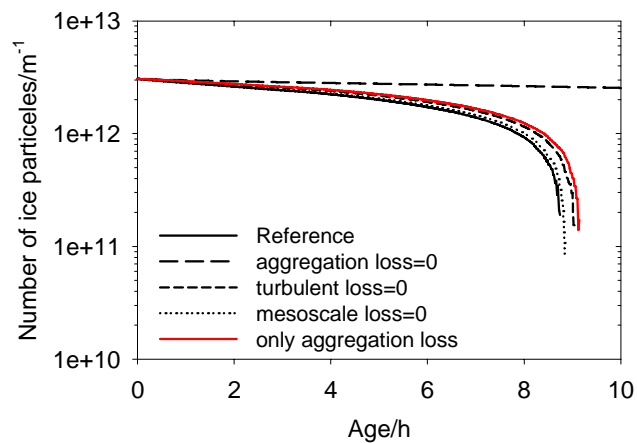
Fig. 16. Ice number per distance: Impact of particle loss processes.
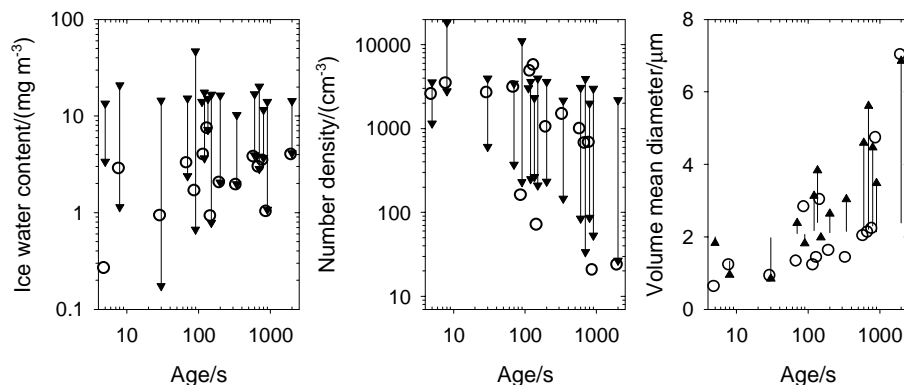
Fig. 17. Comparison of CoCiP results (lines with triangles, pointing towards increasing shear, for shear from 0 to 0.002 m s^{-1}) with observations (open circles) versus contrail age: **(a)** Ice water content, **(b)** ice particle number concentration, **(c)** volume mean ice particle diameter.
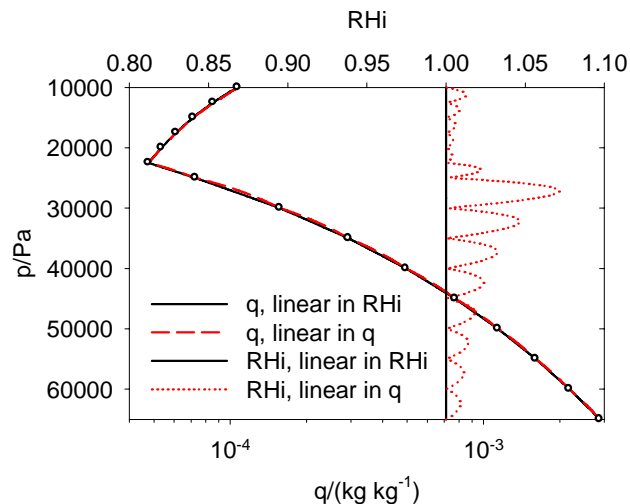
Fig. 18. Impact of linear interpolation between discrete grid point values (circles) in either absolute (q) or relative (RHi) humidity versus pressure-altitude for the ICAO standard atmosphere with RHi = 100 %. Data are provided in this example (and in the ECMWF data used) with 50 hPa intervals below 250 hPa and 25 hPa above that altitude.
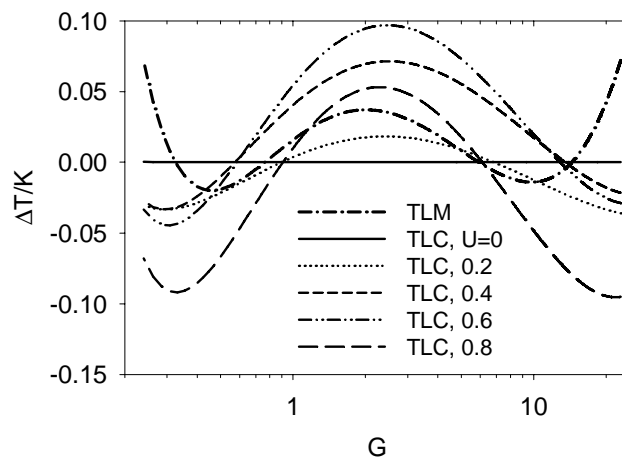
Fig. 19. Difference between fit (Eqs. 10 and A16) and exact solution for contrail threshold temperature at liquid saturation $T_{LM} = T_{LC}(U = 1)$, and T_{LC} for given relative humidity U over liquid water.
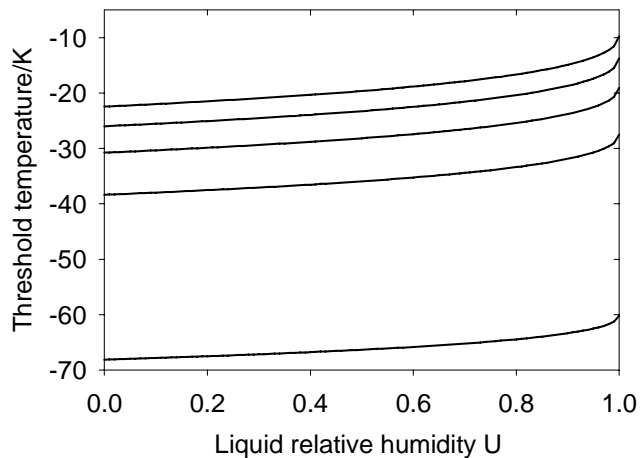
Fig. 20. Threshold temperature T_{LC} versus liquid relative humidity for 5 values of G, equidistant between 0.24 and 23 Pa K^{-1}, from bottom to top.
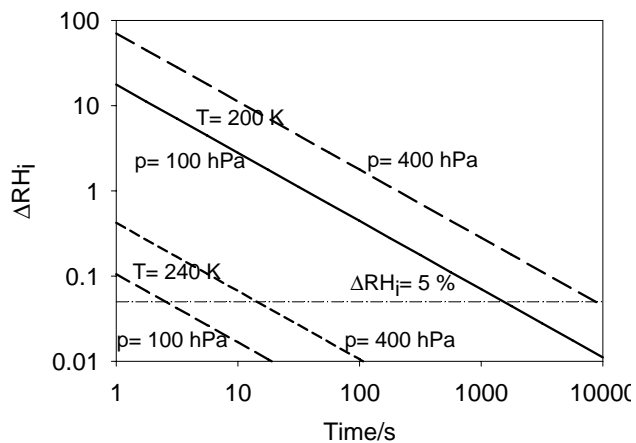
Fig. 21. Relative humidity increase over ice due to engine water vapor emissions versus time.

Contrail cirrus model
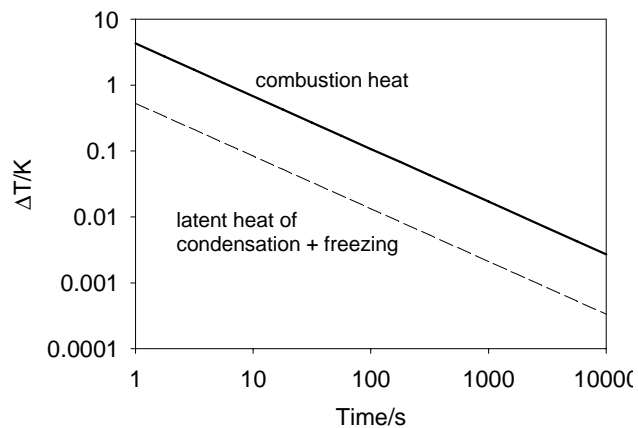
U. Schumann

Fig. 22. Temperature increases due to combustion heat and latent heat releases versus time.
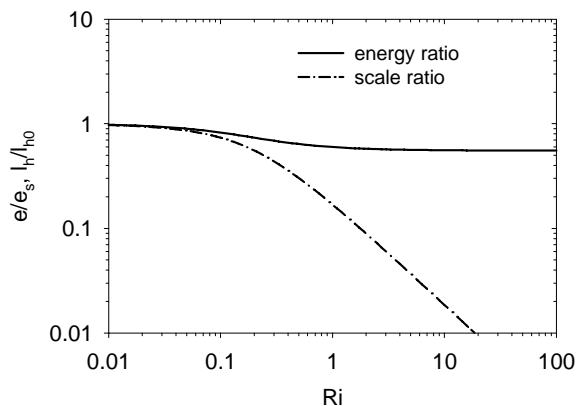
Fig. 23. Subgrid-scale energy and scale ratio versus Richardson number, $e_s = e(Ri = 0)$, $\ell_{h0} = \ell_h(Ri = 0)$.
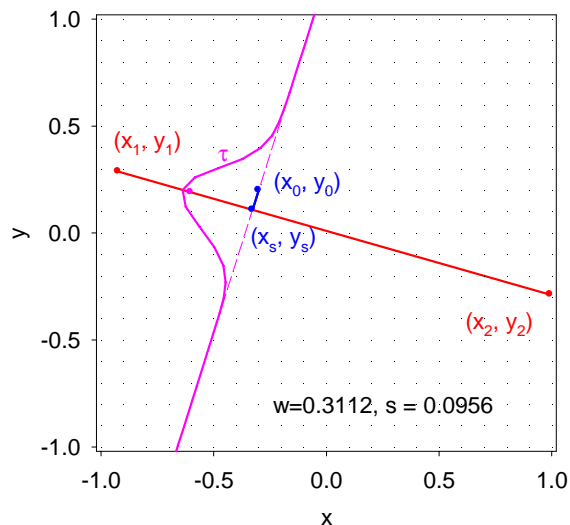
Fig. 24. Example of a contrail-segement $(x_1, y_1), (x_2, y_2)$ (red) with closest connection (blue) from a point (x_0, y_0) in the cloud mask to (x_s, y_s) on the contrail center-line, and contribution to optical depth τ, see Sects. 2.15 and A12.